Naturally-inspired circuits for microbial composition control and biosensing

Thesis by
Matthieu Francois Kratz

In Partial Fulfillment of the Requirements for the
Degree of
Bioengineering

CALIFORNIA INSTITUTE OF TECHNOLOGY
Pasadena, California

2026
Defended October 14, 2025

ACKNOWLEDGEMENTS

I want to thank my advisors, Richard Murray and Michael Elowitz. Richard, thank you for giving me the intellectual freedom to pursue whatever I wanted, and for sticking with me through the many ups and downs. Michael, thank you for taking me into your group when I switched advisors, and for providing the right balance of mentorship and space to succeed on my own terms.

I am also grateful to my thesis committee — Gozde Demirer, Justin Bois, and Bruce Hay — for being both understanding and intellectually engaged. Your thoughtful feedback and challenges helped strengthen the direction and rigor of my work.

To my family: thank you for your unwavering love and support throughout this journey. I am especially grateful to my father, whose encouragement and belief in me across so many stages of life gave me the confidence to pursue a PhD in the first place.

To my first set of Caltech PhD friends — Costa, Henry, Ryan, Mikey, Jordan, and Keefe — thank you for filling the Treatment Sanctuary with warmth, absurdity, and laughter. From family dinners to late-night gaming in the sunroom, those years were some of the best of my PhD. I especially want to thank Costa and Henry, my gamer companions through so many magical, often ridiculous moments — you two made life feel lighter and more vibrant.

To my later crew — Blade, Nikos, and Mark — thank you for being true kindred spirits and like(feeble)-minded friends. I've lost count of how many times we've cried laughing at jokes that make no sense in hindsight. Beyond that, you helped shoulder my stress and uncertainties about the future, and made these final, chaotic years full of joy and meaning.

To everyone in the Murray Lab, past and present — thank you for fostering an intellectually rigorous and collaborative environment. I'm especially grateful to John Marken. In the latter years of my PhD, you were effectively a third advisor and a deeply valued friend. You helped me stay grounded, taught me how to ask sharper questions at every scale, and helped me navigate the challenges of doing a PhD in the Elowitz Lab. Your influence on my scientific development is impossible to overstate, and I'll always be grateful.

Finally, I would like to thank the Jun Lab at UCSD — much of the work presented

in Chapters 2 and 3 of this thesis would have a year longer to achieve without their help. I especially want to thank Suckjoon, Michael, and Haochen!

ABSTRACT

When considering the design of gene circuits, there are many possible sources of inspiration. Many early synthetic gene circuits used nature as an inspiration, seeking to recreate biological behaviors with non-native components. As the field grew, alternative approaches sourcing designs from adjacent engineering fields and computational approaches emerged and grew in prominence. Despite this shift, there remains a great deal of naturally-inspired circuits that provide useful functions for biotechnology. Indeed nature has often been uniquely capable of exploiting typically undesirable phenomena, e.g. noise to create biologically useful function.

This thesis presents two projects directly inspired by natural systems. Each project aims to replicate a behavior or circuit topology found in nature, leveraging its unique dynamics to address key challenges in biotechnology. Chapters 2 and 3 will cover the development of a circuit emulating the microbial behavior of phase variation, whereby individual cells reversibly and stochastically transition between distinct phenotypes. We recreate this behavior using serine recombinases and demonstrate how it can enable stable, bulk control of phenotype composition—a task of great relevance to biotechnology. Chapter 4 lays the groundwork for applying the biologically-relevant feed-forward loop topology to the problem of spurious biosensor activation. We realize this topology in a modular manner using small transcription activating RNAs (STARs) and provide a preliminary characterization of its dynamical properties. Finally, we discuss alternative implementations that may provide more directly applicable properties than the current STAR implementation.

PUBLISHED CONTENT AND CONTRIBUTIONS

1. Kratz, M. F., Murray, R. M. & Elowitz, M. B. *Synthetic Phase Variation for Engineered Microbial Consortia* en. ISSN: 2692-8205 Pages: 2025.08.25.672192 Section: New Results. Aug. 2025. https://www.biorxiv.org/content/10.1101/2025.08.25.672192v2 (2025).
   M.F.K conceived and designed the project, performed the experiments, analyzed the data, and wrote the manuscript with R.M.M and M.B.E. The manuscript is currently under review in Nature Communications.

TABLE OF CONTENTS

Chapter 1

INTRODUCTION

1.1 The naturally-inspired approach to designing genetic circuits

The earliest approach to designing synthetic gene circuits involved recreating natural circuit dynamics using genetic components from different biological contexts. This approach is clearly demonstrated in the earliest circuits of our field; the Represillator [1] and the Toggle Switch [2]. The Represillator used three genes arranged in a cyclic inhibitory feedback loop, where each gene represses the next gene in the cycle, creating self-sustaining oscillations in the expression of each gene. The Toggle Switch similarly consisted of two mutually inhibitory genes, creating two stable steady states characterized by dominance of one inhibitory gene over the other.

In both cases, the authors explicitly selected components that were not natively involved in bistability or oscillations to recreate these natural dynamics. When looking at these two pivotal works, their inspiration is clearly stated. Elowitz et al. repeatedly mention the inspiration from and draw comparison to the natural biological time-keeping function associated with circadian clocks. Gardner et al. similarly mention these circadian clocks as well the bacteriophage Lambda lysis-lysogeny bistable switch. These early works underscore the prevailing goal of the field: recreate complex natural dynamics using simple genetic parts and networks.

Although not strictly synthetic circuits, early work from Mangnan et al. [3] was particularly influential for this naturally-inspired approach. In their work, they examined the dynamical properties of the recurring feed-forward loop (FFL) network motif, a motif characterized by a transcription factor regulating both a target gene directly and indirectly. They demonstrated computationally that these were capable of a wide variety of dynamical behaviors from sign-sensitive response acceleration to signal filtering and pulse generation. This work provided many candidate network designs for broadly useful dynamical behaviors and highlighted the rich and complex dynamics that can arise from relatively simple, naturally-occurring circuit motifs.

1.2 Applying an engineering mindset to gene circuit design

Although the naturally-inspired approach was prevalent in the first works of our field, several alternative approaches arose as the field grew. Notably, an approach underscored by the application of classical engineering principles such as modularity and abstraction arose. In principle, this approach was necessary to orchestrate the larger circuits that would enable more complex dynamics and was an approach that characterized many prominent works of the post-Represillator era. Many key works placed emphasis on creating distinctly non-biological behaviors, taking inspiration from and putting into practice principles from engineering and adjacent fields such as computing.

Part of this effort came in the massive expansion of characterized genetic parts, with the Anderson promoter library being one of the most influential examples. In this library, the -35 and -10 regions of the consensus σ_{70} promoter were varied to generate a combinatorial library that was subsequently screened in *E. coli*. This work underscored the desire of the community to generate a much larger variety of characterized genetic parts to eventually assemble into more complex circuits.

Another salient example of this engineering inspired approach can be found in the work by Nielsen et al [4]. In their work, the authors developed Cello, effectively an AutoCAD for the design of logic gate circuits. Specifically, Cello converted high level descriptions of circuit performance into DNA sequences that can be deployed in living cells. To do so, Cello drew from a characterized and engineered pool of repressors implementing NOT/NOR logic, assembling these units to create the desired behavior. Much like AutoCAD, it employed modular components, supported simulation and validation, and abstracted most low-level details of the constituent parts. The electrical-engineering inspiration permeates throughout this entire work, from the resulting NIMPLY and XNOR logic-gates to direct references to electrical design automation.

Another work that exemplifies this approach came from Tabor et al. [5] who implemented a light-edge detection algorithm by combining both a dark sensor and quorum sensing system (Figure 1.1). The light-edge detection arises from how an activating, diffusible quorum-sensing molecules (AHLs) and a repressing gene interact with a pigment producing gene LacZ. Light-exposed cells produce both AHLs and a repressor, with said repressor overpowering the activating signal from the AHL within a given cell, preventing expression of LacZ. Dark-exposed cells express neither the AHL nor the repressor and thus similarly do not express LacZ.

However, when these two cell populations are in proximity, e.g. at light edges, the diffusible AHL from the light cells activate the unrepressed dark cells, leading to pigment production exclusively at light-dark interfaces. The computational and engineering inspiration for this work is clear — edge detection is a well-known task in computer science and the authors used small constituent circuits to compose a larger program.

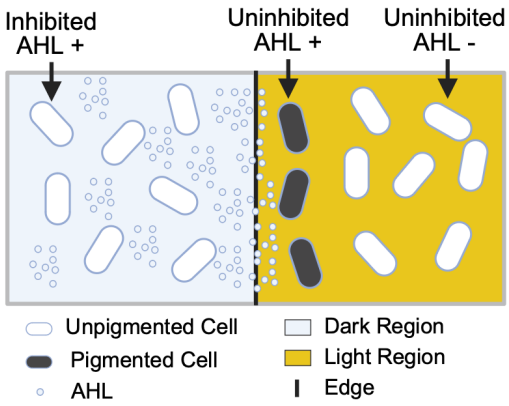

Figure 1.1: Edge detector circuit schematic. All cells in the system contain the same gene construct. Edge detection arises from the unique activation of pigmentation in zones where both light exposed and dark exposed cells are in close proximity [5].

1.3 Computational and data-driven circuit design

In parallel to the engineering-inspired approach, an approach relying on computational design of circuits arose. Initially, this involved exhaustive enumeration and simulation of small networks. Ma et al. [6] used such an approach explore all 3-node topologies capable of performing adaption — the ability to reset themselves after responding to a stimulus. Although their work was exclusively in silico, they highlighted a finite set of circuits capable of adaption across a wide parameter range. In contrast to early versions of these approaches, modern versions have harnessed advances in search algorithms to more efficiently explore this design space. For instance, Bhamidipati et al. [7] developed an approach employing Monte Carlo Tree Search to optimize circuit topology for a given target circuit behavior. With this approach, they deeply and efficiently explored the design of 3-node networks with mutationally-robust oscillations and even scaled their search to a 5-node system.

Perhaps the most important evolution of this approach came in the form of integration of experimental data, made possible by our increased capacity to generate and parse large amounts of the design space. For instance, Rai et al. [8] developed

an approach combining barcoding with long and short read sequencing to analyze combinatorial construct libraries assembled via pooled methods. The generated libraries can be screened in vivo and samples performing the desired function can be mapped back to specific constructs via sequencing. They used this approach to generate multi-layered logic circuits, where protein domains, promoters, and other elements were varied to generate a library with over 10^5 unique constructs. The resulting phenotype-to-construct dataset was used to train a multi-layer perceptron neural network that could accurately predict the behavior of unsampled constructs. Although a relatively simple circuit, their work demonstrates the potential of these high throughput computational approaches as sources for circuit designs.

1.4 Shifting prevalence of these approaches

In the early days of gene circuit design, the naturally-inspired approach was ubiquitous. However, as the field grew, the engineering-inspired and computational approaches became much more prominent. In particular, the engineering-inspired approach to circuit design was central to much of the post-repressilator gene circuit design. Perhaps this is due to a more application-orientated shift in gene circuit design. Indeed, the earliest circuits recreated biologically useful but not obviously biotechnologically useful functions. In spite of this perceived shift, we believe that there are still many sources of naturally-inspired circuits that are broadly useful in biology AND biotechnology.

One such example comes from Williams et al.[9], where the authors recreated the terminal differentiation dynamics associated with many multicellular organisms, in *E. coli*. Specifically, unidirectional recombinase reactions were used to induce terminal differentiation of dividing progenitor cell into non-dividing cell expressing a burdensome or toxic function, essentially separating the replication roles and engineering function roles. Critically, this approach limited the propagation of mutants that lost the engineered function, enhancing the evolutionary stability of said function in a population — a critical aspect for many gene circuit applications such as bioprocessing.

Although this work is quite recent, it embodies the spirit of early work in gene circuits, where the authors aimed to recreate natural dynamics using components from different functional contexts. At the same time, it builds upon early work by showing these dynamics can be applied to an industrially relevant task. Overall, this work and others like it [10–13] are important demonstrations that nature can still be

an important source of inspiration for useful circuit behavior and design.

1.5 Overview of thesis

In this thesis we will present two projects that take direct inspiration from natural systems. Each project seeks to implement a naturally-existing behavior or circuit topology and use its unique dynamics to contribute towards solving various challenges in biotechnology.

In Chapters 2 and 3, we will present a circuit that emulates the natural dynamics of phase variation, whereby cells stochastically, and reversibly transition between several heritable, distinct phenotypic states. We successfully recreate this single-cell behavior using serine recombinases for up to three distinct phenotypes and characterize both its single cell and bulk dynamics. Further, we demonstrate that the uniquely stochastic single cell dynamics can lead to stable bulk dynamics and apply this phenomena to the task of controlling composition in mixed microbial cultures. We further speculate as to its utility in other organisms as well as its unique capacity for spatially-invariant composition control.

In Chapter 4, we will present the groundwork for applying one of the aforementioned feed-forward loops (FFL) topologies to the problem of signal filtering in biosensors. We posit that small activating trans RNAs (STARs) are a particularly useful tool for implementing these FFLs and characterize the design parameters of said STARs. We then demonstrate that STARs can successfully compose AND gates and FFLs. We provide a preliminary characterization of FFL dynamics and lay out the next steps required to bring this project to fruition. Finally, we conclude with closing remarks as to the future of gene circuit design and the interplay between naturally-inspired circuits and computational circuit design.

BIBLIOGRAPHY

1. Elowitz, M. B. & Leibler, S. A synthetic oscillatory network of transcriptional regulators. en. *Nature* **403.** Publisher: Nature Publishing Group, 335–338. ISSN: 1476-4687. https://www.nature.com/articles/35002125 (2025) (Jan. 2000).

2. Gardner, T. S., Cantor, C. R. & Collins, J. J. Construction of a genetic toggle switch in Escherichia coli. en. *Nature* **403.** Publisher: Nature Publishing Group, 339–342. ISSN: 1476-4687. https://www.nature.com/articles/35002131 (2025) (Jan. 2000).

3. Mangan, S. & Alon, U. Structure and function of the feed-forward loop network motif. EN. *Proceedings of the National Academy of Sciences* **100.** Company: National Academy of Sciences Distributor: National Academy of Sciences Institution: National Academy of Sciences Label: National Academy of Sciences Publisher: Proceedings of the National Academy of Sciences, 11980–11985. https://www.pnas.org/doi/abs/10.1073/pnas.2133841100 (2025) (Oct. 2003).

4. Nielsen, A. A. K., Der, B. S., Shin, J., Vaidyanathan, P., Paralanov, V., Strychalski, E. A., Ross, D., Densmore, D. & Voigt, C. A. Genetic circuit design automation. eng. *Science (New York, N.Y.)* **352,** aac7341. ISSN: 1095-9203 (Apr. 2016).

5. Tabor, J. J., Salis, H., Simpson, Z. B., Chevalier, A. A., Levskaya, A., Marcotte, E. M., Voigt, C. A. & Ellington, A. D. A Synthetic Genetic Edge Detection Program. *Cell* **137,** 1272–1281. ISSN: 0092-8674. https://www.ncbi.nlm.nih.gov/pmc/articles/PMC2775486/ (2025) (June 2009).

6. Ma, W., Trusina, A., El-Samad, H., Lim, W. A. & Tang, C. Defining Network Topologies that Can Achieve Biochemical Adaptation. *Cell* **138,** 760–773. ISSN: 0092-8674. https://www.sciencedirect.com/science/article/pii/S0092867409007120 (2025) (Aug. 2009).

7. Bhamidipati, P. S. & Thomson, M. *Designing biochemical circuits with tree search* en. Pages: 2025.01.27.635147 Section: New Results. Jan. 2025. https://www.biorxiv.org/content/10.1101/2025.01.27.635147v1 (2025).

8. Rai, K., O'Connell, R. W., Piepergerdes, T. C., Wang, Y., Brown, L. B. C., Samra, K. D., Wilson, J. A., Lin, S., Zhang, T. H., Ramos, E. M., Sun, A., Kille, B., Curry, K. D., Rocks, J. W., Treangen, T. J., Mehta, P. & Bashor, C. J. *Ultra-high throughput mapping of genetic design space* en. Pages: 2023.03.16.532704 Section: New Results. May 2025. https://www.biorxiv.org/content/10.1101/2023.03.16.532704v3 (2025).

9. Williams, R. L. & Murray, R. M. Integrase-mediated differentiation circuits improve evolutionary stability of burdensome and toxic functions in E. coli. en. *Nature Communications* **13.** Publisher: Nature Publishing Group, 6822. ISSN: 2041-1723. https://www.nature.com/articles/s41467-022-34361-y (2025) (Nov. 2022).

10. Zhu, R., del Rio-Salgado, J. M., Garcia-Ojalvo, J. & Elowitz, M. B. Synthetic multistability in mammalian cells. *Science* **375.** Publisher: American Association for the Advancement of Science, eabg9765. https://www.science.org/doi/10.1126/science.abg9765 (2025) (Jan. 2022).

11. Ziesack, M., Gibson, T., Oliver, J. K. W., Shumaker, A. M., Hsu, B. B., Riglar, D. T., Giessen, T. W., DiBenedetto, N. V., Bry, L., Way, J. C., Silver, P. A. & Gerber, G. K. Engineered Interspecies Amino Acid Cross-Feeding Increases Population Evenness in a Synthetic Bacterial Consortium. en. *mSystems* **4** (ed Collins, C. H.) e00352–19. ISSN: 2379-5077. https://journals.asm.org/doi/10.1128/mSystems.00352-19 (2025) (Aug. 2019).

12. Kerner, A., Park, J., Williams, A. & Lin, X. N. A Programmable Escherichia coli Consortium via Tunable Symbiosis. en. *PLoS ONE* **7** (ed Sandler, S. J.) e34032. ISSN: 1932-6203. https://dx.plos.org/10.1371/journal.pone.0034032 (2025) (Mar. 2012).

13. Scott, S. R., Din, M. O., Bittihn, P., Xiong, L., Tsimring, L. S. & Hasty, J. A stabilized microbial ecosystem of self-limiting bacteria using synthetic quorum-regulated lysis. en. *Nature Microbiology* **2.** Publisher: Nature Publishing Group, 1–9. ISSN: 2058-5276. https://www.nature.com/articles/nmicrobiol201783 (2025) (June 2017).

Chapter 2

DEVELOPMENT AND EXAMINATION OF A SYNTHETIC 2-STATE PHASE VARIATION SYSTEM

The work described in this chapter is currently under review in Nature Communications under the attribution:

Kratz M.F., Elowitz M.B., Murray, R.M. Synthetic Phase Variation for Engineered Microbial Consortia. *bioRxiv* 2025.08.25.672192;
https://doi.org/10.1101/2025.08.25.672192.

2.1 Introduction

Consortia are communities composed of multiple distinct cell types[1–3] that coordinate their individual behavior to achieve a community-level function. Consortia could implement more complex functions than single strain systems, and enable applications in metabolic engineering and biomanufacturing[4–8]. To this end, a major research goal in microbial synthetic biology has been to extend synthetic gene networks to the consortia level. The standard way to create a consortium is to co-culture several distinct microbial strains implementing separate parts of an overall function[1–3, 7], such as metabolic synthesis of a chemical (Figure 2.1a, left). In such systems, optimizing the overall consortium function requires a mechanism to optimize and maintain stable strain composition[1, 5, 9]. One approach is to use naturally symbiotic strains. However, many applications favor engineered and specialized lab strains[10, 11]. As a result, even small differences in the growth rates of the individual strains can drastically shift the composition[2, 3, 7] (Figure 2.1b, left).

Several approaches have been introduced to control consortium composition. One approach is to establish feedback on population sizes through intercellular signaling systems (Figure 2.1a, center, Figure 2.1b right)[12–18]. Broadly speaking, each consortium member secretes a member-specific signal that influences the growth or death rates of other members. For instance, auxotrophic *E. coli* mutants were used to create pairs of strains that complement each other's growth through cross-feeding of essential metabolites[18]. Metabolites secreted from one auxotrophic strain directly stimulate the growth of a complementary auxotrophic strain, favoring

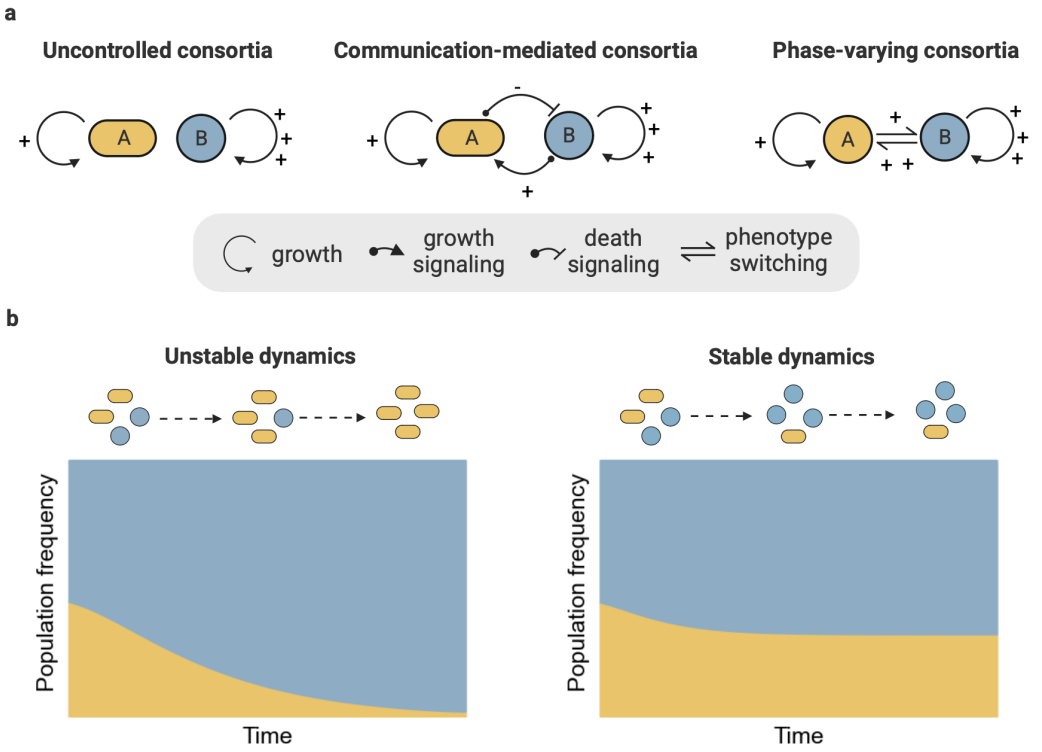

Figure 2.1: **Mechanisms and dynamics of microbial consortia implementations**. **a**, Schematics of different microbial consortia implementations: (left) no composition control, (middle) communication-based composition control, where growth and death are mediated via cell to cell signaling, and (right) phase-varying consortia, where each cell stochastically switches between phenotypic states. **b**, Bulk population dynamics of consortia implementations. In an uncontrolled system, the fastest growing strain dominates the culture (unstable dynamics). Both the communication-mediated and phase-varying consortia balance all strains, achieving stable dynamics. Blue and yellow represent distinct states, while shapes (circle, oval) represent distinct strains.

co-existence. In this case, the metabolites act as signals and controllers of growth rates. Recent implementations have expanded the repertoire of metabolites used this way[15] and exploited quorum sensing molecules and toxin-antitoxin systems for communication and death control[12, 13, 16], respectively. These approaches allow for inter-species consortia but require accurate communication between members to properly function[1, 4]. As such, their performance can be compromised in non-well-mixed settings, e.g. industrial bioreactors[19] or human gut[20]. Furthermore, they rely on a limited set of orthogonal communication channels, making scaling to many members difficult. Hence, these communication-mediated approaches have substantial limitations in terms of their scalability and suitability for non-well-mixed deployment contexts.

Another recent class of approaches addresses this scaling issue by emulating stem cell differentiation dynamics and removing the need for intercellular communication[21–23]. In these approaches, a consortium starts as a set of undifferentiated progenitor cells and progressively shifts to a community of terminally differentiated cells. Recently, *An et al.* used several orthogonal serine recombinases to mediate differentiation into a series of terminal cell types from a single founder cell type[23]. By manipulating the nucleotide sequence of recombinase attachment sites, the precise ratio of the terminal cell types could be manipulated. This approach is scalable to many phenotypes, but is limited by depletion of the progenitor pool and lacks closed-loop feedback control of overall cell fate proportions.

What approaches could allow for scalable and continual composition control without relying on intercellular communication? In the natural process of phase variation, cells stochastically and reversibly transition between distinct phenotypic states, each conferring distinct fitness benefits and costs[24, 25]. Phase variation facilitates survival in environments with abrupt and stochastic changes in selection pressure[24–26]. Here, we implement a synthetic version of phase variation in which a single strain encodes a set of mutually exclusive states, with each individual cell stochastically and reversibly switching between these states (Figure 2.1a, right, Figure 2.1b right). By controlling state transition rates, the system allows tuning of the steady-state distribution. In this approach, there is no requirement for intercellular communication and cells have access to all states at all times. These features make this system amenable to continuous control of composition.

We first used mathematical modeling to demonstrate that the dynamics of phase variation can stabilize otherwise unstable consortium configurations. We then

designed circuits that exploit reversible recombinase flipping to switch between mutually exclusive phenotypic states. Next, we experimentally constructed this design, showing it can balance the abundances of two distinct states. Finally, through the addition of a secondary orthogonal recombinase, we demonstrated that synthetic phase variation can be scaled to control the proportions of three distinct states. This work establishes a communication-free, scalable architecture for continuous control of consortia composition, opening the door to applications of consortia in otherwise inaccessible contexts.

2.2 Results

Phase variation stabilizes otherwise unstable consortium *in silico*

We first demonstrated through mathematical modeling that phase variation can be a viable method of composition control for microbial consortia. To model the competitive exclusion dynamics that drive instabilities in consortia, we used a chemostat as the base of our ordinary differential equation model. In such a framework, individual strains grow and multiply via a common, constantly replenishing substrate resource, creating competition between strains for this limited resource.

Building a chemostat model for examining phase variation

Let us first consider how one may model a single strain (A) growing through consumption of a substrate (S) in a chemostat environment. In abstracted terms one may expect the dynamics in Equation 1 for said species:

$$\frac{dA}{dt} = Growth - Death - Outflow$$

$$\frac{dS}{dt} = Substrate\ Inflow - Substrate\ Outflow + Substrate\ Consumption \tag{1}$$

A experiences change due to cell growth/division, death, or outflow from the chemostat mechanism. Previous research has shown individual cell death to be a rare event and to be the result of accumulated damage [27] Because cells are consistently exiting the chemostat, we will assume death to be a negligible source of change in A. The levels of S will change due to fresh media inflow, partially spent media outflow and consumption of substrate by cells for the process of replication. Due

to the mechanism of a chemostat, this inflow term should be equal to the outflow term. We will now ascribe mathematical forms to each of these sources of change in Equation 2:

$$\begin{aligned}
\frac{dA}{dt} &= \left(\frac{\mu_a S}{K_a + S} - D \right) A, \\
\frac{dS}{dt} &= D(S_0 - S) - \left(\frac{\mu_a S}{K_a + S} \frac{A}{\gamma_a} + \frac{\mu_b S}{K_b + S} \frac{B}{\gamma_b} \right).
\end{aligned} \tag{2}$$

For the dynamics of A, cell growth is represented with a Monod model [28] and outflow is represented with a dilution term (D) applied to A. For the dynamics of S, substrate inflow and outflow are represented by the dilution term applied to the relevant substrate source (fresh, S_0 or spent media, S). Finally, substrate transformation into biomass is effectively the growth process from $\frac{dA}{dt}$ scaled by a yield term γ_a which describes the efficiency by which substrate is converted to cell mass. We can now add a second strain, using the same exact dynamics as for the first strain, creating a model that should exhibit competitive exclusion dynamics.

$$\begin{aligned}
\frac{dA}{dt} &= \left(\frac{\mu_a S}{K_a + S} - D \right) A, \\
\frac{dB}{dt} &= \left(\frac{\mu_b S}{K_b + S} - D \right) B, \\
\frac{dS}{dt} &= D(S_0 - S) - \left(\frac{\mu_a S}{K_a + S} \frac{A}{\gamma_a} + \frac{\mu_b S}{K_b + S} \frac{B}{\gamma_b} \right).
\end{aligned}$$

We can introduce the phase variation dynamics associated with our 2-state circuit (highlighted in red). To model state transitions, we use simple linear switching terms (β_j) applied to the relevant species:

$$\frac{dA}{dt} = \left(\frac{\mu_a S}{K_a + S} - D \right) A + \beta_1 B - \beta_2 A,$$

$$\frac{dB}{dt} = \left(\frac{\mu_b S}{K_b + S} - D \right) B + \beta_2 A - \beta_1 B,$$

$$\frac{dS}{dt} = D(S_0 - S) - \left(\frac{\mu_a S}{K_a + S} \frac{A}{\gamma_a} + \frac{\mu_b S}{K_b + S} \frac{B}{\gamma_b} \right).$$

In this final model, μ_i,γ_im and K_i are the maximum growth rate, yield constant, and half-velocity constant for a given state i, respectively. S_0 and D, are the inlet substrate concentration and flow rate, respectively. Finally, β_j is the switching rate associated with a given transition. Using non-dimensionalization we can reframe the system of equations and reduce the number of parameters to create the system in Equation 3:

$$\frac{d\mathbf{A}}{d\boldsymbol{t}} = \left(\frac{\boldsymbol{S}}{1 + \boldsymbol{S}} - \overline{D} \right) \mathbf{A} + \overline{\beta_1} \mathbf{B} - \overline{\beta_2} \mathbf{A},$$

$$\frac{d\mathbf{B}}{d\boldsymbol{t}} = \left(\frac{\overline{\mu_b}\overline{K_b}\boldsymbol{S}}{1 + \overline{K_b}\boldsymbol{S}} - \overline{D} \right) \mathbf{B} + \overline{\beta_2} \mathbf{A} - \overline{\beta_1} \mathbf{B},$$

$$\frac{d\boldsymbol{S}}{d\boldsymbol{t}} = \overline{D} \left(\overline{S_0} - \boldsymbol{S} \right) - \left(\frac{\boldsymbol{S}}{1 + \boldsymbol{S}} \mathbf{A} + \frac{\overline{\mu_b}\overline{K_b}\boldsymbol{S}}{1 + \overline{K_b}\boldsymbol{S}} \frac{\mathbf{B}}{\overline{\gamma_b}} \right), \tag{3}$$

$$\overline{D} = \frac{D}{\mu_a}, \quad \overline{\beta_j} = \frac{\beta_j}{\mu_a}, \quad \overline{\mu_b} = \frac{\mu_b}{\mu_a}, \quad \overline{K_b} = \frac{K_a}{K_b}, \quad \overline{S_0} = \frac{S_o}{K_a}, \quad \overline{\gamma_b} = \frac{\gamma_b}{\gamma_c}.$$

Examining phase variation with our chemostat model

Under what circumstances can stochastic switching establish a stable consortium? Using the previously described framework, we first examined the case of an uncontrolled consortium with two competing strains, each fixed in a distinct state, A or B.

For example, if strain B grows at a 30% faster rate than strain A, and both strains are seeded at equal concentrations, the combination of growth rate differences and limiting nutrient leads strain B to progressively overtake the mixed culture (Fig. 2a). Thus, in the absence of additional control mechanisms, the consortium is unstable.

Phase variation mitigates this issue. To explore this, we added a secondary layer of phase variation dynamics to the model. In this case, the two phenotypic states, A and B, interconvert, with switching rates[29–31] β_1 or β_2 for B-to-A, or A-to-B transitions, respectively (Fig. 2b). Transitions compensate for the growth advantage of B, allowing for stable coexistence of both states in simulations. Parameters used in these simulations can be found in Table S1.

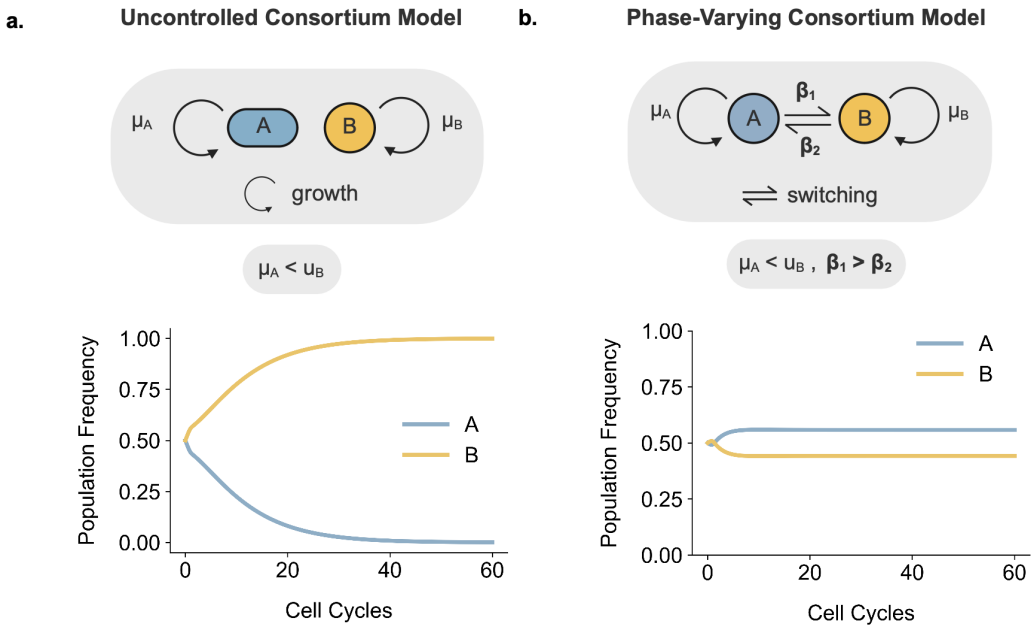

Figure 2.2: **Phase variation stabilizes consortium composition**. **a** Uncontrolled consortium model schematic and simulation results. **b** Phase-varying consortium model schematic and simulation results. Presented results and parameters are non-dimensionalized and scaled to the growth rate of strain/phenotype A.

We may also derive the steady state phenotype ratio (r) of our system. If we assume that both strains have the same yield constants and half-velocity constants i.e. $\overline{K_b} = \overline{\gamma_b} = 1$, then at steady state, we can derive the following expressions:

$$0 = \left(X \ - \overline{D} \ - \overline{\beta_2} \right) r + \overline{\beta_1},$$

$$0 = \left(\overline{\mu_b} X \ - \overline{D} \ - \overline{\beta_1} \right) + \overline{\beta_2} r,$$

$$X \ = \ \frac{\boldsymbol{S}}{1 + \boldsymbol{S}} \ , \ r \ = \ \frac{\mathbf{A}^*}{\mathbf{B}^*}.$$

We can solve for X for one expression and subsequently substitute it into the second expression, resulting in the following quadratic, with the solution in Equation 4:

$$r = \frac{\overline{D} \ + \overline{\beta_1} \ - \ \overline{\mu_b} \ \left(\overline{D} \ + \overline{\beta_2} - \frac{\overline{\beta_1}}{r} \right)}{\overline{\beta_2}},$$

$$0 = \ \overline{\beta_2} r^2 \ - \ \left[(1 - \ \overline{\mu_b}) \, \overline{D} \ + \ \overline{\beta_1} \ - \overline{\mu_b} \, \overline{\beta_2} \right] r \ - \overline{\mu_b} \, \overline{\beta_1},$$

$$r \ = \frac{\alpha \ + \ \sqrt[2]{\alpha^2 \ + \ 4 \overline{\mu_b} \, \overline{\beta_1} \, \overline{\beta_2}}}{2 \overline{\beta_2}}, \tag{4}$$

$$\alpha \ = \ (1 - \ \overline{\mu_b}) \, \overline{D} \ + \ \overline{\beta_1} \ - \overline{\mu_b} \, \overline{\beta_2}.$$

The square root term will be strictly positive for all physical parameter values. Further this square root term will always be larger than α^2 for positive $\overline{\mu_b}, \overline{\beta_1}, \overline{\beta_2}$, hence for any system where switching occurs, we only need to consider the positive root. Thus, r takes on a unique population ratio that can be modulated by tuning switching rates (Figure S1). Overall, these numerical simulations and analytical results demonstrate how phase variation can force co-existence in an otherwise unstable consortia and allow to tune the relative abundance of consortia members.

A recombinase circuit can drive 2-state phase variation dynamics

Having demonstrated that phase variation dynamics can stabilize consortia *in silico,* we sought to design an experimental circuit that implements phase variation. The ideal circuit would rely on well-characterized components with multiple orthogonal variants to enable scalable engineering of systems with multiple states. We designed a DNA cassette which encodes two mutually exclusive transcriptional states, one corresponding to YFP[32] expression and the other to mTurquoise[33] expression (Figure 2.3a). Both fluorophores were tagged with the ssrA degradation tag[34], shortening their half-lives to accelerate circuit readout dynamics[32]. To allow transitions, we also incorporated serine recombinases, viral proteins that catalyze site specific DNA rearrangements[35]. We flanked the cassette with two antiparallel Bxb1 serine recombinase attachment sites. When Bxb1 binds to these sites, it catalyzes inversion of the intervening DNA sequence, switching expression from YFP to mTurquoise. This reaction can be reversed by Bxb1 in complex with its cognate reverse directionality factor (RDF)[36]. By regulating the concentrations of Bxb1 and its RDF, one can influence the frequency and bias of these flipping reactions[37]. Analogous constructs have been previously used as rewritable DNA storage[38–40] or to tune expression variation of a single gene[41].

After constructing this circuit, we experimentally probed its single cell dynamics using the 'mother machine' microfluidic device[27, 42–45] (Figure 2.3b). This device consists of a series of growth channels perpendicular to a trench through which fresh media flows, providing a chemostatic environment and allowing long term monitoring of individual "mother" cells at the ends of each channel. This device thus allows one to probe the long term switching dynamics of single cells under steady state conditions.

When observed in the mother machine, individual cells stably expressed a single fluorophore for multiple cell cycles, while occasionally switching to the other state. We can see an example of this switching process in Figure 2.3c, in which a cell switches from mTurquoise to YFP fluorescence (Supplemental Movie 1). It is important to note that in this instance, the mother cell seems to spend relatively little time in a mixed YFP-mTurquoise state, existing primarily in one of the two states exclusively.

To further probe the switching dynamics, we tracked the distribution of residence times, defined as how long the cell spends in a given state before switching (Figure 2.3d). Both states displayed a wide distribution of residence times. Because the

switching rates were unequal, cells spent more time in the YFP state (residence time of 521 min., s.d. 300 min) than the mTurquoise state (174 min., s.d. 119 min). Furthermore, consistent with the kymograph observations, the YFP and mTurquoise states were exclusive, with cells spending relatively little time in transitional states expressing both proteins. The residence times were exponentially distributed for both the mTurquoise and YFP states, but with different time constants, consistent with our expectation of a generative Poisson process for switching (Fig. S2).

Varying expression of recombinase elements enables stable, bulk composition control

We next sought to tune the state composition of the population. We placed Bxb1 and Bxb1 RDF under the control of salicylate (sal) and Isopropyl-β-d-thiogalactoside (IPTG) inducible promoters[46], respectively, on a p15a plasmid (Figure 2.4a). With these constructs, the transition rates that govern the bulk cell population dynamics should be tunable, allowing for bulk-scale control of composition.

We used the mother machine to observe population dynamics under YFP-biased (0 µM sal, 250 µM IPTG) and Turquoise-biased (4 µM sal, 10 µM IPTG) inducer conditions. The circuit was strongly biased to the mTurquoise state in the absence of inducers due to basal Bxb1 expression. Upon induction, the distribution of cell states rapidly shifted to a new steady-state composition (Figure 2.4b, Fig. S3-S4). Within ~19 hours both conditions reached 95% of the steady-state composition value. Additionally, we tracked the frequency of mixed-state cells during these runs (Figure S5) and noted that at steady state, the frequency of these cells remained ~5%, further supporting our previous findings that most cells exist in a single expression state. Together, these results indicate that Bxb1 and RDF expression levels can tune the population composition.

To rapidly explore a broader range of inducer concentrations, we switched to a turbidostat-plate reader setup that allows greater multiplexing (Figure 2.4c). The non-chemostatic plate reader conditions also provided an opportunity to examine circuit operation in a distinct, batch culture growth context.

For plate reader experiments, we explored a matrix of 3 initial compositions, each induced with one of 5 different inducer concentrations, for a total of 15 individual culture trajectories (Figure 2.4d, Fig. S7-S11). For each inducer concentration, cultures approached the same final steady state distribution regardless of initial conditions, and did so over a similar timescale (Figure 2.4d). Final compositions

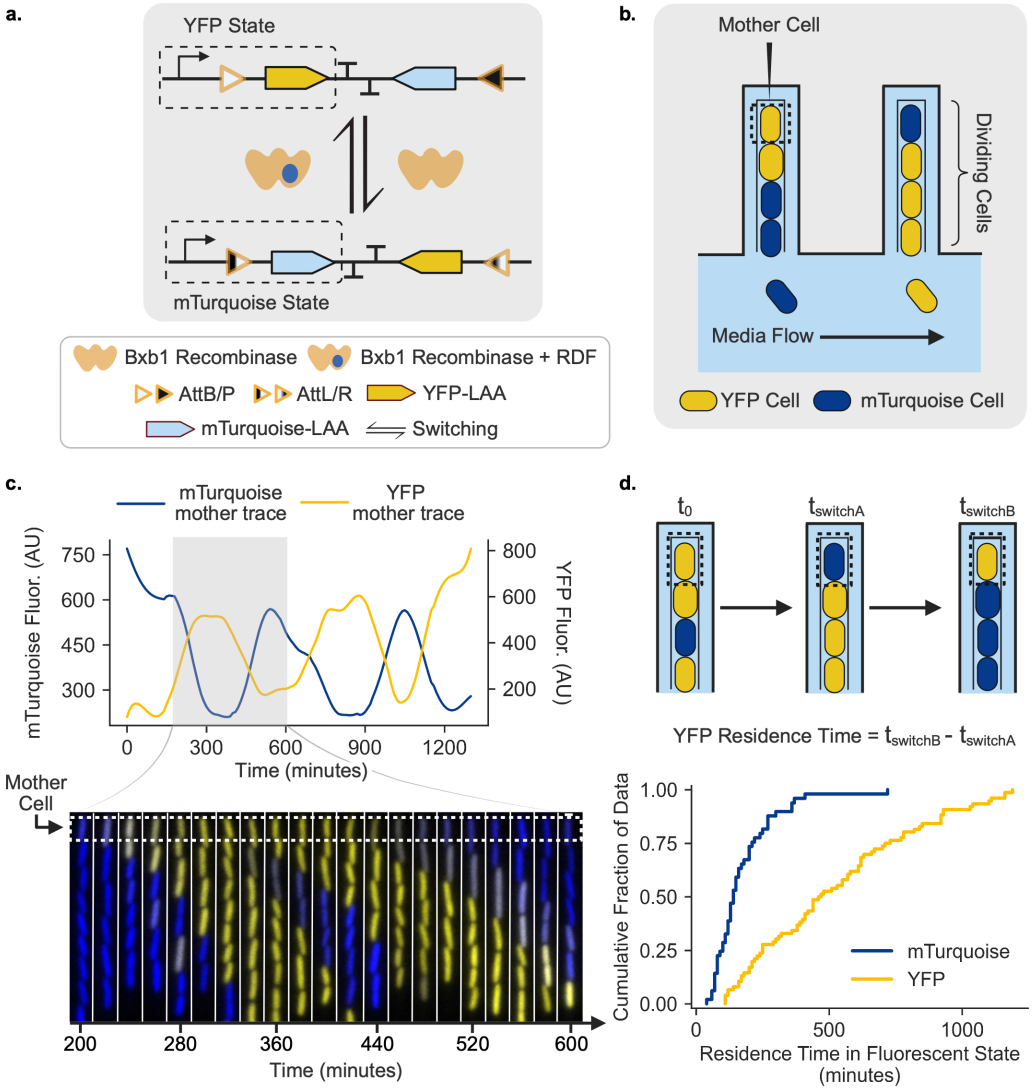

Figure 2.3: **A recombinase circuit successfully recreates single cell phase variation dynamics.** **a**, Recombinase switching construct schematic. The arrows represent state transitions, with Bxb1 or the Bxb1-RDF complex catalyzing transitions. Bxb1 recombinase was destabilized using the LAA ClpXP degradation tag[34]. This construct was integrated as a single copy in the genome. Bxb1 and RDF were expressed under inducible control from a separate plasmid. **b**, Mother machine schematic. The cell at the end of the growth channel (mother cell), remains in the channel indefinitely and can be tracked for many generations **c**, Mother machine kymograph and single mother cell fluorescence trace. Successive images in the kymograph are separated by twenty minute intervals. The highlighted grey section in the trace corresponds to the time frame associated with the kymograph movie. **d**, Schematic defining residence times and cumulative distribution of mother cell residence times. Data were collected by manual observation of mother cells.

spanned a ~100-fold range of population ratios, and were tunable within this range. In a negative control experiment, we performed a similar analysis on a 2-strain (non-switching) system. In this case, cultures were overtaken by the YFP expressing strain (Fig. S6), indicating that the circuit is required to stabilize mixed compositions.

The time to reach 95% of the steady state was noticeably longer in the plate reader (~19 h) compared to the mother machine (~26 h). However, the final compositions were similar between the two environments: 1.08 vs. 1.05 for the YFP-biased condition and -0.91 vs. -0.66 for the mTurquoise-biased condition. Taken together, these results demonstrated continuous control of bulk composition dynamics.

2.3 Discussion

Previous work has used recombinase circuits to tune phenotypic variation of a single phenotypic state expressing GFP (ON/OFF). Additionally, control of two distinct genetic states has been demonstrated via toggle switch dynamics. However, it has remained unclear if a recombinase approach could tune phenotypic variation for multiple distinct states, and improve upon the tunability and scalability of previous toggle switch approaches.

In this chapter we demonstrated *in silico* that the addition of switching dynamics can stabilize otherwise unstable consortia. Subsequently, we proposed a realized a recombinase circuit that recreated the single cell, stochastic switching dynamics associated with microbial phase variation, with consistent switching and minimal state crossover. Finally, we demonstrated the through tunable expression of recombinase elements, one can achieve fine control of bulk composition that is transferable across two distinct media and growth contexts.

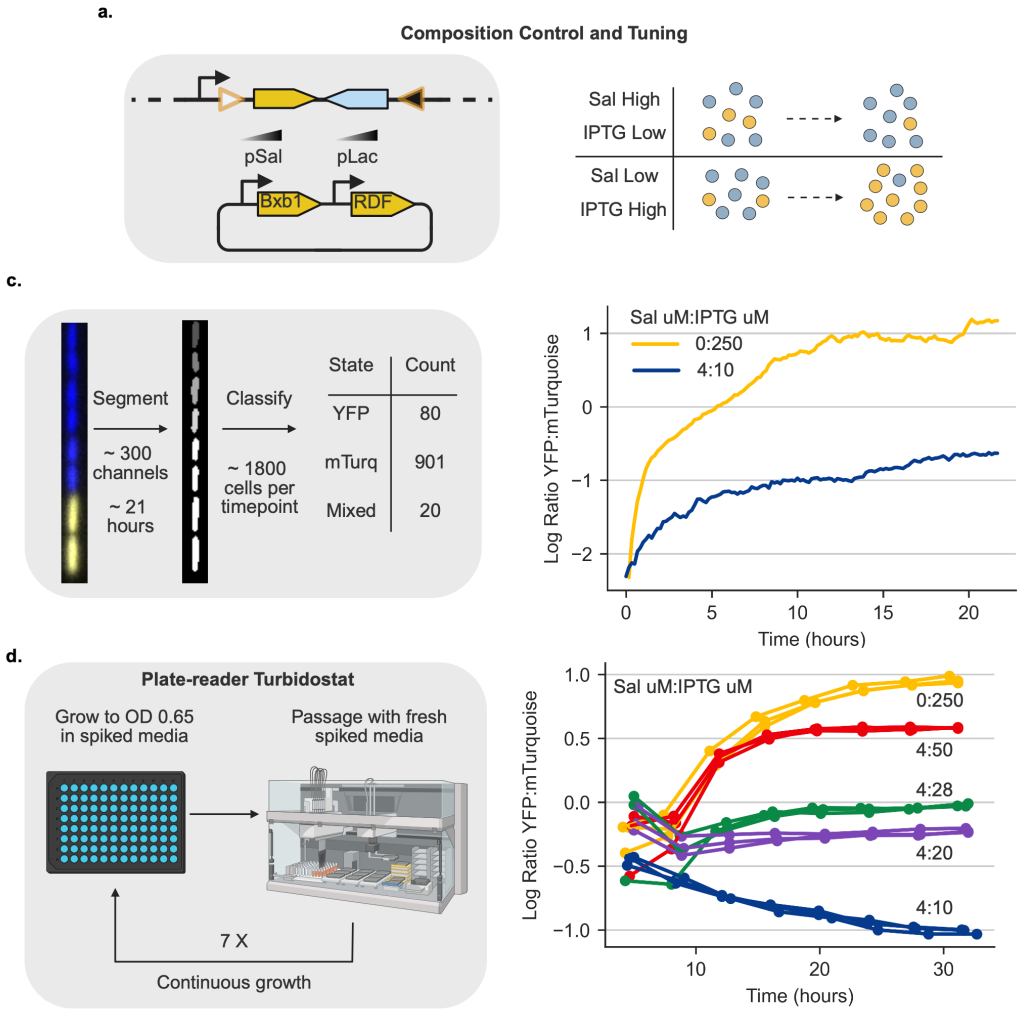

Figure 2.4: **Synthetic phase variation enables bulk composition control in diverse growth contexts a**, 2-state composition control schematic. The recombinase switching construct was located in a single copy on the genome and the recombinase elements were expressed from a p15a plasmid. Bxb1 is controlled by a salicylate inducible promoter (pSal) and its cognate RDF is controlled by an IPTG inducible promoter pTac. By varying inducer levels, the steady state composition of the system should be tunable. **b**, Mother machine processing pipeline and bulk population dynamics. Cells are sorted into YFP and mTurquoise categories based on the median fluorescent signal ratio of the relevant channels. Traces start in a heavily mTurquoise biased state due to leak associated with the Bxb1 recombinase. The inducer concentrations used for each experiment are labeled next to each trace. Individual population traces can be found in Figures S2-S3. **c**, Plate reader turbidostat setup and bulk population dynamics. Traces of the same color are cultured in the same media and expected to end at the same final composition. The inducer concentrations used for each experiment are labeled next to each trace. Due to the dynamics of degradation-tagged fluorophores in batch cultures, the maximum value for each fluorophore channel in each cycle was used to calculate composition. Signals are normalized to the max fluorescence possible for a given channel e.g. YFP is normalized to an all YFP culture.

BIBLIOGRAPHY

1. McCarty, N. S. & Ledesma-Amaro, R. Synthetic Biology Tools to Engineer Microbial Communities for Biotechnology. eng. *Trends in Biotechnology* **37,** 181–197. ISSN: 1879-3096 (Feb. 2019).

2. Brenner, K., You, L. & Arnold, F. H. Engineering microbial consortia: a new frontier in synthetic biology. English. *Trends in Biotechnology* **26.** Publisher: Elsevier, 483–489. ISSN: 0167-7799, 1879-3096. https://www.cell.com/trends/biotechnology/abstract/S0167-7799(08)00171-6 (2025) (Sept. 2008).

3. Duncker, K. E., Holmes, Z. A. & You, L. Engineered microbial consortia: strategies and applications. *Microbial Cell Factories* **20,** 211. ISSN: 1475-2859. https://doi.org/10.1186/s12934-021-01699-9 (2025) (Nov. 2021).

4. Roell, G. W., Zha, J., Carr, R. R., Koffas, M. A., Fong, S. S. & Tang, Y. J. Engineering microbial consortia by division of labor. *Microbial Cell Factories* **18,** 35. ISSN: 1475-2859. https://doi.org/10.1186/s12934-019-1083-3 (2025) (Feb. 2019).

5. Mittermeier, F., Bäumler, M., Arulrajah, P., García Lima, J. d. J., Hauke, S., Stock, A. & Weuster-Botz, D. Artificial microbial consortia for bioproduction processes. en. *Engineering in Life Sciences* **23,** e2100152. ISSN: 1618-2863. https://onlinelibrary.wiley.com/doi/abs/10.1002/elsc.202100152 (2025) (2023).

6. Jawed, K., Yazdani, S. S. & Koffas, M. A. Advances in the development and application of microbial consortia for metabolic engineering. *Metabolic Engineering Communications* **9,** e00095. ISSN: 2214-0301. https://www.sciencedirect.com/science/article/pii/S2214030118300440 (2025) (Dec. 2019).

7. Bhatia, S. K., Bhatia, R. K., Choi, Y.-K., Kan, E., Kim, Y.-G. & Yang, Y.-H. Biotechnological potential of microbial consortia and future perspectives. *Critical Reviews in Biotechnology* **38.** Publisher: Taylor & Francis _eprint: https://doi.org/10.1080/07388551.2018.1471445, 1209–1229. ISSN: 0738-8551. https://doi.org/10.1080/07388551.2018.1471445 (2025) (Nov. 2018).

8. Xin, Y. & Qiao, M. Towards microbial consortia in fermented foods for metabolic engineering and synthetic biology. *Food Research International* **201,** 115677. ISSN: 0963-9969. https://www.sciencedirect.com/science/article/pii/S0963996925000134 (2025) (Feb. 2025).

9. Jiang, Y., Wu, R., Zhang, W., Xin, F. & Jiang, M. Construction of stable microbial consortia for effective biochemical synthesis. English. *Trends in Biotechnology* **41.** Publisher: Elsevier, 1430–1441. ISSN: 0167-7799, 1879-3096. https://www.cell.com/trends/biotechnology/abstract/S0167-7799(23)00155-5 (2025) (Nov. 2023).

10. Sagt, C. M. J. Systems metabolic engineering in an industrial setting. en. *Applied Microbiology and Biotechnology* **97,** 2319–2326. ISSN: 1432-0614. https://doi.org/10.1007/s00253-013-4738-8 (2025) (Mar. 2013).

11. Sun, J. & Alper, H. S. Metabolic engineering of strains: from industrial-scale to lab-scale chemical production. *Journal of Industrial Microbiology and Biotechnology* **42,** 423–436. ISSN: 1367-5435. https://doi.org/10.1007/s10295-014-1539-8 (2025) (Mar. 2015).

12. Balagaddé, F. K., Song, H., Ozaki, J., Collins, C. H., Barnet, M., Arnold, F. H., Quake, S. R. & You, L. A synthetic Escherichia coli predator-prey ecosystem. eng. *Molecular Systems Biology* **4,** 187. ISSN: 1744-4292 (2008).

13. McCardell, R. D., Pandey, A. & Murray, R. M. *Control of density and composition in an engineered two-member bacterial community* en. Pages: 632174 Section: New Results. May 2019. https://www.biorxiv.org/content/10.1101/632174v1 (2025).

14. You, L., Cox, R. S., Weiss, R. & Arnold, F. H. Programmed population control by cell–cell communication and regulated killing. en. *Nature* **428.** Publisher: Nature Publishing Group, 868–871. ISSN: 1476-4687. https://www.nature.com/articles/nature02491 (2025) (Apr. 2004).

15. Kong, W., Meldgin, D. R., Collins, J. J. & Lu, T. Designing microbial consortia with defined social interactions. en. *Nature Chemical Biology* **14.** Publisher: Nature Publishing Group, 821–829. ISSN: 1552-4469. https://www.nature.com/articles/s41589-018-0091-7 (2025) (Aug. 2018).

16. Scott, S. R., Din, M. O., Bittihn, P., Xiong, L., Tsimring, L. S. & Hasty, J. A stabilized microbial ecosystem of self-limiting bacteria using synthetic quorum-regulated lysis. en. *Nature Microbiology* **2.** Publisher: Nature Publishing Group, 1–9. ISSN: 2058-5276. https://www.nature.com/articles/nmicrobiol201783 (2025) (June 2017).

17. Xu, P. Dynamics of microbial competition, commensalism, and cooperation and its implications for coculture and microbiome engineering. en. *Biotechnology and Bioengineering* **118,** 199–209. ISSN: 0006-3592, 1097-0290. https://onlinelibrary.wiley.com/doi/10.1002/bit.27562 (2025) (Jan. 2021).

18. Wintermute, E. H. & Silver, P. A. Emergent cooperation in microbial metabolism. *Molecular Systems Biology* **6.** Publisher: John Wiley & Sons, Ltd, 407. ISSN: 1744-4292. https://www.embopress.org/doi/full/10.1038/msb.2010.66 (2025) (Jan. 2010).

19. Lara, A. R., Galindo, E., Ramírez, O. T. & Palomares, L. A. Living with heterogeneities in bioreactors: understanding the effects of environmental gradients on cells. eng. *Molecular Biotechnology* **34,** 355–381. ISSN: 1073-6085 (Nov. 2006).

20. Labavić, D., Loverdo, C. & Bitbol, A.-F. Hydrodynamic flow and concentration gradients in the gut enhance neutral bacterial diversity. *Proceedings of the National Academy of Sciences* **119.** Publisher: Proceedings of the National Academy of Sciences, e2108671119. https://www.pnas.org/doi/10.1073/pnas.2108671119 (2025) (Jan. 2022).

21. Williams, R. L. & Murray, R. M. Integrase-mediated differentiation circuits improve evolutionary stability of burdensome and toxic functions in E. coli. en. *Nature Communications* **13.** Publisher: Nature Publishing Group, 6822. ISSN: 2041-1723. https://www.nature.com/articles/s41467-022-34361-y (2025) (Nov. 2022).

22. Aditya, C., Bertaux, F., Batt, G. & Ruess, J. A light tunable differentiation system for the creation and control of consortia in yeast. en. *Nature Communications* **12.** Publisher: Nature Publishing Group, 5829. ISSN: 2041-1723. https://www.nature.com/articles/s41467-021-26129-7 (2025) (Oct. 2021).

23. An, B., Tang, T.-C., Zhang, Q., Wang, T., Gan, K., Liu, K., Liu, Y., Wang, Y., Shaw, W. M., Liang, Q., Wang, Y., Lu, T. K., Church, G. M. & Zhong, C. *Synthetic ratio computation for programming population composition and multicellular morphology* en. Pages: 2024.11.26.624747 Section: New Results. Dec. 2024. https://www.biorxiv.org/content/10.1101/2024.11.26.624747v2 (2025).

24. Thattai, M. & van Oudenaarden, A. Stochastic Gene Expression in Fluctuating Environments. *Genetics* **167,** 523–530. ISSN: 1943-2631. https://doi.org/10.1534/genetics.167.1.523 (2025) (May 2004).

25. Van der Woude, M. W. & Bäumler, A. J. Phase and Antigenic Variation in Bacteria. *Clinical Microbiology Reviews* **17,** 581–611. ISSN: 0893-8512. https://www.ncbi.nlm.nih.gov/pmc/articles/PMC452554/ (2025) (July 2004).

26. Morawska, L. P., Hernandez-Valdes, J. A. & Kuipers, O. P. Diversity of bet-hedging strategies in microbial communities—Recent cases and insights. *Wires Mechanisms of Disease* **14,** e1544. ISSN: 2692-9368. https://www.ncbi.nlm.nih.gov/pmc/articles/PMC9286555/ (2025) (2022).

27. Wang, P., Robert, L., Pelletier, J., Dang, W. L., Taddei, F., Wright, A. & Jun, S. Robust Growth of Escherichia coli. English. *Current Biology* **20.** Publisher: Elsevier, 1099–1103. ISSN: 0960-9822. https://www.cell.com/current-biology/abstract/S0960-9822(10)00524-5 (2025) (June 2010).

28.

*"Bibliographie": p. [200]-210.*Monod, J. *Recherches sur la croissance des cultures bactériennes* (Hermann & cie, Paris, 1942).

29. Wolf, D. M., Vazirani, V. V. & Arkin, A. P. Diversity in times of adversity: probabilistic strategies in microbial survival games. *Journal of Theoretical Biology* **234,** 227–253. ISSN: 0022-5193. https://www.sciencedirect.com/science/article/pii/S0022519304005740 (2024) (May 2005).

30. Visco, P., Allen, R. J., Majumdar, S. N. & Evans, M. R. Switching and Growth for Microbial Populations in Catastrophic Responsive Environments. *Biophysical Journal* **98,** 1099–1108. ISSN: 0006-3495. https://www.ncbi.nlm.nih.gov/pmc/articles/PMC2849059/ (2024) (Apr. 2010).

31. Jia, C., Qian, M.-P., Kang, Y. & Jiang, D.-Q. *Modeling stochastic phenotype switching and bet-hedging in bacteria: stochastic nonlinear dynamics and critical state identification* arXiv:1311.2216 [q-bio]. Jan. 2015. http://arxiv.org/abs/1311.2216 (2025).

32. Pédelacq, J.-D., Cabantous, S., Tran, T., Terwilliger, T. C. & Waldo, G. S. Engineering and characterization of a superfolder green fluorescent protein. en. *Nature Biotechnology* **24.** Publisher: Nature Publishing Group, 79–88. ISSN: 1546-1696. https://www.nature.com/articles/nbt1172 (2025) (Jan. 2006).

33. Goedhart, J., von Stetten, D., Noirclerc-Savoye, M., Lelimousin, M., Joosen, L., Hink, M. A., van Weeren, L., Gadella, T. W. J. & Royant, A. Structure-guided evolution of cyan fluorescent proteins towards a quantum yield of 93%. en. *Nature Communications* **3.** Publisher: Nature Publishing Group, 751. ISSN: 2041-1723. https://www.nature.com/articles/ncomms1738 (2025) (Mar. 2012).

34. Jadhav, P., Chen, Y., Butzin, N., Buceta, J. & Urchueguía, A. Bacterial degrons in synthetic circuits. *Open Biology* **12.** Publisher: Royal Society, 220180. https://royalsocietypublishing.org/doi/10.1098/rsob.220180 (2025) (Aug. 2022).

35. Stark, W. M. Making serine integrases work for us. en. *Current Opinion in Microbiology. Mobile genetic elements and HGT in prokaryotes * Microbiota* **38,** 130–136. ISSN: 1369-5274. https://www.sciencedirect.com/science/article/pii/S1369527417300206 (2022) (Aug. 2017).

36. Olorunniji, F. J., Buck, D. E., Colloms, S. D., McEwan, A. R., Smith, M. C. M., Stark, W. M. & Rosser, S. J. Gated rotation mechanism of site-specific recombination by phiC31 integrase. *Proceedings of the National Academy of Sciences* **109.** Publisher: Proceedings of the National Academy of Sciences, 19661–19666. https://www.pnas.org/doi/10.1073/pnas.1210964109 (2025) (Nov. 2012).

37. Durrant, M. G., Fanton, A., Tycko, J., Hinks, M., Chandrasekaran, S. S., Perry, N. T., Schaepe, J., Du, P. P., Lotfy, P., Bassik, M. C., Bintu, L., Bhatt, A. S. & Hsu, P. D. Systematic discovery of recombinases for efficient integration of large DNA sequences into the human genome. en. *Nature Biotechnology* **41.** Publisher: Nature Publishing Group, 488–499. ISSN: 1546-1696. https://www.nature.com/articles/s41587-022-01494-w (2025) (Apr. 2023).

38. Bonnet, J., Subsoontorn, P. & Endy, D. Rewritable digital data storage in live cells via engineered control of recombination directionality. *Proceedings of the National Academy of Sciences* **109.** Publisher: Proceedings of the National Academy of Sciences, 8884–8889. https://www.pnas.org/doi/10.1073/pnas.1202344109 (2022) (June 2012).

39. Huang, B. D., Kim, D., Yu, Y. & Wilson, C. J. Engineering intelligent chassis cells via recombinase-based MEMORY circuits. en. *Nature Communications* **15.** Publisher: Nature Publishing Group, 2418. ISSN: 2041-1723. https://www.nature.com/articles/s41467-024-46755-1 (2025) (Mar. 2024).

40. Yang, L., Nielsen, A. A. K., Fernandez-Rodriguez, J., McClune, C. J., Laub, M. T., Lu, T. K. & Voigt, C. A. Permanent genetic memory with >1-byte capacity. en. *Nature Methods* **11.** Number: 12 Publisher: Nature Publishing Group, 1261–1266. ISSN: 1548-7105. https://www.nature.com/articles/nmeth.3147 (2022) (Dec. 2014).

41. Hung, M., Chang, E., Hussein, R., Frazier, K., Shin, J.-E., Sagawa, S. & Lim, H. N. Modulating the frequency and bias of stochastic switching to control phenotypic variation. en. *Nature Communications* **5.** Publisher: Nature Publishing Group, 4574. ISSN: 2041-1723. https://www.nature.com/articles/ncomms5574 (2025) (Aug. 2014).

42. Bakshi, S., Leoncini, E., Baker, C., Cañas-Duarte, S. J., Okumus, B. & Paulsson, J. Tracking bacterial lineages in complex and dynamic environments with applications for growth control and persistence. *Nature microbiology* **6,** 783–791. ISSN: 2058-5276. https://www.ncbi.nlm.nih.gov/pmc/articles/PMC10277933/ (2025) (June 2021).

43. Luro, S., Potvin-Trottier, L., Okumus, B. & Paulsson, J. Isolating live cells after high-throughput, long-term, time-lapse microscopy. *Nature methods* **17,** 93–100. ISSN: 1548-7091. https://www.ncbi.nlm.nih.gov/pmc/articles/PMC7525750/ (2025) (Jan. 2020).

44. Sauls, J. T., Cox, S. E., Do, Q., Castillo, V., Ghulam-Jelani, Z. & Jun, S. Control of Bacillus subtilis Replication Initiation during Physiological Transitions and Perturbations. *mBio* **10.** Publisher: American Society for Microbiology, 10.1128/mbio.02205–19. https://journals.asm.org/doi/10.1128/mbio.02205-19 (2025) (Dec. 2019).

45. Si, F., Le Treut, G., Sauls, J. T., Vadia, S., Levin, P. A. & Jun, S. Mechanistic Origin of Cell-Size Control and Homeostasis in Bacteria. *Current Biology* **29,** 1760–1770.e7. ISSN: 0960-9822. https://www.sciencedirect.com/science/article/pii/S0960982219304919 (2025) (June 2019).

46. Meyer, A. J., Segall-Shapiro, T. H., Glassey, E., Zhang, J. & Voigt, C. A. Escherichia coli "Marionette" strains with 12 highly optimized small-molecule sensors. en. *Nature Chemical Biology* **15.** Publisher: Nature Publishing Group, 196–204. ISSN: 1552-4469. https://www.nature.com/articles/s41589-018-0168-3 (2025) (Feb. 2019).

47. Zhang, Q., Azarin, S. M. & Sarkar, C. A. Model-guided engineering of DNA sequences with predictable site-specific recombination rates. en. *Nature Communications* **13.** Publisher: Nature Publishing Group, 4152. ISSN: 2041-1723. https://www.nature.com/articles/s41467-022-31538-3 (2025) (July 2022).

2.4 Supplemental Figures

Parameter	Uncontrolled Consortium	Phase-Varying Consortium
$\overline{\mu_b}$	1.3	1.3
$\overline{K_b}$	1.0	1.0
$\overline{\beta_1}$	0.0	0.2
$\overline{\beta_2}$	0.0	0.1
$\overline{D}$	0.5	0.5
$\overline{S_0}$	9.0	9.0
$\overline{\gamma_b}$	1.0	1.0

Table S1: 2-state phase variation parameter set. $\overline{K_b}$ and $\overline{\gamma_b}$ were set to unity as it is assumed both strains are of the same species and thus, bar growth rates, have similar growth properties. The values of $\overline{\beta_j}$ were selected in accordance with the expected timescales from a previous experimental study by Zhang et al [47]. $\overline{D}$ and $\overline{S_0}$ were selected to be in accordance with the expected functional regime of a chemostat system.

.

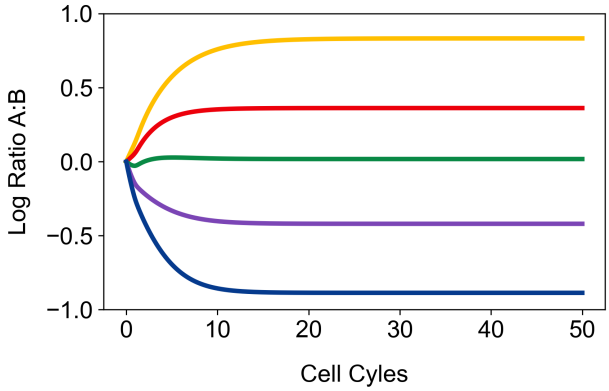

Figure S1: Composition tuning in the 2-state chemostat model. Different color traces correspond to different switching parameter sets (β_j values) in the 2-state chemostat model, leading to different steady state compositions. Parameter sets used for this plot are available in the modeling section of the supplement.

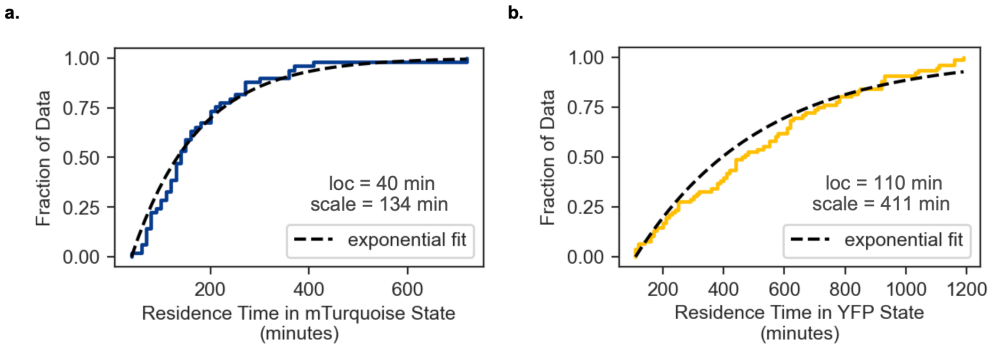

Figure S2: Mother machine residence time cumulative distribution fits. **a**, mTurquoise residence time cumulative distribution fit. **b**, YFP residence cumulative distribution time fit. Collected data was fit to an exponential distribution, allowing both the location and scale parameter to vary.

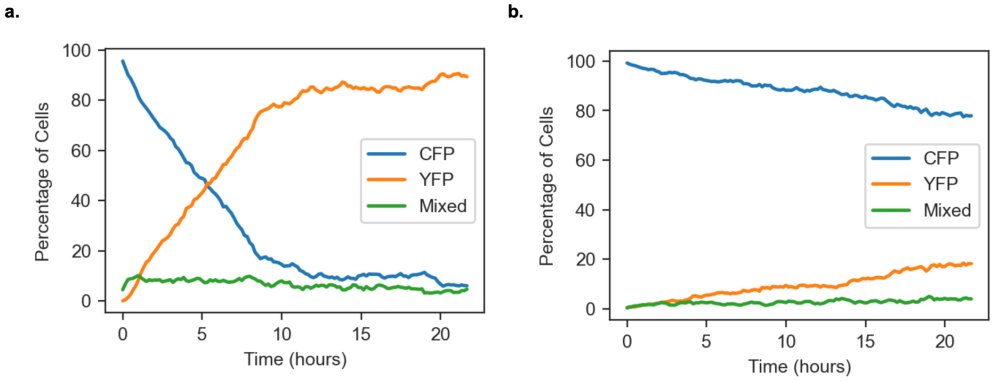

Figure S3: Mother machine individual population dynamics for 2-state system. **a**, YFP-dominant condition. **b**, mTurquoise-dominant condition. Cells are classified into YFP, mTurquoise or mixed bins according to their YFP to mTurquoise ratio. Cells abundance are expressed as percentage of live, fluorescent cells.

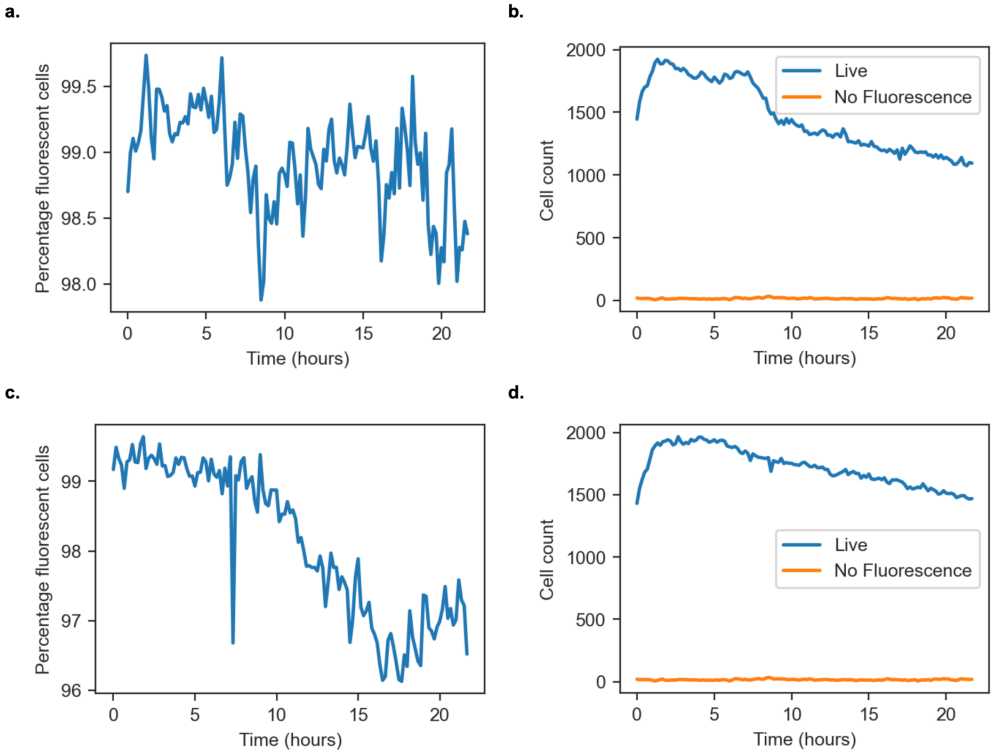

Figure S4: Mother machine cell viability dynamics for 2-state system. **a**, YFP-dominant condition percentage fluorescent cell dynamics. **b**, YFP-dominant condition live and non-fluorescent cell abundance dynamics. **c**, mTurquoise-dominant condition percentage fluorescent cell dynamics. **d**, mTurquoise-dominant condition live and non-fluorescent cell abundance dynamics. Cells are considered non-fluorescent cell when the sum of the normalized flourscent intensity is below 0.25.

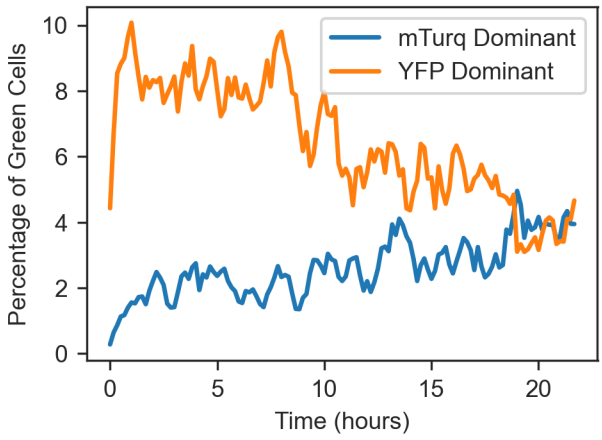

Figure S5: Mother machine mixed cell abundance dynamics. Cells are classified into YFP, mTurquoise, or mixed bins according to their YFP to mTurquoise ratio. Cells abundance are expressed as percentage of live, fluorescent cells.

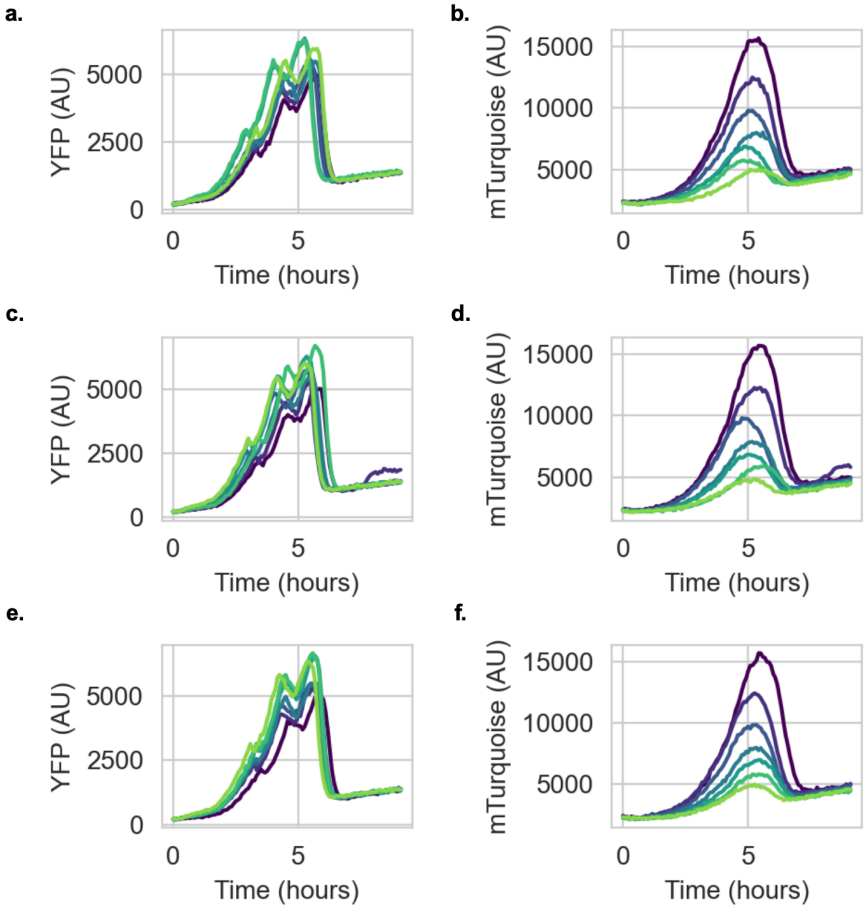

Figure S6: Raw fluorescent traces for 2-strain uncontrolled consortia. **a**, YFP dynamics for replicate 1. **b**, mTurquoise dynamics for replicate 1. **c**, YFP dynamics for replicate 2. **d**, mTurquoise dynamics for replicate 2. **e**, YFP dynamics for replicate 3. **f**, mTurquoise dynamics for replicate 3. Each individual peak corresponds to a growth cycle for a given well. Early cycles are plotted in dark colors, starting in dark blue, and progress to light colors as cycle number increases, finishing in light green.

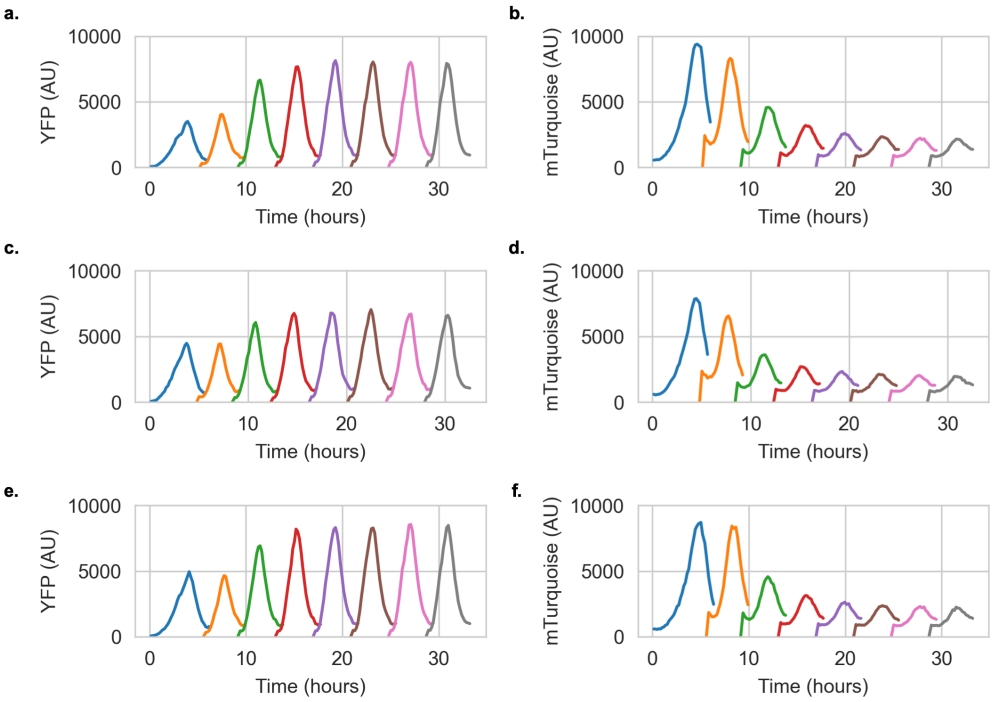

Figure S7: Raw 2-state composition control fluorescent traces for condition A ▬. **a**, YFP dynamics for initial condition 1. **b**, mTurquoise dynamics for initial condition 1. **c**, YFP dynamics for initial condition 2. **d**, mTurquoise dynamics for initial condition 2. **e**, YFP dynamics for initial condition 3. **f**, mTurquoise dynamics for initial condition 3. Each individual peak corresponds to a growth cycle for a given well, max fluorescent signal during this growth signal was taken to be representative of composition for a given fluorescent channel.

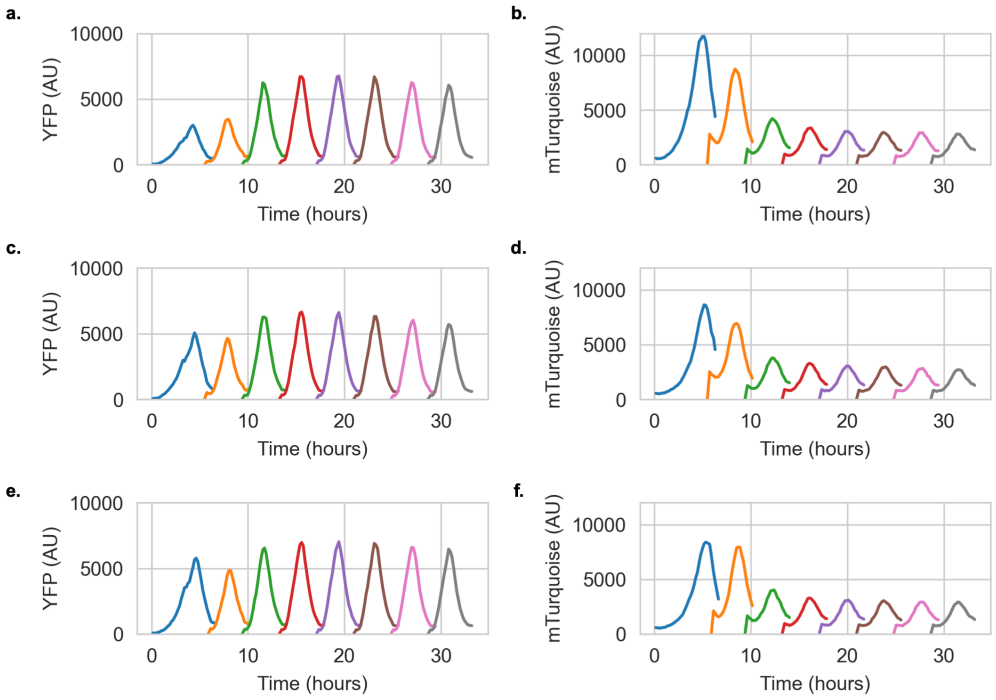

Figure S8: Raw 2-state composition control fluorescent traces for condition B ▬. **a**, YFP dynamics for initial condition 1. **b**, mTurquoise dynamics for initial condition 1. **c**, YFP dynamics for initial condition 2. **d**, mTurquoise dynamics for initial condition 2. **e**, YFP dynamics for initial condition 3. **f**, mTurquoise dynamics for initial condition 3. Each individual peak corresponds to a growth cycle for a given well, max fluorescent signal during this growth signal was taken to be representative of composition for a given fluorescent channel.

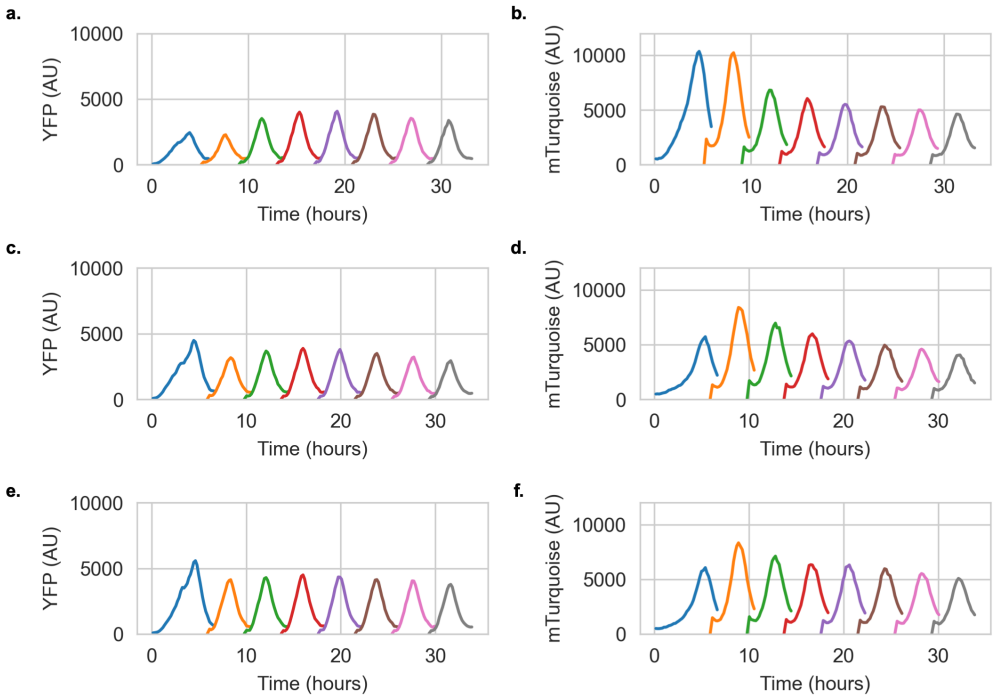

Figure S9: Raw 2-state composition control fluorescent traces for condition C ▬. **a.** YFP dynamics for initial condition 1. **b.** mTurquoise dynamics for initial condition 1. **c.** YFP dynamics for initial condition 2. **d.** mTurquoise dynamics for initial condition 2. **e.** YFP dynamics for initial condition 3. **f.** mTurquoise dynamics for initial condition 3. Each individual peak corresponds to a growth cycle for a given well, max fluorescent signal during this growth signal was taken to be representative of composition for a given fluorescent channel.

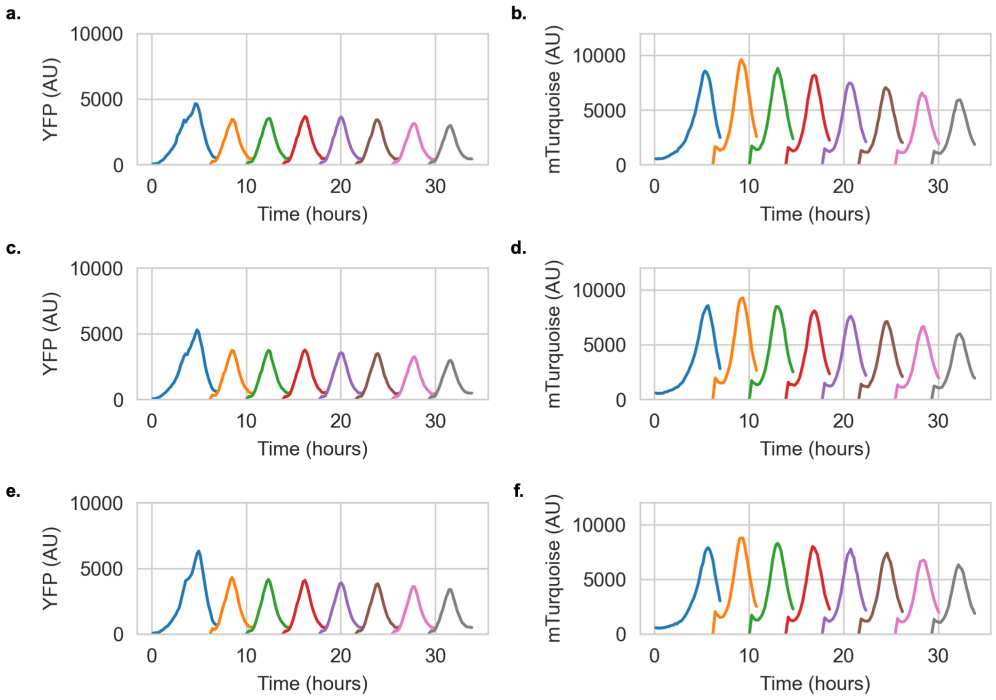

Figure S10: Raw 2-state composition control fluorescent traces for condition D ▬. **a**, YFP dynamics for initial condition 1. **b**, mTurquoise dynamics for initial condition 1. **c**, YFP dynamics for initial condition 2. **d**, mTurquoise dynamics for initial condition 2. **e,** YFP dynamics for initial condition 3. **f**, mTurquoise dynamics for initial condition 3. Each individual peak corresponds to a growth cycle for a given well, max fluorescent signal during this growth signal was taken to be representative of composition for a given fluorescent channel.

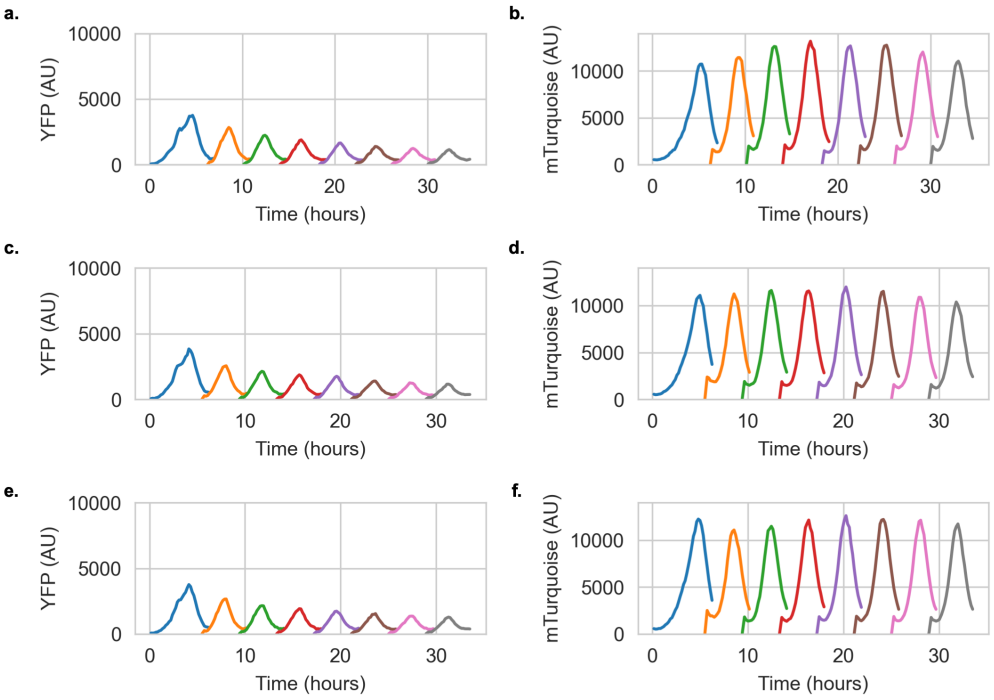

Figure S11: Raw 2-state composition control fluorescent traces for condition E ▬. **a**, YFP dynamics for initial condition 1. **b**, mTurquoise dynamics for initial condition 1. **c**, YFP dynamics for initial condition 2. **d**, mTurquoise dynamics for initial condition 2. **e**, YFP dynamics for initial condition 3. **f**, mTurquoise dynamics for initial condition 3. Each individual peak corresponds to a growth cycle for a given well, max fluorescent signal during this growth signal was taken to be representative of composition for a given fluorescent channel.

Chapter 3

EXTENDING OUR DESIGN TO A 3-STATE PHASE VARIATION SYSTEM

The work described in this chapter currently under review in Nature Communications under the attribution:

Kratz M.F., Elowitz M.B., Murray, R.M. Synthetic Phase Variation for Engineered Microbial Consortia. *bioRxiv* 2025.08.25.672192;
https://doi.org/10.1101/2025.08.25.672192.

3.1 Introduction

With the previous results, we demonstrated the single cell and bulk-scale dynamics of our synthetic phase variation system for two distinct states. Many consortium applications primarily use two strains, but recent use cases in metabolic engineering employed as many as four distinct strains[1]. This work provokes the question of whether synthetic phase variation can scale to larger numbers of states[2, 3].

3.2 Results

Designing and modeling a 3-state phase variation system

Incorporation of a second orthogonal recombinase (blue) can enable 3-state switching. As shown in Figure 3.1a, we added a third transcriptional state downstream of the 2-state unit, and flanked the construct with the attachment sites of the second recombinase. The resulting system is predicted to generate four genetic states, one for state A, one for state B, and two for state C (C_A and C_B). These two C states both express the C gene and are therefore phenotypically equivalent. However, they respond differently to the second (blue) recombinase, with C_A and C_B respectively transitioning to states A and B. In this design, the first recombinase activity (yellow) determines the ratio of A to B population sizes, while the second recombinase (blue) determines the (A+B) to C ratio. We refer to the system as the 3-state circuit based on the number of distinct phenotypic states.

To understand composition control properties of the 3-state circuit, we simulated its dynamics using the framework in Fig. 2 (Fig. 3.1b). We can model the dynamics of the respective genetics states (A, B, C_A and C_B) and substrate (S) as follows:

$$\frac{dC_b}{dt} = \left(\frac{\mu_c S}{K_c + S} - D \right) C_b + \beta_4 B + \beta_2 C_a - C_b(\beta_1 + \beta_3),$$

$$\frac{dC_a}{dt} = \left(\frac{\mu_c S}{K_c + S} - D \right) C_a + \beta_4 A + \beta_1 C_b - C_a(\beta_3 + \beta_2),$$

$$\frac{dA}{dt} = \left(\frac{\mu_a S}{K_a + S} - D \right) A + \beta_1 B + \beta_3 C_a - A(\beta_2 + \beta_4),$$

$$\frac{dB}{dt} = \left(\frac{\mu_b S}{K_b + S} - D \right) B + \beta_3 C_b + \beta_2 A - B(\beta_1 + \beta_4),$$

$$\frac{dS}{dt} = D(S_0 - S) - \left(\frac{\mu_c S}{K_c + S} \frac{C_b}{\gamma_c} + \frac{\mu_c S}{K_c + S} \frac{C_a}{\gamma_c} + \frac{\mu_a S}{K_a + S} \frac{A}{\gamma_a} + \frac{\mu_b S}{K_b + S} \frac{B}{\gamma_b} \right).$$

μ_i,γ_i and K_i are the maximum growth rate, yield constant and half-velocity constant for a given state i, respectively. S_0 and D are the inlet substrate concentration and flow rate, respectively. Finally, β_j is the switching rate associated with a given transition. Note that states C_A and C_B adopt the same protein state/phenotype, and they thus have identical growth parameters in spite of their distinct genetic states. Using non-dimensionalization we can reframe the system of equations and reduce the number of parameters as follows:

$$\frac{d\mathbf{C}_b}{d\boldsymbol{t}} = \left(\frac{\boldsymbol{S}}{1+\boldsymbol{S}} - \overline{D} \right) \mathbf{C}_b + \overline{\beta_4}\mathbf{B} + \overline{\beta_2}\mathbf{C}_a - \mathbf{C}_b \left(\overline{\beta_1} + \overline{\beta_3} \right)$$

$$\frac{d\mathbf{C}_a}{d\boldsymbol{t}} = \left(\frac{\boldsymbol{S}}{1+\boldsymbol{S}} - \overline{D} \right) \mathbf{C}_a + \overline{\beta_4}\mathbf{A} + \overline{\beta_1}\mathbf{C}_b - \mathbf{C}_a \left(\overline{\beta_3} + \overline{\beta_2} \right),$$

$$\frac{d\mathbf{A}}{d\boldsymbol{t}} = \left(\frac{\overline{\mu_a}\overline{K_a}\boldsymbol{S}}{1+\overline{K_a}\boldsymbol{S}} - \overline{D} \right) \mathbf{A} + \overline{\beta_1}\mathbf{B} + \overline{\beta_3}\mathbf{C}_a - \mathbf{A} \left(\overline{\beta_2} + \overline{\beta_4} \right),$$

$$\frac{d\mathbf{B}}{d\boldsymbol{t}} = \left(\frac{\overline{\mu_b}\overline{K_b}\boldsymbol{S}}{1+\overline{K_b}\boldsymbol{S}} - \overline{D} \right) \mathbf{B} + \overline{\beta_3}\mathbf{C}_b + \overline{\beta_2}\mathbf{A} - \mathbf{B} \left(\overline{\beta_1} + \overline{\beta_4} \right),$$

$$\frac{d\boldsymbol{S}}{d\boldsymbol{t}} = \overline{D} \left(\overline{S_0} - \boldsymbol{S} \right) - \left(\frac{\boldsymbol{S}}{1+\boldsymbol{S}} \mathbf{C}_b + \frac{\boldsymbol{S}}{1+\boldsymbol{S}} \mathbf{C}_a + \frac{\overline{\mu_a}\overline{K_a}\boldsymbol{S}}{1+\overline{K_a}\boldsymbol{S}} \frac{\mathbf{A}}{\overline{\gamma_a}} + \frac{\overline{\mu_b}\overline{K_b}\boldsymbol{S}}{1+\overline{K_b}\boldsymbol{S}} \frac{\mathbf{B}}{\overline{\gamma_b}} \right),$$

$$\overline{D} = \frac{D}{\mu_c}, \quad \overline{\beta_j} = \frac{\beta_i}{\mu_c}, \quad \overline{\mu_i} = \frac{\mu_i}{\mu_c}, \quad \overline{K_i} = \frac{K_c}{K_i}, \quad \overline{S_0} = \frac{S_o}{K_c}, \quad \overline{\gamma_i} = \frac{\gamma_i}{\gamma_c}.$$

We can numerically integrate this system of differential equations to investigate the properties of our proposed Timesharing design in a chemostat environment. Further, to simulate the conventional, uncontrolled case, all switching parameters (β_i) can be set to zero.

State-switching in the 3-state architecture stabilizes configurations that would otherwise be unstable (Figure 3.1c, parameters in Table S1). Depending on switching rates, the circuit can access the full repertoire of possible cell state compositions (Figure S1). Overall, these mathematical modeling results imply that our design can be scaled beyond the control of 2-states.

A scaled architecture displays stochastic switching and bulk composition control

To implement the 3-state circuits, we added a second orthogonal recombinase and RDF, TP901[4] together with a third fluorescent protein, mScarlet3[5]. TP901 and its cognate RDF were placed under the control of the lux and cin inducible promoters[6], respectively, and assembled alongside the Bxb1 elements (Figure

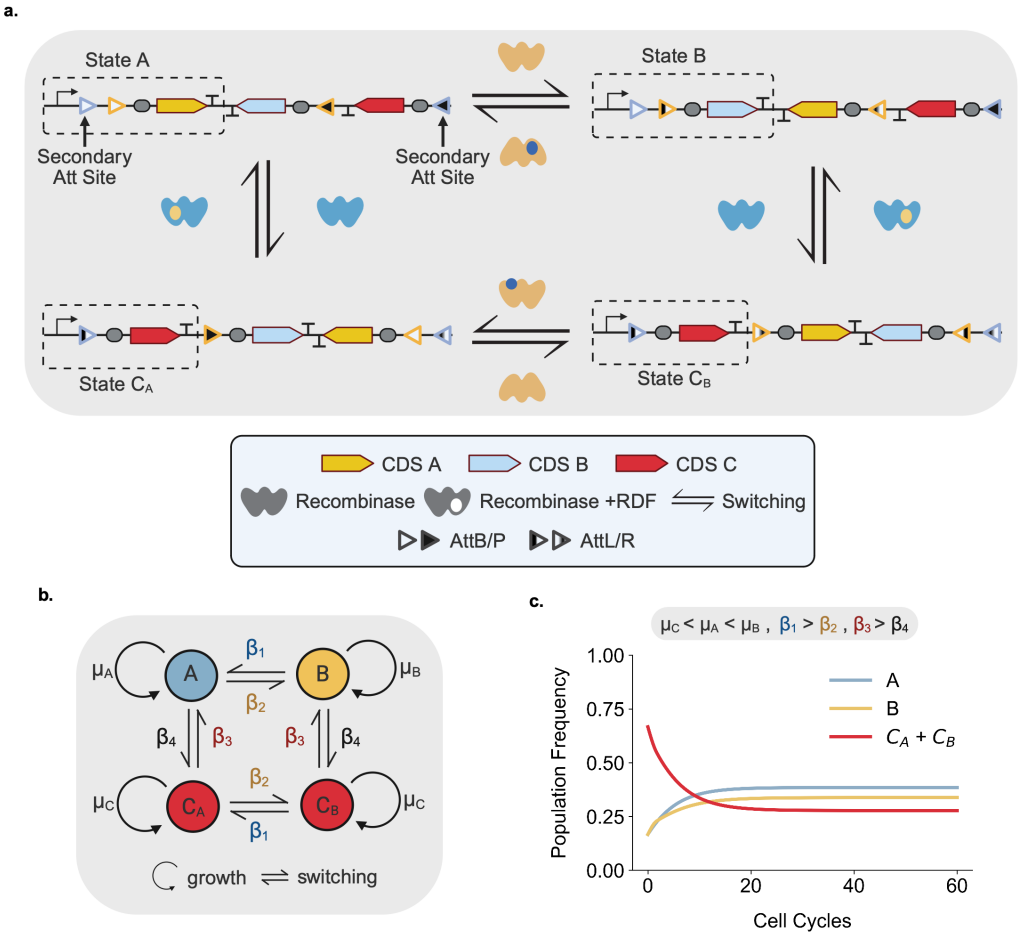

Figure 3.1: **A second recombinase allows 3-state switching**. **a**, Recombinase elements (include Att sites) are colored according to their cognate recombinase. Arrows represent transitions between states, with the relevant recombinase complex catalyzing these transitions next to each arrow. The active transcriptional state of the system is surrounded by a dotted box. Note C_A and C_B are two separate DNA states but transcriptionally are the same state **b**, 3-state phase varying consortium schematic. Note that certain transition rates catalyze multiple distinct transitions e.g. β_1 switches B to A and C_B to C_A **c**, 3-state model simulation dynamics. Presented results and parameters are non-dimensionalized and scaled to the growth rate of strain/phenotype C.

3.2a). We examined the system in the mother machine, using similar growth conditions to the 2-state system (Figure 3.2b, Methods). Cells switched across all three fluorophore states, presenting stable expression of each fluorescent state. However, in contrast to the 2-state system, the 3-state circuit imposed a larger burden on cell physiology, leading to filementation and cell death (Supplemental Movie 2). This was partially remedied by reducing the copy number of the recombinase elements by moving the circuit from a p15a plasmid to a genomic location (pOSIP T-site)[7]. This alteration successfully reduced burden. It also markedly increased the single cell switching timescale, consistent with lower recombinase expression levels (Supplemental Movie 3-7). Nonetheless, the 3-state system exhibited active switching among three stable, heritable expression states.

Finally, we characterized composition control at the bulk level. We initiated cultures from an all-YFP initial composition. We identified several inducer conditions that enabled stable, long-term coexistence ($\sim$120 hours) of all states (Figure 3.2d, Figures S12-S13). This contrasts with a non-switching control system, where the mScarlet strain rapidly takes over the mixed culture (Figure S14). Interestingly, the two switching processes in our system operate at different timescales, with the YFP to mTurquoise (Bxb1) process reaching steady-state noticeably faster than the (YFP + mTurquoise) to mScarlet process. These experiments demonstrated that synthetic phase variation circuits can create a stable set of compositions in an otherwise unstable 3-state system.

Finally, having investigated stable compositions, we asked what transient composition trajectories were accessible. We used a similar passaging setup, but assayed a wider variety of inducer concentrations over fewer passages (Table S2). Under these conditions, increasing salicylate concentration (Bxb1) increased mTurquoise signal and increasing lux AHL (TP901) increased mScarlet signal, indicating that the system continued to function as expected. The 3-state system traversed a broad variety of compositions (Figure 3.2e, Figures S2-S11). Cultures transiently populated compositions heavily biased towards individual states (closer to vertices), as well as mixed compositions (closer to grey center triangle). Depending on the conditions, cells traversed the composition space at different velocities. These experiments demonstrate that we can transiently pass through a wide variety of compositions.

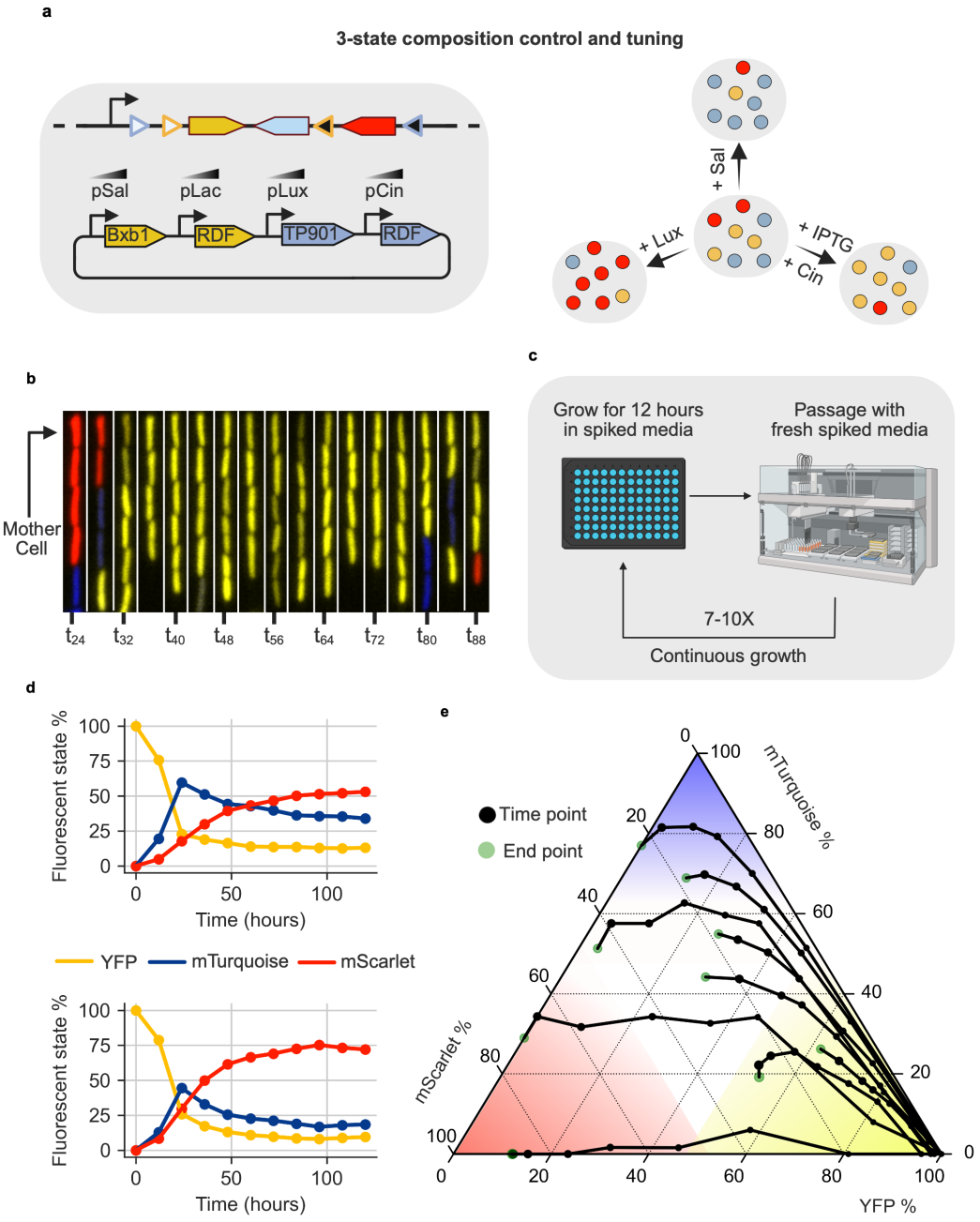

Figure 3.2: **The 3-state design retains the single cell and bulk dynamics of the 2-state system.**

Figure 3.2: **The 3-state design retains the single cell and bulk dynamics of the 2-state system. a**, 3-state composition control schematic. Recombinase elements (include Att sites) are colored according to their cognate recombinase. The 3-state switching construct is integrated as a single copy on the genome. Bxb1 is controlled by a salicylate inducible promoter (pSal) and its cognate RDF is controlled by an IPTG inducible promoter pTac. TP901 is controlled by a Lux AHL (pLux) inducible promoter and its cognate RDF is controlled by a Cin AHL inducible promoter (pCin). By varying inducer levels, the steady state composition of the system should be tunable. The copy number of the recombinase element varies based on the experiment. **b**, Mother machine kymograph. Successive images are separated by forty minute intervals. **c**, Liquid handler passaging setup. **d**, Select stable 3-state time course traces. Fluorescence values have been normalized to the max possible fluorescence signal for the given channel. **e**, 3-state space exploration traces. Fluorescence values have been normalized to the max possible fluorescence signal for the given channel. As typical for a ternary diagram, the ratio of all three channels is used to calculate positions of individual trajectories. Each point in a given trajectory is separated by a fixed growth cycle of 12 hours

3.3 Discussion

The ability to establish defined distributions of cell states within a population would facilitate the creation of stable microbial communities. It has, however, remained unclear if a recombinase approach could tune phenotypic variation for multiple distinct states, and improve upon the tunability and scalability of toggle switches [3, 8, 9] and other previous approaches [10–12]. Here, we demonstrated granular, straightforward control of two to three distinct phenotypic states. Further, this strategy could be scaled to higher numbers of states by adding additional recombinases. Thus, it should be possible to engineer multi-state consortia within a single strain.

There are several limitations of this work. First, recombinases place a burden on cell physiology [13–15]. Better understanding this burden and developing ways to circumvent it will be important for its deployment in applications. Specifically, characterizing the interplay between recombinase expression, switching rates, bulk dynamics and burden will be critical. Optimizing burden is a particular concern as a given composition control method should be as low-burden as possible to minimize interference with consortia function. However, the circuits introduced here displayed high levels of burden in the mother machine, with noticeable cell death and filamentation, especially in the 3-state system (Supplemental Movie 2). These effects were reduced but not eliminated by reducing the copy number of the recombinase genes. In this architecture, the number of unique controllable

states scales linearly with the number of distinct recombinases. There are over 60 characterized serine recombinases[16], many of which are orthogonal, but the larger issue relates to the burden associated with each additional recombinase. This could be partially addressed through mutant recombinase attachment sites that switch at faster rates than their wild-type counterparts[17], reducing the required recombinase expression level, while maintaining higher switching rates. Another fundamental limitation of our approach is shared with the terminal differentiation approach: the cell must be capable of expressing each phenotype in the system. This prevents use of multi-species consortia and runs counter to the typical strain specialization workflows of metabolic engineering[18, 19].

Synthetic phase variation could be expanded in several ways. First, one could decouple the core state switching circuit from the target genes it controls. Specifically, fluorescent protein genes could be replaced with transcriptional activators that would in turn regulate expression of functional transcriptional units on separate genetic constructs. Those transcriptional units would not need to be expressed as single copies. This modification would improve modularity, allowing for easy swapping of functional target genes. Second, a unique element of our circuit is that it could be implemented in mammalian systems, where recombinase activity has previously been demonstrated[58]. Further, unlike communication-mediated composition control, the circuit introduced here does not rely on synthesis or active import and export of metabolites, making it theoretically more host-agnostic than other approaches. It will be interesting to find out whether the circuit can be modified to operate in human cells for research and applications. The approach introduced here could potentially be implemented in non-model microorganisms for rapid development of non-model organism consortia, e.g. *Pseudomonas* species for soil[20] and *Bacteroides* for gut[21].

Synthetic phase variation circuits enable several specific applications. Because cells retain access to all states and control can be maintained without intercellular communication, composition control should be spatially invariant and deployable in non-well-mixed, even static, environments. For instance, bioprocessing has benefited from use of consortia[1, 22–24]. However, at the industrial scale many fermentations have issues with spatial heterogeneity and mixing[25]. This interferes with the use of communication-mediated consortia; our approach would be able to maintain control in this context. Similarly, gut microbiome engineering could be heavily enabled through the use of consortia, with different phenotypes interacting

with specific niches to cause persistent, large scale shifts in the microbiome[26]. However, the gut displays erratic and irregular mixing, favouring the use of our approach to implement consortia in the gut microbiome[27]. Another suitable use of our system may be in the context of biomaterials. Specifically, several biomaterials systems use varying ratios of different strains/phenotypes to generate materials with differing mechanical properties[28, 29]. In our framework, a single cell would be able to generate all phenotypes, implying one could regenerate a biomaterial from a single cell sample. This regeneration phenomena would be infeasible to recreate using the communication-mediated or terminal differentiation approaches.

Stochasticity is often perceived as a nuisance that degrades the performance of synthetic biological circuits. In this case, stochasticity is essential to generate stable, accurate composition at the population level. This design provides an example of how naturally inspired circuits can be used to exploit unique biological phenomena to generate novel engineered functions.

3.4 Materials and Methods

Strain and plasmid construction

The MG1655 Marionette strain was used as the base strain for all experiments in this study. Genomic integrations for this study were performed using the pOSIP clonetegration system. For mother machine experiments, knockouts of the MotA gene were necessary and performed using Lambda Red Recombineering.

All plasmids were assembled using 3G assembly, sourcing parts from Murray Biocircuits Part Library, an extended version of the CIDAR MoClo extension part kit. To perform pOSIP clonetegration of switching constructs, an approach alternating use of bsaI (NEBuilder HiFi DNA Assembly Master Mix) and bsmbI (NEBridge Golden Gate Assembly Kit (BsmBI-v2)) to catalyze golden gate assembly constructs was employed. Other pOSIP clonetegrations were performed using 3G assembly.

Media and Reagents

For plate reader experiments, cells were grown in M9CA 1% glucose (Teknova) with 25 μg/ml chloramphenicol and 50 μg/ml kanamycin. For mother machine experiments were M9CA 0.5% glycerol with 25 μg/ml chloramphenicol, 50 μg/ml kanamycin and 50 μg/ml hygromycin. Unlike the glucose media, the glycerol media was not purchased from a vendor and made in the wetlab. 1L of this media was produced using 200 ml of 5X M9 Salts, 10 ml 50% glycerol solution (Teknova), 10 ml 100X casamino acid solution, 1 ml 1000X thiamine-HCL solution, 200 μl

Solution name	Chemical name and quantity	Solvent name and quantity
5X M9 Salts	56.4 g M9 Salts	1L distilled water
100X Casamino acids	20 g Casamino acids	200 ml distilled water
1000X Thiamine	10 mg Thiamine-HCl	20 ml distilled water
5000X $MgSO_4$	2.465 mg $MgSO_4$-$7H_2O$	10 ml distilled water
10000X $CaCl_2$	1.10 mg $CaCl_2$-$2H_2O$	10 ml distilled water

Table 3.1: **Stock solution table**

5000X MgSO4 solution and 100 μl 10000X CaCl2 solution. The quantities of each chemical and solvent required to make these stock solutions can be found in the table below.

Mother machine experiment preparation

Microfluidic 'mother machine' devices were manufactured in the Jun Lab at UCSD according to the protocol from Wang et al.1 Prior to loading cells, the device was annealed to a WillCo-dish (Glass Bottom Dish, HBST-5040) via high power plasma cleaning. Once annealed, the device was loaded with 10 μl of 0.5 mg/ml BSA (Bovine serum albumin).

From an overnight culture of the relevant strain grown in M9CA Glycerol, 20 μl of culture was diluted into 1 ml of fresh M9CA Glycerol and grown at 37 °C for 4 hours. After 4 hours, the culture was centrifuged and resuspended to concentrate cells 10-fold. 10 μl of this concentrated culture was then loaded into the BSA-treated mother machine device main trench. To load cells into the channels of the mother machine, the device was then placed (via custom adapters) into a centrifuge and spun for two minutes on each side of the device, loading cells into channels on both sides of the main trench. Once cells were loaded, small volumes of spiked media were loaded from the syringe into the mother machine device to clear the main trench of cell debris and provide media for cells.

Mother machine microscopy experiments

The observation setup used a Nikon Ti2e inverted fluorescence microscope with Andor sCMOS Camera, 60X oil-immersion objective and Lumencor Spectra Light

Engine source. The microscope heat-chamber was set to 37°C, the device was fitted on the stage and a microsyringe pump (Harvard Apparatus Pico Plus Elite) fitted with 25 ml syringes (BD Plastipak syringe with Luer-Lok) delivered spiked media to the device at a rate of 0.75 ml/hr. To help avoid temperature related drift from Willco-dish expansion, we waited 1 hour before beginning acquisition.

Images were acquired every 10 minutes for 22 hours, using the Nikon perfect focus system. Power and exposure settings were initially calibrated to balance signal-to-noise ratio and cell viability. After this initial calibration, the same power and exposure settings were used for all experiments. YFP, mTurquoise, and mScarlet were excited using the Blue LED, Cyan/Teal LED, and Green LED, respectively.

Mother machine analysis

To correct temperature related drift during the mother machine experiments, the 'Correct 3D Drift' plugin in FIJI was employed for each FOV. Stabilized FOVs were then cropped and resized to ensure identical pixel dimensions across FOVs. FOVs were then analyzed and segmented in the napari-mm3 software2 developed by the Jun Lab.

The subsequent described steps were performed in python and the scripts applying these steps to the segmented dataset can be found at the following GitHub repository. With the segmented outputs of the napari-mm3 pipeline, the masks were applied to the YFP and mTurquoise fluorescent channels. After background subtraction and normalization to the maximum signal of each fluorophore, intensities for each cell were summed. If below 0.25, the cell was assumed to be non-fluorescent and not included in further analysis. Cells that passed this screening step had the ratio of mTurquoise intensity to YFP intensity calculated. Based on observations of movies, a cell was considered mTurquoise if this ratio was above 2, YFP if this ratio was below 0.5, and mixed if between these two values.

For the mother cell trace in Fig 3.3, on the stabilized movie of the relevant trench, a region of interest was drawn that encapsulated the mother cell. The 'Measure Stack' function was then used to collect intensities in this ROI. The max values of each channel across time were then smoothed using the Savitzky-Golay filter implementation in Scipy.

Composition control plate reader experiments (2-state)

Unless otherwise specified, all cultures were grown in 96 square well plates (96 well MatriPlate™ clear bottom), in M9CA Glucose, at 37°C using a plate reader (Biotek H1M). From an overnight culture of the 2-state system, three separate wells with different spiked media were seeded and grown overnight. These three wells were then spun down to remove inducers and resuspended in fresh media. 65 μl of these resuspended cultures were then added to 299 μl of fresh unspiked media and grown in a plate reader until they reached an OD700 of 0.65. At this OD, the liquid handler (Hamilton STARlet Liquid Handling Robot) removed the culture plate and seeded a new culture for each of the three wells. These new cultures were composed of 299 μl spiked media and 64 μl of the previous culture. The culture plate was then replaced into the plate reader, repeating this culture seeding process once the newest culture reached an OD700 of 0.65.

Due to the time-varying, pulsatile production of the deg-tagged fluorophores in batch culture, the max YFP and mTurquoise fluorescent signal pulse in a given growth well was taken as the abundance of a given state. After background subtraction, these values were used to calculate the ratio of YFP to mTurquoise signal. The code implementation of this workflow can be found in the GitHub repository associated with this publication.

Composition control plate reader experiments (3-state)

Due to multiplexing constraints with the liquid handler machine, the passages in the following experiments were performed manually. As such, this protocol differs from the 2-state protocol so as to be more 'human-friendly'. From an overnight culture of the 3-state system, a single well with spiked media was seeded and grown in the plate reader at 37°C. After 12 hours, the plate was removed and 2 μl of cells from the grown well was transferred to a new well with 200 μl fresh spiked media, maintaining the same concentrations of spiked inducers in these new wells. This lower dilution ratio was selected as it seemed to cause a marked improvement in cell health and circuit function. This dilution was repeated a further 6-9 times for a total of 7-10X12 hr growth cycles.

Due to the time-varying production of the deg-tagged fluorophores in batch culture, the max YFP, mScarlet, and mTurquoise fluorescent signal in a given growth well was taken as the abundance of a given state. Due to drastically differing max intensities of each state, after background subtraction, the max signal was normalized to the

maximum possible intensity of the state. These max intensities were determined by completely biasing the system to the relevant fluorescent state. These subtracted and normalized values were then used to plot the ternary diagram in Figure 6.

Data processing and analysis All described computational workflows starting from the raw datasets to the generated figures (main and supplement) can be found in the GitHub repository associated with this chapter.

BIBLIOGRAPHY

1. Jones, J. A., Vernacchio, V. R., Collins, S. M., Shirke, A. N., Xiu, Y., Englaender, J. A., Cress, B. F., McCutcheon, C. C., Linhardt, R. J., Gross, R. A. & Koffas, M. A. G. Complete Biosynthesis of Anthocyanins Using E. coli Polycultures. *mBio* **8.** Publisher: American Society for Microbiology, e00621–17. https://journals.asm.org/doi/10.1128/mBio.00621-17 (2021).

2. Zhu, R., del Rio-Salgado, J. M., Garcia-Ojalvo, J. & Elowitz, M. B. Synthetic multistability in mammalian cells. *Science* **375.** Publisher: American Association for the Advancement of Science, eabg9765. https://www.science.org/doi/10.1126/science.abg9765 (2025) (Jan. 2022).

3. Wu, F., Su, R.-Q., Lai, Y.-C. & Wang, X. Engineering of a synthetic quadrastable gene network to approach Waddington landscape and cell fate determination. *eLife* **6** (ed Shou, W.) Publisher: eLife Sciences Publications, Ltd, e23702. ISSN: 2050-084X. https://doi.org/10.7554/eLife.23702 (2025) (Apr. 2017).

4. Christiansen, B., Brøndsted, L., Vogensen, F. K. & Hammer, K. A resolvase-like protein is required for the site-specific integration of the temperate lactococcal bacteriophage TP901-1. *Journal of Bacteriology* **178.** Publisher: American Society for Microbiology, 5164–5173. https://journals.asm.org/doi/10.1128/jb.178.17.5164-5173.1996 (2025) (Sept. 1996).

5. Gadella, T. W. J., van Weeren, L., Stouthamer, J., Hink, M. A., Wolters, A. H. G., Giepmans, B. N. G., Aumonier, S., Dupuy, J. & Royant, A. mScarlet3: a brilliant and fast-maturing red fluorescent protein. en. *Nature Methods* **20.** Publisher: Nature Publishing Group, 541–545. ISSN: 1548-7105. https://www.nature.com/articles/s41592-023-01809-y (2025) (Apr. 2023).

6. Meyer, A. J., Segall-Shapiro, T. H., Glassey, E., Zhang, J. & Voigt, C. A. Escherichia coli "Marionette" strains with 12 highly optimized small-molecule sensors. en. *Nature Chemical Biology* **15.** Publisher: Nature Publishing Group, 196–204. ISSN: 1552-4469. https://www.nature.com/articles/s41589-018-0168-3 (2025) (Feb. 2019).

7. St-Pierre, F., Cui, L., Priest, D. G., Endy, D., Dodd, I. B. & Shearwin, K. E. One-Step Cloning and Chromosomal Integration of DNA. *ACS Synthetic Biology* **2.** Publisher: American Chemical Society, 537–541. https://doi.org/10.1021/sb400021j (2022) (Sept. 2013).

8. Guarino, A., Fiore, D., Salzano, D. & di Bernardo, M. Balancing Cell Populations Endowed with a Synthetic Toggle Switch via Adaptive Pulsatile Feedback Control. *ACS Synthetic Biology* **9.** Publisher: American Chemical Society, 793–803. https://doi.org/10.1021/acssynbio.9b00464 (2025) (Apr. 2020).

9. Salzano, D., Fiore, D. & di Bernardo, M. Ratiometric control of cell phenotypes in monostrain microbial consortia. *Journal of The Royal Society Interface* **19.** Publisher: Royal Society, 20220335. https://royalsocietypublishing.org/doi/full/10.1098/rsif.2022.0335 (2025) (July 2022).

10. You, L., Cox, R. S., Weiss, R. & Arnold, F. H. Programmed population control by cell–cell communication and regulated killing. en. *Nature* **428.** Publisher: Nature Publishing Group, 868–871. ISSN: 1476-4687. https://www.nature.com/articles/nature02491 (2025) (Apr. 2004).

11. Aditya, C., Bertaux, F., Batt, G. & Ruess, J. A light tunable differentiation system for the creation and control of consortia in yeast. en. *Nature Communications* **12.** Publisher: Nature Publishing Group, 5829. ISSN: 2041-1723. https://www.nature.com/articles/s41467-021-26129-7 (2025) (Oct. 2021).

12. An, B., Tang, T.-C., Zhang, Q., Wang, T., Gan, K., Liu, K., Liu, Y., Wang, Y., Shaw, W. M., Liang, Q., Wang, Y., Lu, T. K., Church, G. M. & Zhong, C. *Synthetic ratio computation for programming population composition and multicellular morphology* en. Pages: 2024.11.26.624747 Section: New Results. Dec. 2024. https://www.biorxiv.org/content/10.1101/2024.11.26.624747v2 (2025).

13. Grob, A., Di Blasi, R. & Ceroni, F. Experimental tools to reduce the burden of bacterial synthetic biology. *Current Opinion in Systems Biology* **28,** 100393. ISSN: 2452-3100. https://www.sciencedirect.com/science/article/pii/S2452310021000883 (2025) (Dec. 2021).

14. Sechkar, K., Steel, H., Perrino, G. & Stan, G.-B. A coarse-grained bacterial cell model for resource-aware analysis and design of synthetic gene circuits. en. *Nature Communications* **15.** Publisher: Nature Publishing Group, 1981. ISSN: 2041-1723. https://www.nature.com/articles/s41467-024-46410-9 (2025) (Mar. 2024).

15. Liu, Q., Schumacher, J., Wan, X., Lou, C. & Wang, B. Orthogonality and Burdens of Heterologous AND Gate Gene Circuits in E. coli. *ACS Synthetic Biology* **7.** Publisher: American Chemical Society, 553–564. https://doi.org/10.1021/acssynbio.7b00328 (2025) (Feb. 2018).

16. Durrant, M. G., Fanton, A., Tycko, J., Hinks, M., Chandrasekaran, S. S., Perry, N. T., Schaepe, J., Du, P. P., Lotfy, P., Bassik, M. C., Bintu, L., Bhatt, A. S. & Hsu, P. D. Systematic discovery of recombinases for efficient integration of large DNA sequences into the human genome. en. *Nature Biotechnology* **41.** Publisher: Nature Publishing Group, 488–499. ISSN: 1546-1696. https://www.nature.com/articles/s41587-022-01494-w (2025) (Apr. 2023).

17. Zhang, Q., Azarin, S. M. & Sarkar, C. A. Model-guided engineering of DNA sequences with predictable site-specific recombination rates. en. *Nature Communications* **13.** Publisher: Nature Publishing Group, 4152. ISSN: 2041-1723. https://www.nature.com/articles/s41467-022-31538-3 (2025) (July 2022).

18. Xin, Y. & Qiao, M. Towards microbial consortia in fermented foods for metabolic engineering and synthetic biology. *Food Research International* **201,** 115677. ISSN: 0963-9969. https://www.sciencedirect.com/science/article/pii/S0963996925000134 (2025) (Feb. 2025).

19. Sun, J. & Alper, H. S. Metabolic engineering of strains: from industrial-scale to lab-scale chemical production. *Journal of Industrial Microbiology and Biotechnology* **42,** 423–436. ISSN: 1367-5435. https://doi.org/10.1007/s10295-014-1539-8 (2025) (Mar. 2015).

20. Larsson, E. M., Murray, R. M. & Newman, D. K. Engineering the Soil Bacterium Pseudomonas synxantha 2–79 into a Ratiometric Bioreporter for Phosphorus Limitation. *ACS Synthetic Biology* **13.** Publisher: American Chemical Society, 384–393. https://doi.org/10.1021/acssynbio.3c00642 (2025) (Jan. 2024).

21. Mimee, M., Tucker, A. C., Voigt, C. A. & Lu, T. K. Programming a Human Commensal Bacterium, Bacteroides thetaiotaomicron, to Sense and Respond to Stimuli in the Murine Gut Microbiota. English. *Cell Systems* **1.** Publisher: Elsevier, 62–71. ISSN: 2405-4712, 2405-4720. https://www.cell.com/cell-systems/abstract/S2405-4712(15)00006-X (2025) (July 2015).

22. Wang, F., Zhao, J., Li, Q., Yang, J., Li, R., Min, J., Yu, X., Zheng, G.-W., Yu, H.-L., Zhai, C., Acevedo-Rocha, C. G., Ma, L. & Li, A. One-pot biocatalytic route from cycloalkanes to alpha,omega-dicarboxylic acids by designed Escherichia coli consortia. en. *Nature Communications* **11.** Bandiera_abtest: a Cc_license_type: cc_by Cg_type: Nature Research Journals Number: 1 Primary_atype: Research Publisher: Nature Publishing Group Subject_term: Biocatalysis;Biosynthesis;Enzymes Subject_term_id: biocatalysis;biosynthesis;enzymes, 5035. ISSN: 2041-1723. https://www.nature.com/articles/s41467-020-18833-7 (2021) (Oct. 2020).

23. Wang, X., Su, R., Chen, K., Xu, S., Feng, J. & Ouyang, P. Engineering a Microbial Consortium Based Whole-Cell System for Efficient Production of Glutarate From L-Lysine. *Frontiers in Microbiology* **10,** 341. ISSN: 1664-302X. https://www.frontiersin.org/article/10.3389/fmicb.2019.00341 (2021) (2019).

24. Zhang, Z., Li, Q., Wang, F., Li, R., Yu, X., Kang, L., Zhao, J. & Li, A. One-pot biosynthesis of 1,6-hexanediol from cyclohexane by de novo designed cascade biocatalysis. en. *Green Chemistry* **22.** Publisher: Royal Society of Chemistry, 7476–7483. https://pubs.rsc.org/en/content/articlelanding/2020/gc/d0gc02600j (2021) (2020).

25. Lara, A. R., Galindo, E., Ramírez, O. T. & Palomares, L. A. Living with heterogeneities in bioreactors: understanding the effects of environmental gradients on cells. eng. *Molecular Biotechnology* **34,** 355–381. ISSN: 1073-6085 (Nov. 2006).

26. Nazir, A., Hussain, F. H. N. & Raza, A. Advancing microbiota therapeutics: the role of synthetic biology in engineering microbial communities for precision medicine. *Frontiers in Bioengineering and Biotechnology* **12,** 1511149. ISSN: 2296-4185. https://www.ncbi.nlm.nih.gov/pmc/articles/PMC11652149/ (2025) (Dec. 2024).

27. Labavić, D., Loverdo, C. & Bitbol, A.-F. Hydrodynamic flow and concentration gradients in the gut enhance neutral bacterial diversity. *Proceedings of the National Academy of Sciences* **119.** Publisher: Proceedings of the National Academy of Sciences, e2108671119. https://www.pnas.org/doi/10.1073/pnas.2108671119 (2025) (Jan. 2022).

28. An, B., Wang, Y., Jiang, X., Ma, C., Mimee, M., Moser, F., Li, K., Wang, X., Tang, T.-C., Huang, Y., Liu, Y., Lu, T. K. & Zhong, C. Programming Living Glue Systems to Perform Autonomous Mechanical Repairs. English. *Matter* **3.** Publisher: Elsevier, 2080–2092. ISSN: 2590-2393, 2590-2385. https://www.cell.com/matter/abstract/S2590-2385(20)30504-X (2025) (Dec. 2020).

29. Gilbert, C. & Ellis, T. Biological Engineered Living Materials: Growing Functional Materials with Genetically Programmable Properties. *ACS Synthetic Biology* **8.** Publisher: American Chemical Society, 1–15. https://doi.org/10.1021/acssynbio.8b00423 (2025) (Jan. 2019).

3.5 Supplemental Figures

Parameter	Phase-Varying Consortium
$\overline{\mu_a}$	1.1
$\overline{\mu_b}$	1.3
$\overline{K_a}$	1.0
$\overline{K_b}$	1.0
$\overline{\beta_1}$	0.145
$\overline{\beta_2}$	0.090
$\overline{\beta_3}$	0.1
$\overline{\beta_4}$	0.062
$\overline{D}$	0.5
$\overline{S_0}$	10.0
$\overline{\gamma_a}$	1.0
$\overline{\gamma_b}$	1.0

Table S1: 3-state phase variation parameter set. Simulations were performed for 60 divisions. $\overline{K_i}$ and $\overline{\gamma_i}$ were set to unity as it assumed both strains are of the same species and thus, bar growth rates, have similar growth properties. The values of $\overline{\beta_j}$ were selected in accordance with the expected timescales from a previous experimental study by Zhang et al [17]. $\overline{D}$ and $\overline{S_0}$ were selected to be in accordance with the expected functional regime of a chemostat system.

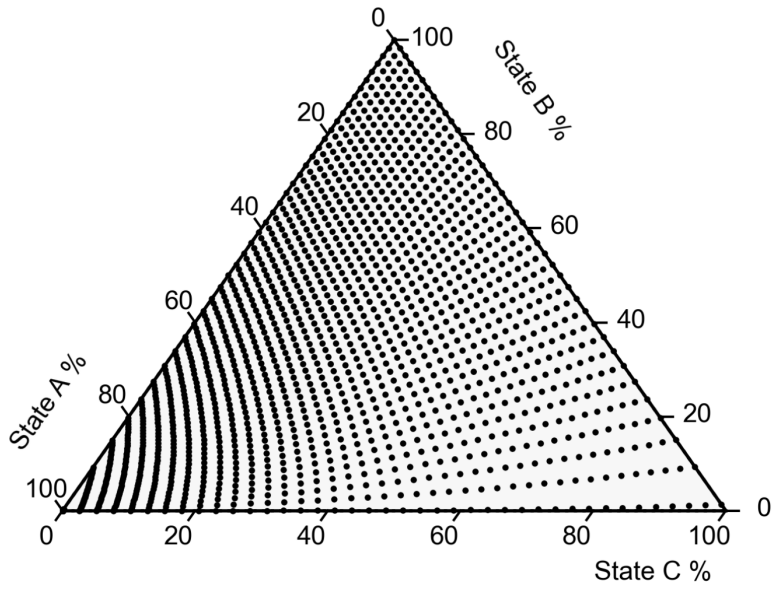

Figure S1: Parameter sweeps of the 3-state model shows our approach can occupy any position in composition space. Ternary diagram of the 3-state system, each dot corresponds to the steady-state composition for a given set of switching rates (four distinct β_j values). The parameter ranges used for this plot are available in the modeling section of the supplement.

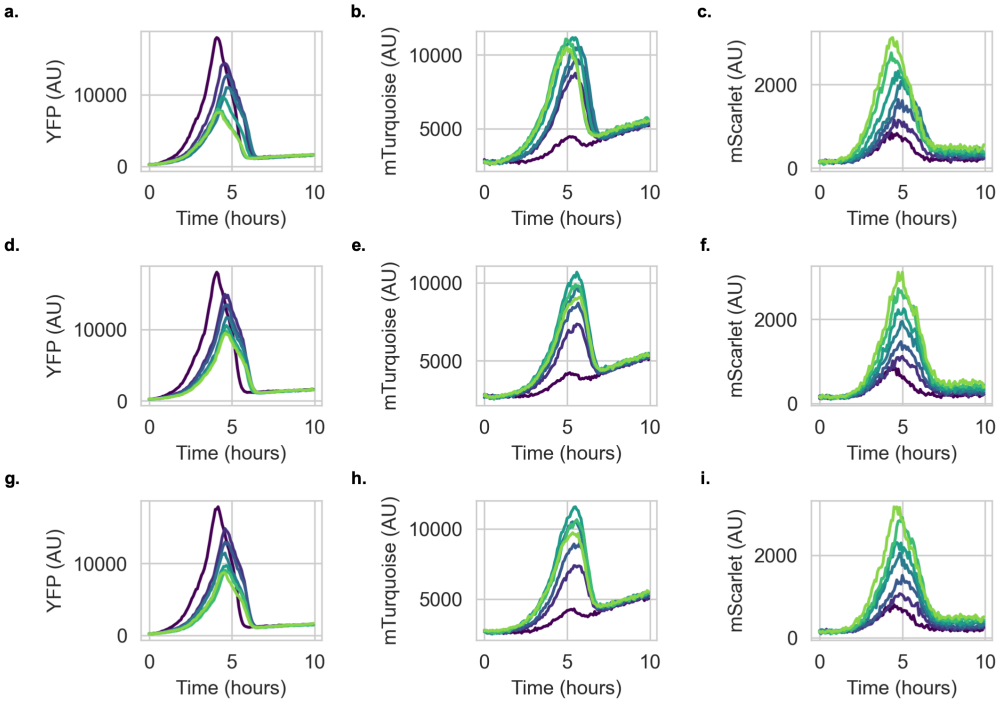

Figure S2: Raw 3-state composition control fluorescent traces for condition A. **a**, YFP dynamics for replicate 1. **b**, mTurquoise dynamics for replicate 1. **c**, mScarlet dynamics for replicate 1. **d**, YFP dynamics for replicate 2. **e**, mTurquoise dynamics for replicate 2. **f**, mScarlet dynamics for replicate 2. **g**, YFP dynamics for replicate 3. **h**, mTurquoise dynamics for replicate 3. **i**, mScarlet dynamics for replicate 3. Each individual peak corresponds to a growth cycle for a given well. Early cycles are plotted in dark colors, starting in dark blue, and progress to light colors as cycle number increases, finishing in light green. Max fluorescent signal during this growth signal was taken to be representative of composition for a given fluorescent channel.

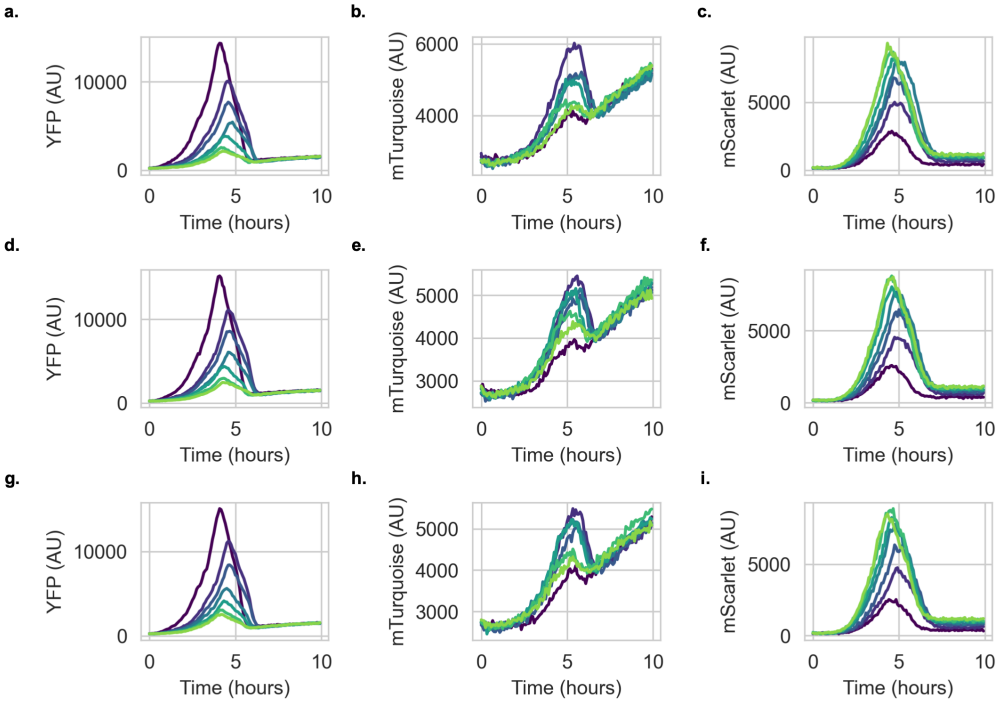

Figure S3: Raw 3-state composition control fluorescent traces for condition B. **a**, YFP dynamics for replicate 1. **b**, mTurquoise dynamics for replicate 1. **c**, mScarlet dynamics for replicate 1. **d**, YFP dynamics for replicate 2. **e**, mTurquoise dynamics for replicate 2. **f**, mScarlet dynamics for replicate 2. **g**, YFP dynamics for replicate 3. **h**, mTurquoise dynamics for replicate 3. **i**, mScarlet dynamics for replicate 3. Each individual peak corresponds to a growth cycle for a given well. Early cycles are plotted in dark colors, starting in dark blue, and progress to light colors as cycle number increases, finishing in light green. Max fluorescent signal during this growth signal was taken to be representative of composition for a given fluorescent channel.

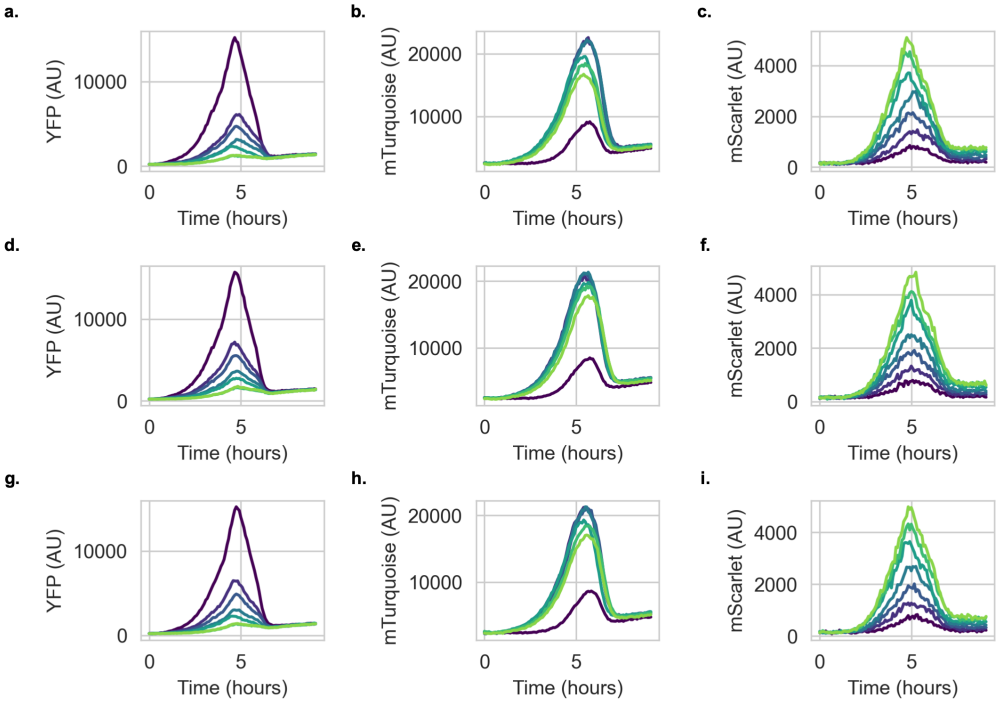

Figure S4: Raw 3-state composition control fluorescent traces for condition C. **a.** YFP dynamics for replicate 1. **b.** mTurquoise dynamics for replicate 1. **c.** mScarlet dynamics for replicate 1. **d.** YFP dynamics for replicate 2. **e.** mTurquoise dynamics for replicate 2. **f.** mScarlet dynamics for replicate 2. **g.** YFP dynamics for replicate 3. **h.** mTurquoise dynamics for replicate 3. **i.** mScarlet dynamics for replicate 3. Each individual peak corresponds to a growth cycle for a given well. Early cycles are plotted in dark colors, starting in dark blue and progress to light colors as cycle number increases, finishing in light green. Max fluorescent signal during this growth signal was taken to be representative of composition for a given fluorescent channel.

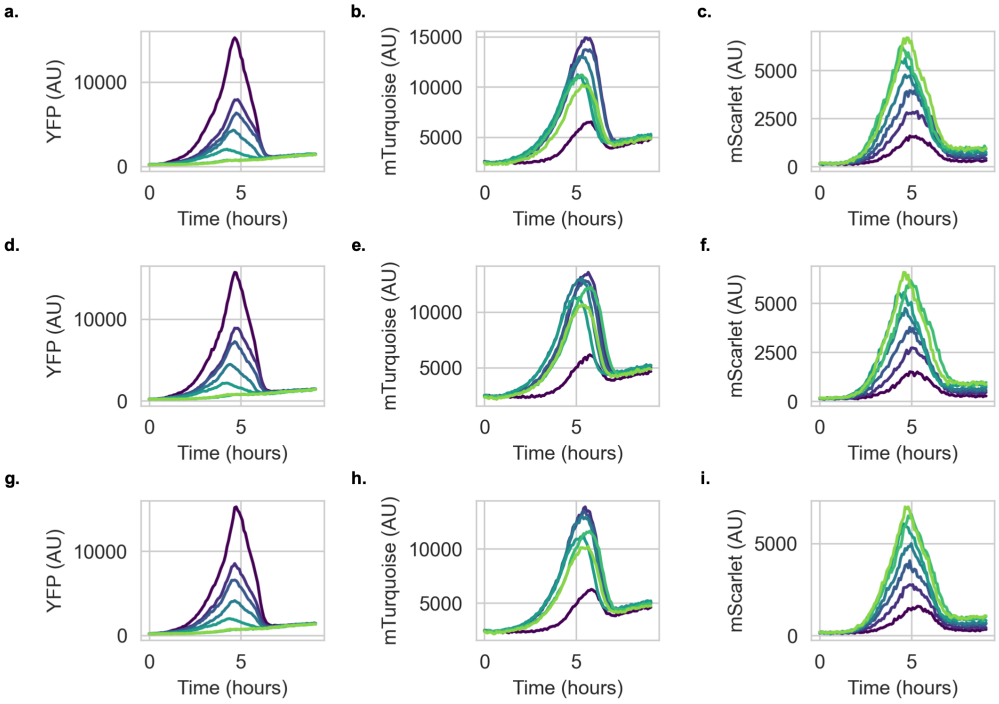

Figure S5: Raw 3-state composition control fluorescent traces for condition D. **a**, YFP dynamics for replicate 1. **b**, mTurquoise dynamics for replicate 1. **c**, mScarlet dynamics for replicate 1. **d**, YFP dynamics for replicate 2. **e**, mTurquoise dynamics for replicate 2. **f**, mScarlet dynamics for replicate 2. **g**, YFP dynamics for replicate 3. **h**, mTurquoise dynamics for replicate 3. **i**, mScarlet dynamics for replicate 3. Each individual peak corresponds to a growth cycle for a given well. Early cycles are plotted in dark colors, starting in dark blue, and progress to light colors as cycle number increases, finishing in light green. Max fluorescent signal during this growth signal was taken to be representative of composition for a given fluorescent channel.

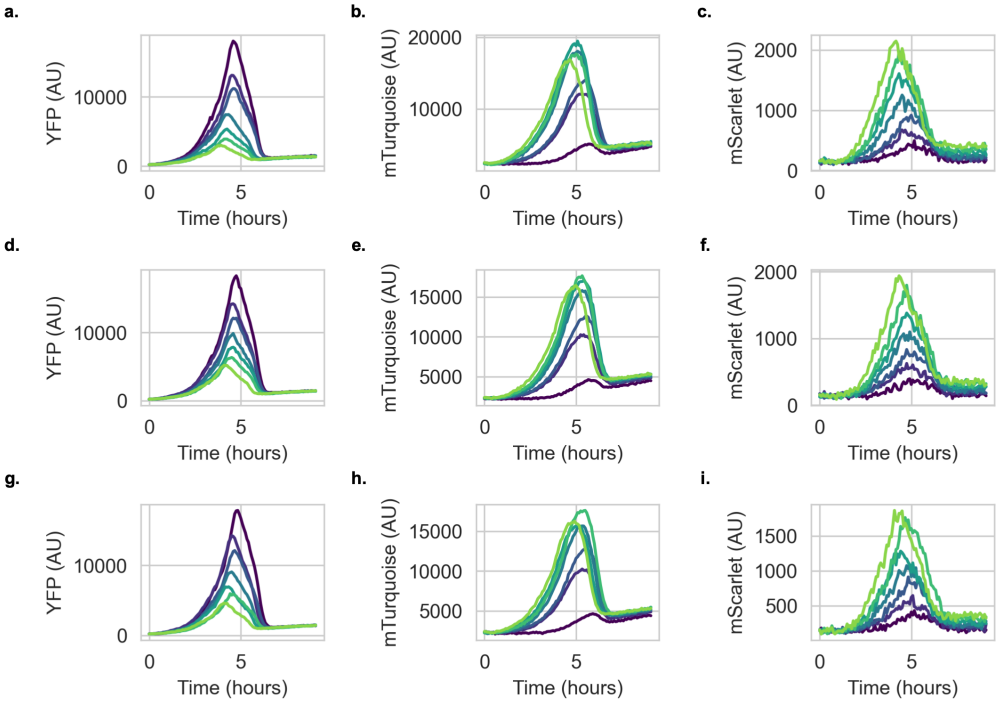

Figure S6: Raw 3-state composition control fluorescent traces for condition E. **a**, YFP dynamics for replicate 1. **b**, mTurquoise dynamics for replicate 1. **c**, mScarlet dynamics for replicate 1. **d**, YFP dynamics for replicate 2. **e.** mTurquoise dynamics for replicate 2. **f**, mScarlet dynamics for replicate 2. **g**, YFP dynamics for replicate 3. **h**, mTurquoise dynamics for replicate 3. **i**, mScarlet dynamics for replicate 3. Each individual peak corresponds to a growth cycle for a given well. Early cycles are plotted in dark colors, starting in dark blue, and progress to light colors as cycle number increases, finishing in light green. Max fluorescent signal during this growth signal was taken to be representative of composition for a given fluorescent channel.

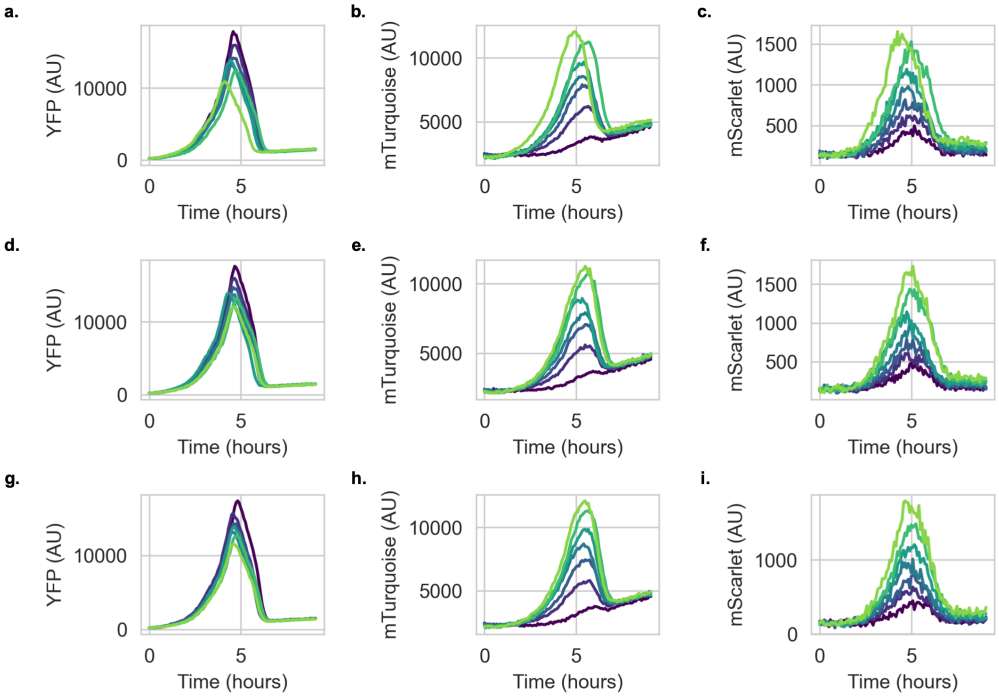

Figure S7: Raw 3-state composition control fluorescent traces for condition F. **a**, YFP dynamics for replicate 1. **b**, mTurquoise dynamics for replicate 1. **c**, mScarlet dynamics for replicate 1. **d**, YFP dynamics for replicate 2. **e**, mTurquoise dynamics for replicate 2. **f**, mScarlet dynamics for replicate 2. **g**, YFP dynamics for replicate 3. **h**, mTurquoise dynamics for replicate 3. **i**, mScarlet dynamics for replicate 3. Each individual peak corresponds to a growth cycle for a given well. Early cycles are plotted in dark colors, starting in dark blue and progress to light colors as cycle number increases, finishing in light green. Max fluorescent signal during this growth signal was taken to be representative of composition for a given fluorescent channel.

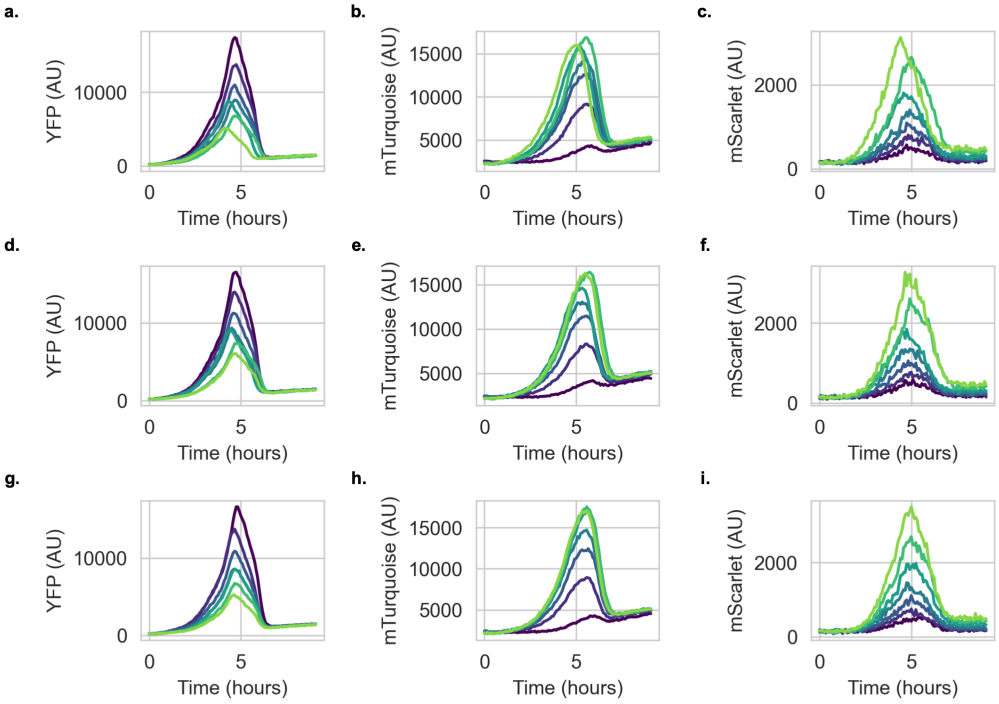

Figure S8: Raw 3-state composition control fluorescent traces for condition G. **a**, YFP dynamics for replicate 1. **b**, mTurquoise dynamics for replicate 1. **c**, mScarlet dynamics for replicate 1. **d**, YFP dynamics for replicate 2. **e**, mTurquoise dynamics for replicate 2. **f**, mScarlet dynamics for replicate 2. **g**, YFP dynamics for replicate 3. **h**, mTurquoise dynamics for replicate 3. **i**, mScarlet dynamics for replicate 3. Each individual peak corresponds to a growth cycle for a given well. Early cycles are plotted in dark colors, starting in dark blue, and progress to light colors as cycle number increases, finishing in light green. Max fluorescent signal during this growth signal was taken to be representative of composition for a given fluorescent channel.

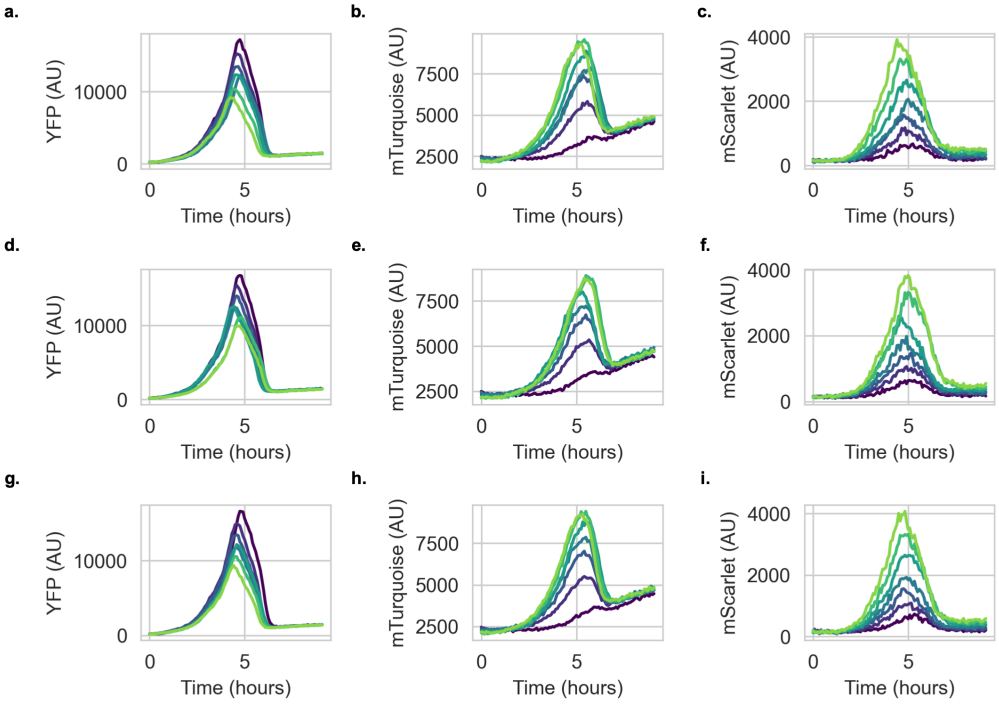

Figure S9: Raw 3-state composition control fluorescent traces for condition H. **a**, YFP dynamics for replicate 1. **b**, mTurquoise dynamics for replicate 1. **c**, mScarlet dynamics for replicate 1. **d**, YFP dynamics for replicate 2. **e**, mTurquoise dynamics for replicate 2. **f**, mScarlet dynamics for replicate 2. **g**, YFP dynamics for replicate 3. **h**, mTurquoise dynamics for replicate 3. **i**, mScarlet dynamics for replicate 3. Each individual peak corresponds to a growth cycle for a given well. Early cycles are plotted in dark colors, starting in dark blue, and progress to light colors as cycle number increases, finishing in light green. Max fluorescent signal during this growth signal was taken to be representative of composition for a given fluorescent channel.

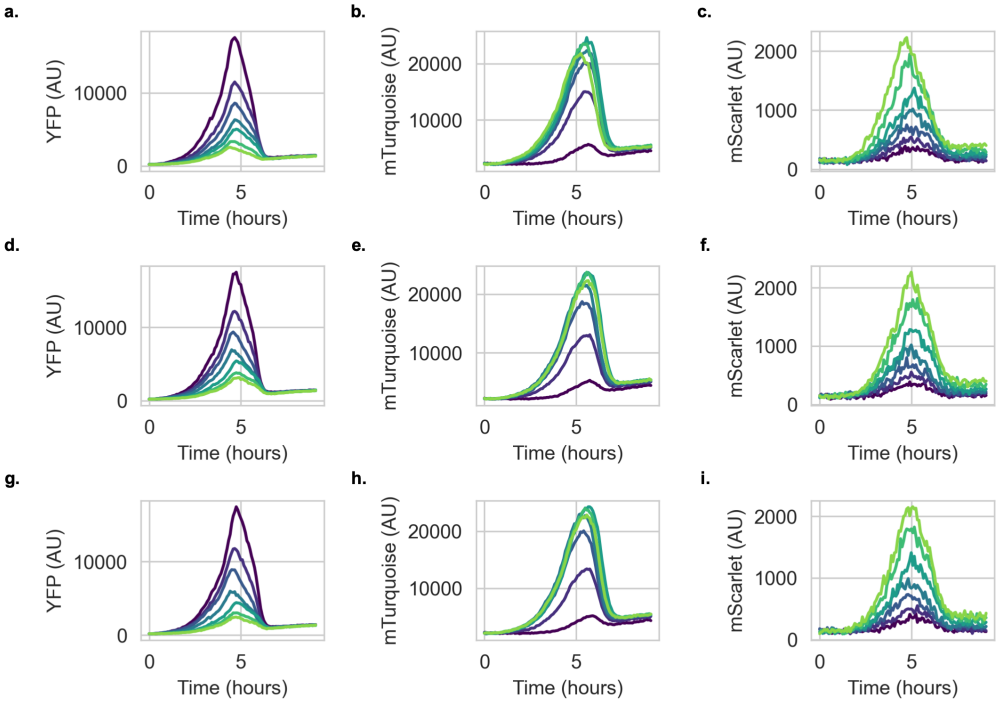

Figure S10: Raw 3-state composition control fluorescent traces for condition I. **a.** YFP dynamics for replicate 1. **b.** mTurquoise dynamics for replicate 1. **c.** mScarlet dynamics for replicate 1. **d.** YFP dynamics for replicate 2. **e.** mTurquoise dynamics for replicate 2. **f.** mScarlet dynamics for replicate 2. **g.** YFP dynamics for replicate 3. **h.** mTurquoise dynamics for replicate 3. **i.** mScarlet dynamics for replicate 3. Each individual peak corresponds to a growth cycle for a given well. Early cycles are plotted in dark colors, starting in dark blue, and progress to light colors as cycle number increases, finishing in light green. Max fluorescent signal during this growth signal was taken to be representative of composition for a given fluorescent channel.

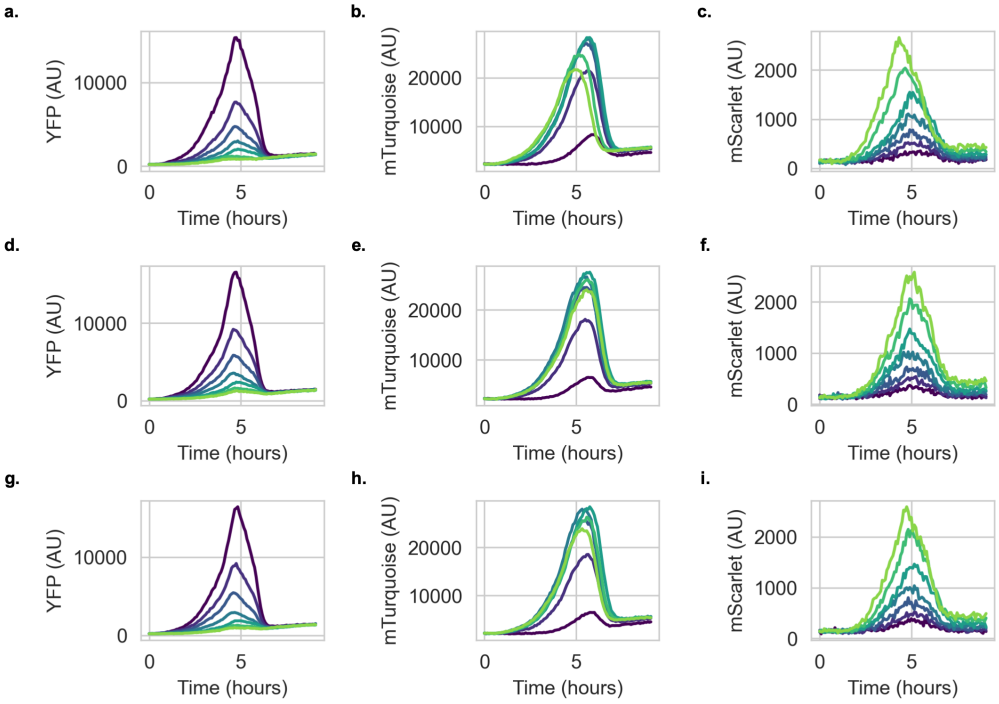

Figure S11: Raw 3-state composition control fluorescent traces for condition J. **a**, YFP dynamics for replicate 1. **b,** mTurquoise dynamics for replicate 1. **c**, mScarlet dynamics for replicate 1. **d**, YFP dynamics for replicate 2. **e**,mTurquoise dynamics for replicate 2. **f**, mScarlet dynamics for replicate 2. **g**, YFP dynamics for replicate 3. **h**, mTurquoise dynamics for replicate 3. **i**, mScarlet dynamics for replicate 3. Each individual peak corresponds to a growth cycle for a given well. Early cycles are plotted in dark colors, starting in dark blue, and progress to light colors as cycle number increases, finishing in light green. Max fluorescent signal during this growth signal was taken to be representative of composition for a given fluorescent channel.

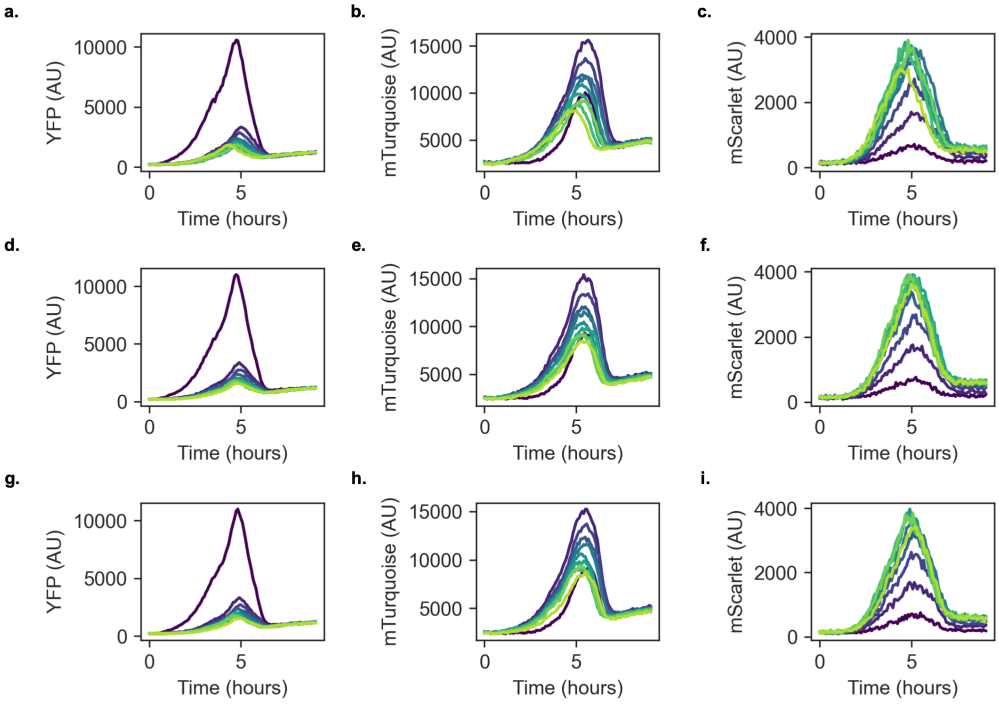

Figure S12: Raw 3-state composition control fluorescent traces for condition K. **a**, YFP dynamics for replicate 1. **b**, mTurquoise dynamics for replicate 1. **c**, mScarlet dynamics for replicate 1. **d**, YFP dynamics for replicate 2. **e**, mTurquoise dynamics for replicate 2. **f**, mScarlet dynamics for replicate 2. **g**, YFP dynamics for replicate 3. **h**, mTurquoise dynamics for replicate 3. **i**, mScarlet dynamics for replicate 3. Each individual peak corresponds to a growth cycle for a given well. Early cycles are plotted in dark colors, starting in dark blue, and progress to light colors as cycle number increases, finishing in light green. Max fluorescent signal during this growth signal was taken to be representative of composition for a given fluorescent channel.

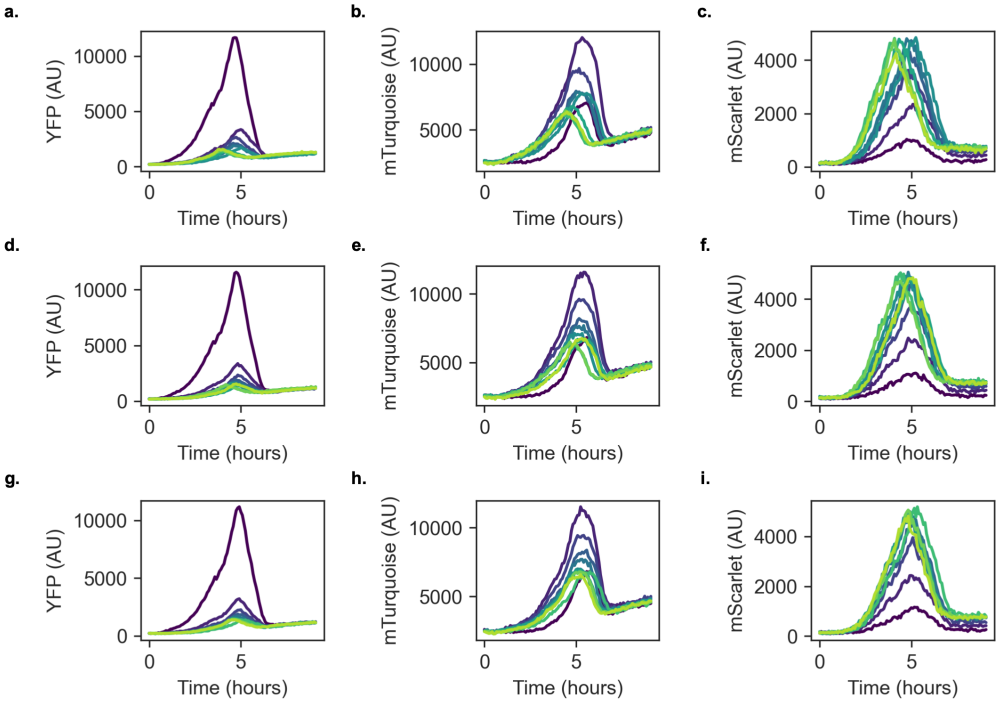

Figure S13: Raw 3-state composition control fluorescent traces for condition L. **a**, YFP dynamics for replicate 1. **b**, mTurquoise dynamics for replicate 1. **c**, mScarlet dynamics for replicate 1. **d**, YFP dynamics for replicate 2. **e**, mTurquoise dynamics for replicate 2. **f**, mScarlet dynamics for replicate 2. **g**, YFP dynamics for replicate 3. **h**, mTurquoise dynamics for replicate 3. **i**, mScarlet dynamics for replicate 3. Each individual peak corresponds to a growth cycle for a given well. Early cycles are plotted in dark colors, starting in dark blue, and progress to light colors as cycle number increases, finishing in light green. Max fluorescent signal during this growth signal was taken to be representative of composition for a given fluorescent channel.

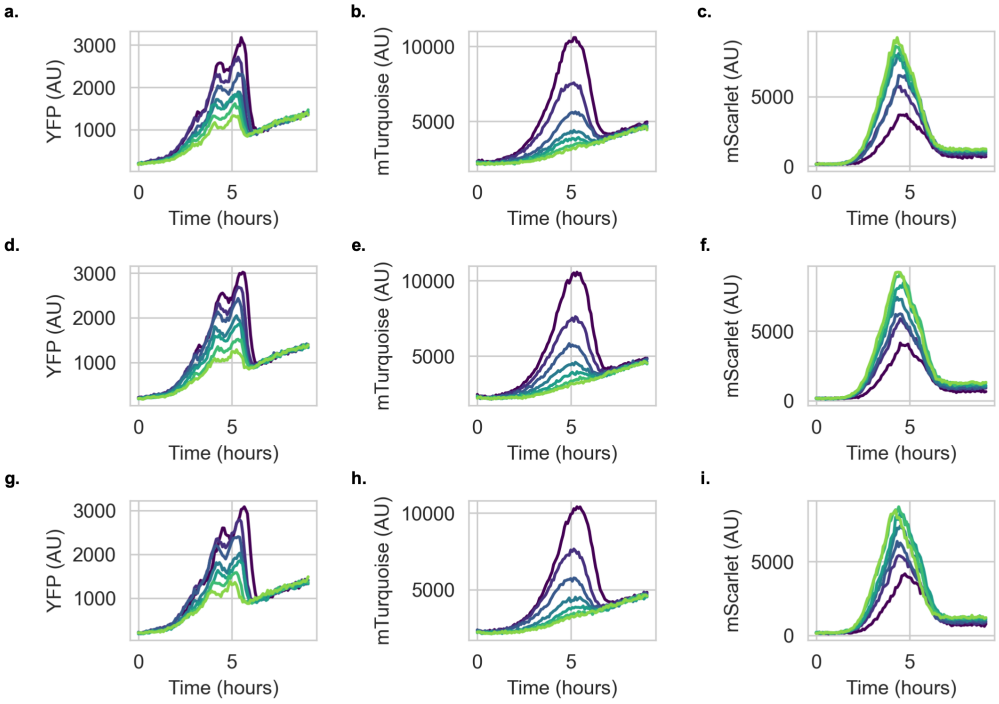

Figure S14: Raw fluorescent traces for 3-strain uncontrolled consortia. **a**, YFP dynamics for replicate 1. **b**, mTurquoise dynamics for replicate 1. **c**, mScarlet dynamics for replicate 1. **d**, YFP dynamics for replicate 2. **e**, mTurquoise dynamics for replicate 2. **f**, mScarlet dynamics for replicate 2. **g**, YFP dynamics for replicate 3. **h**, mTurquoise dynamics for replicate 3. **i**, mScarlet dynamics for replicate 3. Each individual peak corresponds to a growth cycle for a given well. Early cycles are plotted in dark colors, starting in dark blue, and progress to light colors as cycle number increases, finishing in light green. Max fluorescent signal during this growth signal was taken to be representative of composition for a given fluorescent channel.

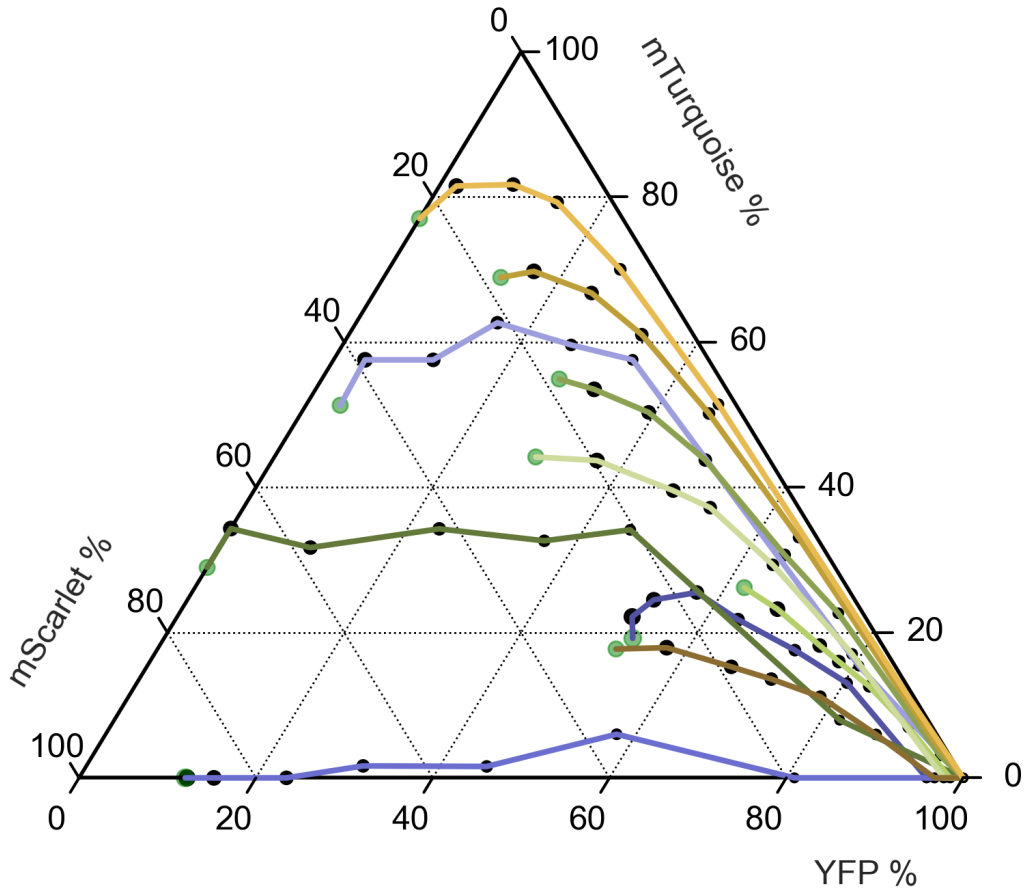

Figure S15: 3-state composition control traces. Different color traces correspond to different inducer conditions described in Table S2. Fluorescence values have been normalized to the max possible fluorescence signal for the given channel. As typical for a ternary diagram, the ratio of all three channels is used to calculate positions of individual trajectories. Each point in a given trajectory is separated by a fixed growth cycle of 12 hours.

Condition	Salicylate (μM)	IPTG (μM)	Lux (μM)	Cin (μM)
Condition A	3.75	5	0.001	0.1
Condition B	3.75	50	0.003	0.25
Condition C	4.375	25	0.001	0.1
Condition D	4.375	25	0.0025	0.7
Condition E	6.5	25	0.001	0.1
Condition F	5.5	50	0.001	0.1
Condition G	6.5	25	0.0025	1
Condition H	5.5	100	0.0025	0.25
Condition I	9.5	25	0.002	0.1
Condition J	10.5	25	0.002	0.1
Condition K (Fig 6d)	18	500	0.008	12
Condition L (Fig 6d)	18	500	0.008	4

Table S2: Conditions used for the 3-state composition control experiments. Molar concentrations of Salicylate (Bxb1), IPTG (Bxb1 RDF), Lux AHL (TP901) and Cin AHL (TP901 RDF) inducers employed for the experiments displayed in Figure 6c. The different color indexes corresponds to the different color traces in Figure S15.

Chapter 4

IMPLEMENTING FEED-FORWARD LOOPS FOR IMPROVED BIOSENSING

4.1 Introduction

Whole-cell biosensors are cells engineered to detect specific environmental or molecular signals, often producing a measurable output such as a fluorophore [1]. Biosensors are unique in that they directly measure bio-available levels of analytes, making them particularly useful in biological applications such as agriculture and human health [2]. Many biosensors have been developed and characterized in the context of this measuring function.

However, biosensors can be integrated into even more powerful configurations — they can be used to actuate a critical, analyte-relevant function. Chimeric antigen receptor (CAR) T-cells are a natural example of this "sense and actuate" configuration [3]. Specifically, T-cells detect specific antigens via engineered surface receptors (sensors) and in turn trigger a powerful cytokine response (actuation). Although a cancer therapeutic example, this general configuration could be used in many application such as soil remediation [4] and gut microbiome therapies [5], among many others.

However, the consequences of spurious biosensor activation become much more significant when tying biosensor inputs to powerful actuation responses. A critical source of spurious activation comes from activation through transient contact with the analyte [1, 2]. Ideally, these transient activation events could be filtered out through some form of simple circuit. In this chapter we will present such a topology and demonstrate how its dynamics can be modulated to fit the required filtering properties.

4.2 Background

Feed-foward loops

A feed-forward loop (FFLs) is a three node topology that is enriched in many natural transcriptional networks [6]. It consists of a transcription factor (X) regulating a second transcription factor (Y) which together regulate a gene (Z). This topology can be thought of as having a direct (X–>Z) and indirect (X–>Y–>Z) regulation arm and the nature of the regulation can be either activating or repressing [7]. FFLs are further classified based on two factors:

- Coherency: Determined by the match between the regulatory nature of the direct and indirect regulation arms. If both arms are the same, the FFL is coherent, if they differ, the FFL is incoherent
- Z Logic: Determined by how the combined inputs from X and Y influence the output of Z. Generally, we only consider two logics, OR and AND logics. In OR, the presence of X or Y is sufficient to activate expression of Z. In AND, the presence of both X and Y is necessary to activate expression of Z.

By varying both coherency and logic, a wide variety of dynamical behaviors are accessible. We focus specifically on the Coherent Type 1 FFL with AND logic (C1-FFL, Figure 4.1). In this FFL, both regulation arms activate Z (coherent) and X AND Y must be simultaneously present to activate Z (AND). This specific FFL possesses a sign sensitive ON delay (T_{on}) — Z will turn on with a certain delay upon exposure to a constant, saturating amount of a signal (S_x). This can intuitively explained by the fact that X must first accumulate and then activate Y, which then must also accumulate to activate Z. As Z requires both X AND Y present, the timescale of Z activation is set by the sequential accumulation process of the indirect arm [7, 8] (Figure 4.1).

When considering pulsing inputs, this configuration can filter transient pulses of S_x with a duration shorter than T_{on}. During these short pulse X directly activates Y but Y is unable to accumulate to the necessary level, as such only X stimulates Z which is insufficient to activate Z due to the AND regulation logic. This property is also know as persistence detection as only pulses longer than T_{on} will cause the expression of Z. Previous work mathematically demonstrated that T_{on} can be increased by reducing the affinity of Y for Z (K_{yz}) [7]. Thus, this C1-FFL with AND logic is an interesting circuit for tunable filtering transient biosensor activation events.

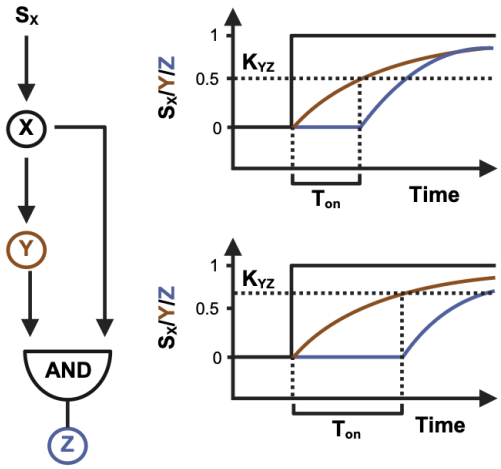

Figure 4.1: Schematic and tunable dynamics of the C1-FFL. S_x corresponds to an input signal, X and Y are transcription factors and Z is the output. Time dynamics have multiple traces corresponding to each species and are color-coded according to the schematic (S_x/X=black, Y=red, Z=blue).

Small transcription activating RNAs

Small transcription activating RNAs (STARs) are synthetic RNA molecules that function as activating transcription factors [9]. To use STARs, a target sequence forming a hairpin structure with a polyuracil tail is placed upstream of a gene, forming an intrinsic terminator (Figure 4.2). In the absence of the STAR, this target sequence forms a terminator during transcription, efficiently aborting transcription. However, when the STAR is present, it binds to this target sequence and inhibits the formation of the hairpin and thus prevents termination, allowing transcription to continue. In practical terms, STARs are the RNA versions of activating protein transcription factors.

For implementing a C1-FFL with AND logic, STARs are a particularly strong candidate. A relatively compact configuration with two transcriptional units can create a C1-FFL (Figure 4.7), whereas alternative protein transcription factor approaches, e.g. Split T7 Polymerase [10], would require more components and transcriptional units. Critically, the modular structure of STARs could provide a pathway to tunable filtering properties through progressive modulation of target affinity via progressive truncations [9]. As such, our implementation could be customized according to the associated timescales demanded by the end-user's application.

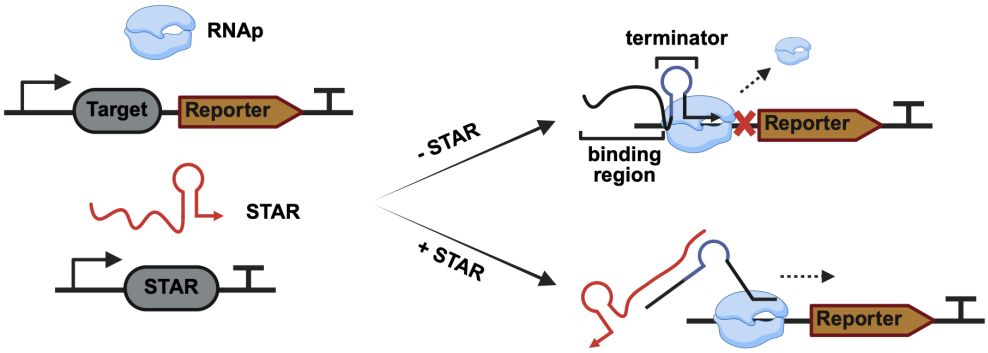

Figure 4.2: STAR mechanism schematic. Without the STAR, a terminating stem loop is formed during transcription, aborting transcription. When the STAR is present, stem loop formation is inhibited by interactions between binding regions of the STAR and target binding regions.

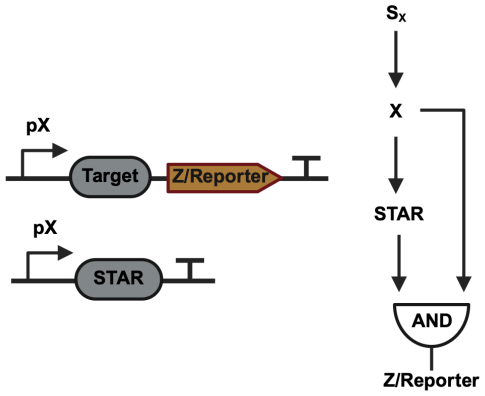

Figure 4.3: STAR C1-FFL implementation. pX correspond to a promoter responding to an arbitrary input signal S_x, and X corresponds to the transcription factor activating this promoter. The system functions as an AND gate as both STAR and X are required to activate Z/reporter expression.

4.3 Results

Testing initial STAR function

Previous work attempting to use STARs in the Murray lab had failed and after discussions with several individuals from the Lucks labs, several modifications to the primary STAR constructs were implemented. First, it was recommended to add the tobacco ringspot virus self-cleaving ribozyme (sTRSV) upstream of the STAR sequence. Chelsea Hu had previously found this to be important in preserving STAR function, possibly because it helps insulate the STAR from any interference in RNA folding originating from the upstream sequence. We further conserved several

cloning scars present in the original STAR constructs, minimizing any deviations from the original DNA context.

With these modifications, we proceeded to verify the STARs capacity to activate transcription from a constitutive promoter (J23102). We used two plasmid configurations: STAR-ColE1H (~70 copies) + target-p15a (~15 copies) and STAR-p15A + target-PSC101 (~5 copies) to investigate possible STAR-target ratio and copy number effects. We tested two STAR-target pairs, the 0/1 pair and 8/9 pair, expressing the STAR under control of a lux inducible promoter (p15a) and GFP under the control of the J23102-target promoter (PSC101).

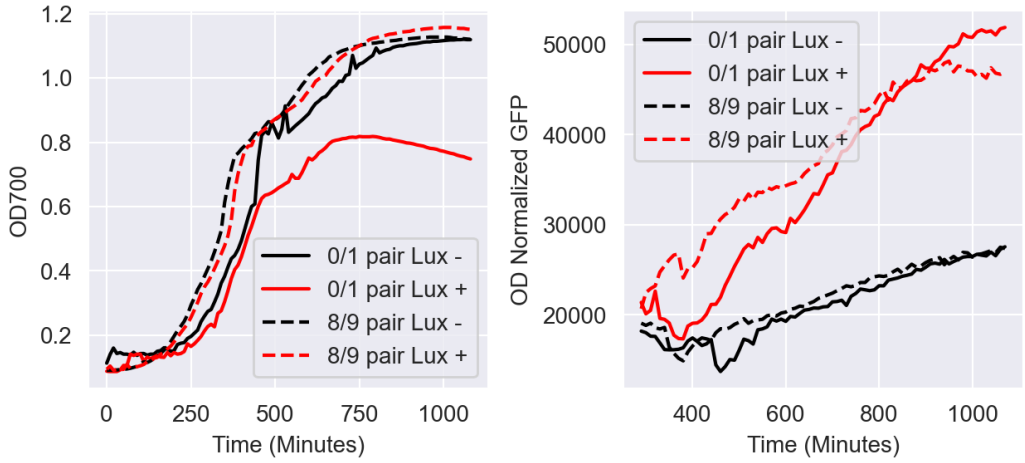

Figure 4.4: STAR plate reader dynamics in P15a (STAR) and PSC101 (Target) configuration. Traces shown are from single well trajectories.

In this p15a-PSC101 configuration, both STAR-target pairs seem to work, providing noticeable activation (Figure 4.4). It should be noted that the 0/1 pair has a noticeable growth defect when the STAR is induced. In contrast, the 8/9 pair has no discernible difference in growth dynamics when induced. Having explored the p15a-PSC101 configuration, we then implemented the same architecture but in the ColE1H-p15a configuration.

Akin to the previous configuration, both pairs seem to induce a noticeable fold-change upon induction of the STAR expression (Figure 4.5). However, both STARs cause a noticeable burden, regardless of whether the STAR has been induced or not. This is likely due to substantial leak originating from a much higher copy number.

To more closely examine the fold-change activation we decided to compare the max GFP signal normalized to OD across all samples (Figure 4.6). This would allow us

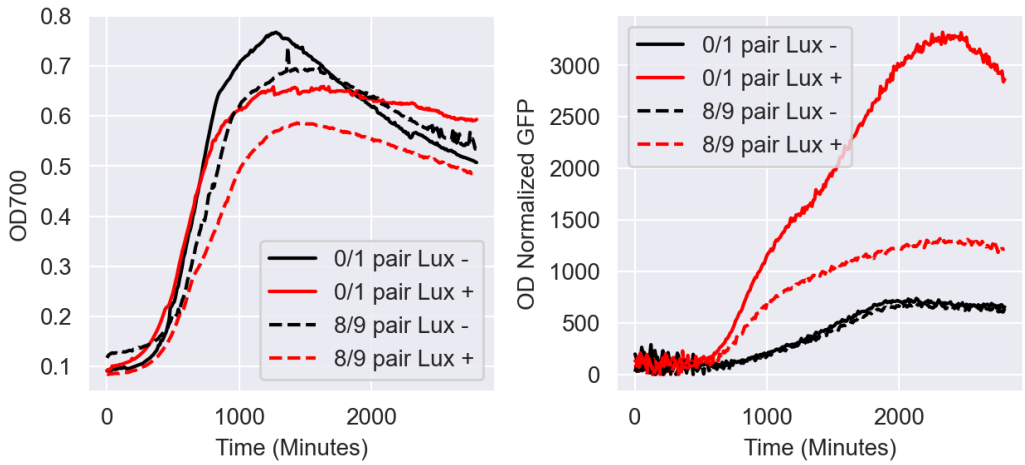

Figure 4.5: STAR plate reader dynamics in ColE1H (STAR) and p15a (Target) configuration. Traces shown are from single well trajectories. GFP signals are at much lower levels than Figure 4.4 due to being performed on a different Biotek plate reader.

to determine which plasmid configuration works best for each STAR pair.

When considering Figure 4.6a and Figure 4.6b, it would seem that moving from p15a/PSC101 to colE1H/p15a substantially improves the fold change associated with the 0/1 pair, from 2X to 5X. On the other hand, the 8/9 pair seems to have a 2X fold change under both configurations. Having demonstrated the greatest fold change with the colE1H/p15a configuration, we moved forward with using this configuration for subsequent constructs.

Implementing STAR-mediated AND gates

With the previous experiments, we demonstrated that STARs function can be replicated. It is interesting to note that our observed fold-changes are vastly inferior to the 9000X fold-change observed by Chappell et al. [9] in spite of close matching of strain and genetic context. Part of this may be ascribed to their use of flow cytometry instead of plate readers but such a large disparity is surprising. Regardless, the next goal was to compose these STAR pairs into AND gates, using Lux to express the STAR and having either Sal, IPTG, or Cin promoters bearing the target sequence (Figure 4.7).

For this set of experiments, we constructed the aforementioned AND gates and tested them in a configuration with no inputs, single inputs and both inputs. Figures 4.8-4.10 show the traces for the 0/1 AND gates, in all cases Lux was used to express

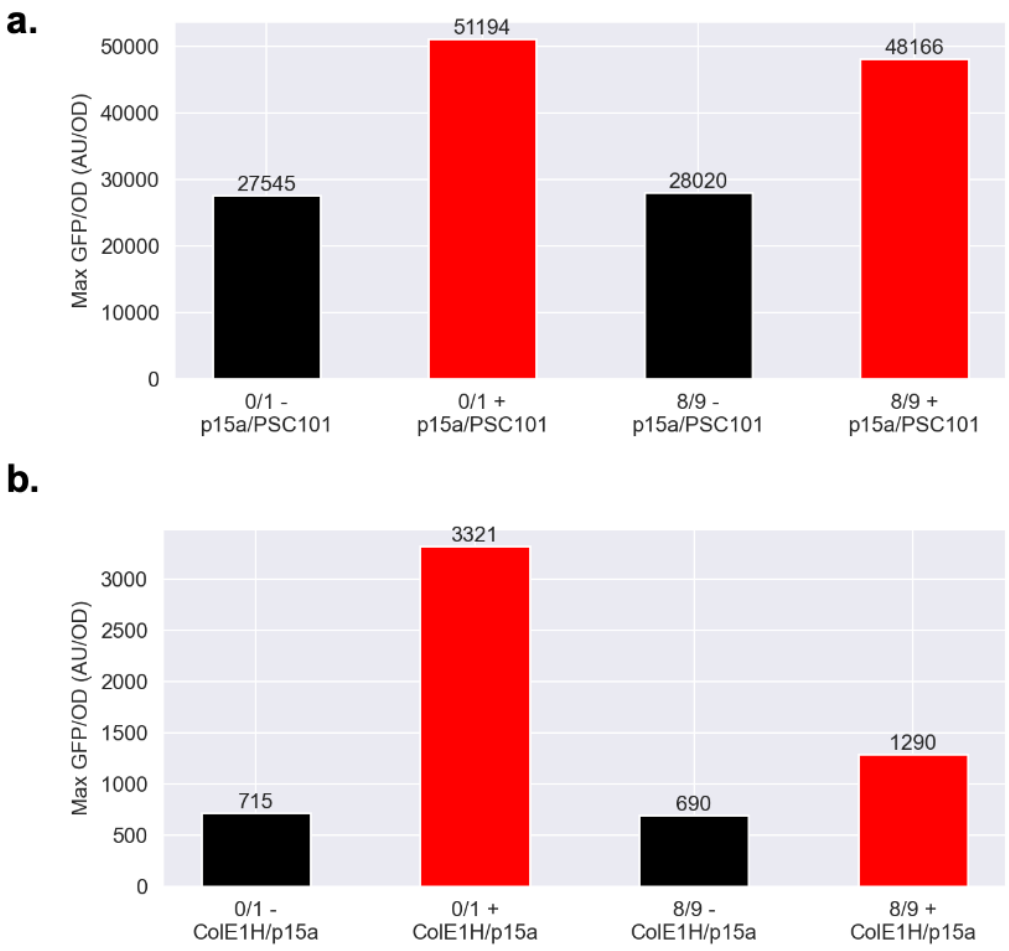

Figure 4.6: **a**. Max OD normalized GFP in P15a (STAR) and PSC101 (Target) configuration. **b**. Max OD normalized GFP in ColE1H (STAR) and p15A (Target) configuration. Values were calculated by taking max GFP signal and dividing by OD at the same time point. Calculations are based on trajectories from Figure 4.4.

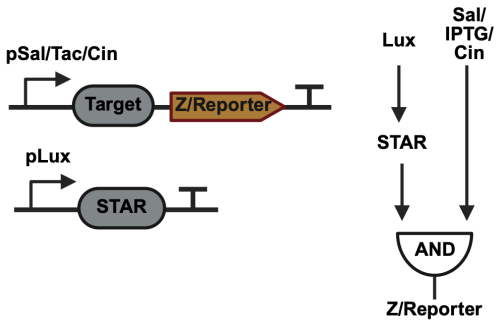

Figure 4.7: STAR AND gate implementation.

the STAR from colE1H and the target promoter on p15a was varied.

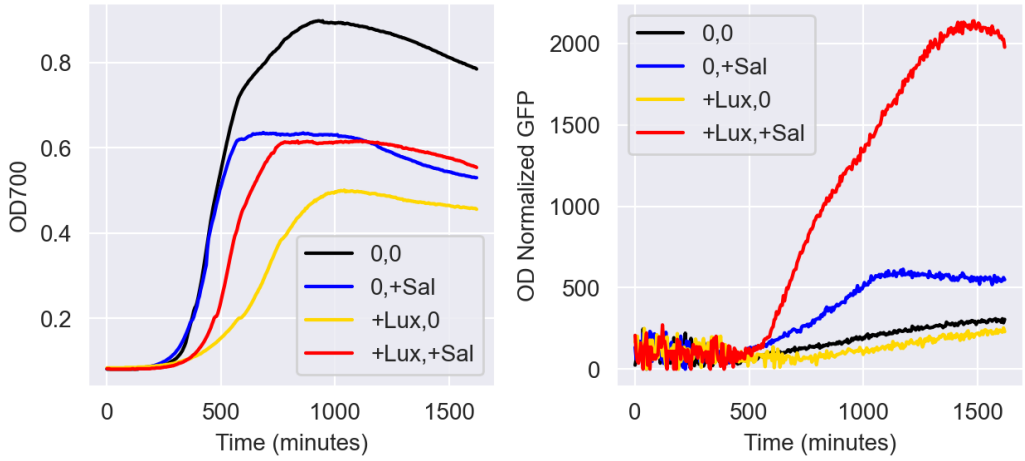

Figure 4.8: Sal AND gate plate reader dynamics. Traces shown are from single well trajectories.

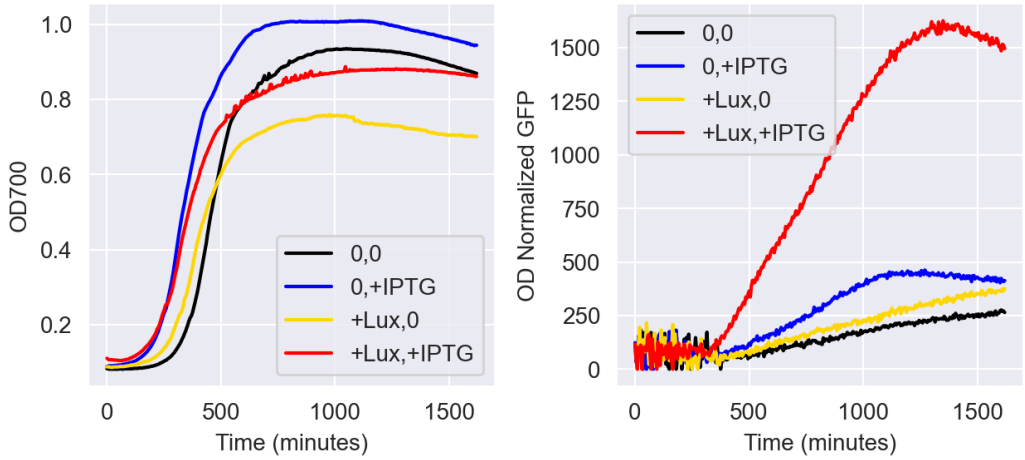

Figure 4.9: IPTG AND gate plate reader dynamics. Traces shown are from single well trajectories.

For the 0/1 pair, the Lux-Sal and Lux-IPTG AND gates worked well (Figure 4.8 and Figure 4.9), experiencing the largest degree of activation when both inducers were present. Some degree of activation that occurs exclusively through the non-lux inducer but this activity is discernible from the activation when both inducers are present. The Lux-Cin AND gate showed no noticeable activation under any combination of inducers (Figure 4.10). Not shown in this main text are any of the 8/9 AND gates — none of these worked as intended. Either one inducer was

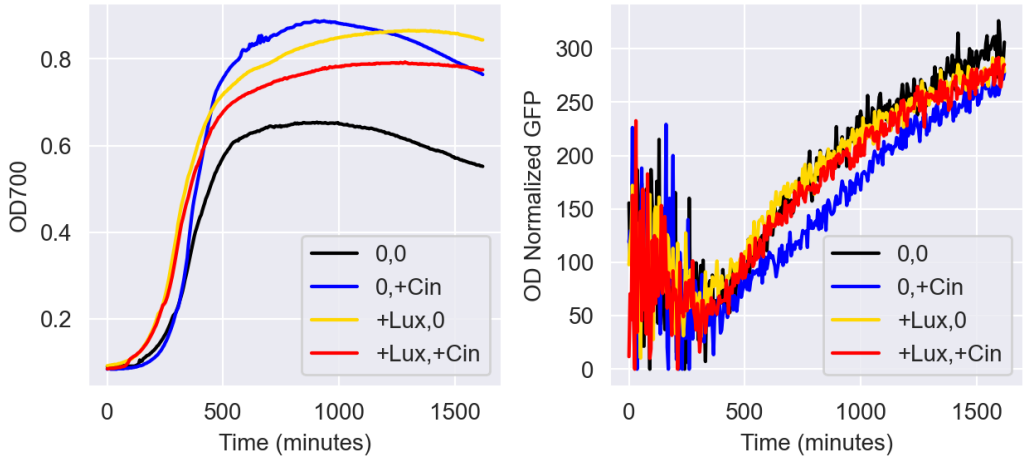

Figure 4.10: Cin AND gate plate reader dynamics. Traces shown are from single well trajectories.

sufficient to cause full activation or no activation was seen both inducers. Moving forward, we worked exclusively with the 0/1 pair.

Constructing and testing C1-FFLs (AND)

Having demonstrated that we can successfully implement AND gates taking two separate inputs, we moved on to the task of generating a C1-FFL with AND logic. The only change that had to be made with respect to our previous design is that now both inputs to the AND gate are the same, i.e. the STAR promoter and target promoter are the same (Figure 4.11).

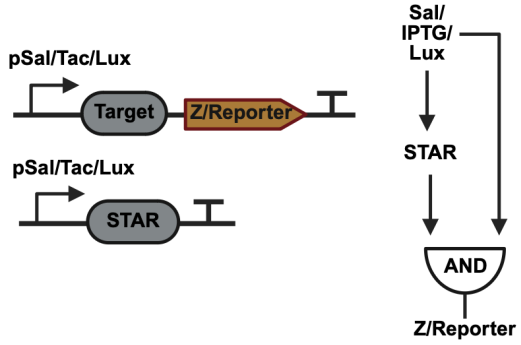

Figure 4.11: FFL AND gate implementation.

We applied this modification to the two inducible systems that had AND gate activity (IPTG and Sal) as well as the Lux inducible system. Figures 4.12-4.14 show the plate reader traces for these FFLs.

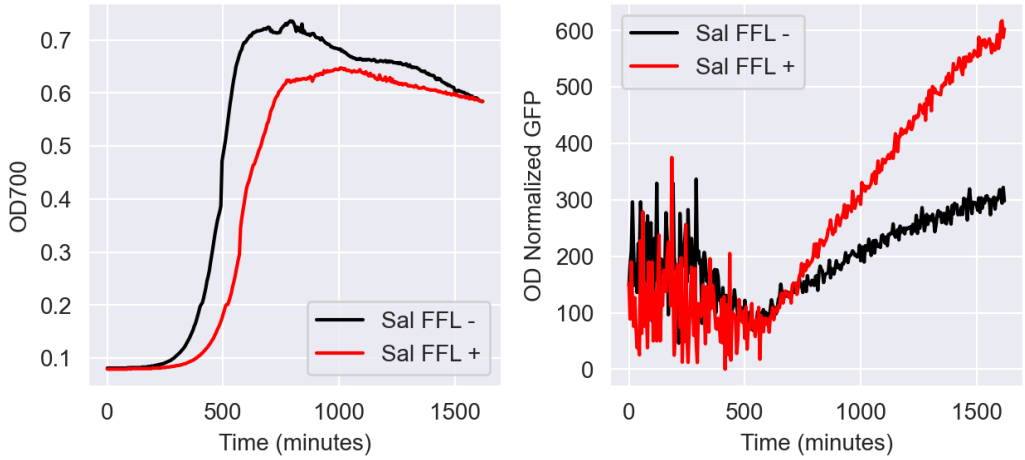

Figure 4.12: Sal C1-FFL plate reader dynamics. Traces shown are from single well trajectories.

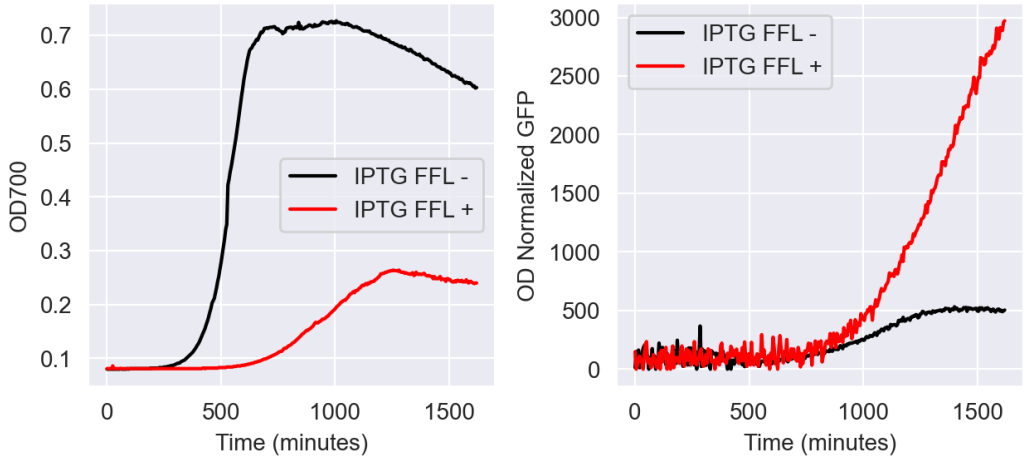

Figure 4.13: Tac C1-FFL plate reader dynamic. Traces shown are from single well trajectories.

Broadly speaking, all the FFLs show some degree of activation. The Sal FFL has by far the weakest degree of activation, even when accounting for growth differences (Figure 4.12). The IPTG FFL has a more noticeable fold-activation, but the OD curve show a distinct growth defect, likely caused by STAR expression (Figure 4.13). The Lux-FFL has a noticeable fold-activation without suffering from a severe growth defect like the IPTG-FFL (Figure 4.14).

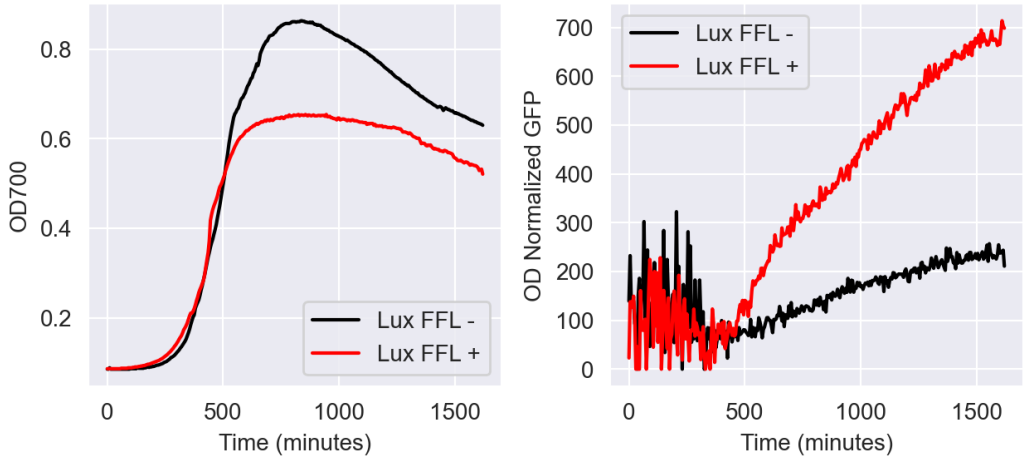

Figure 4.14: Lux C1-FFL plate reader dynamic. Traces shown are from single well trajectories.

Probing predicted C1-FFL time delay

Having demonstrated that FFLs can be composed using STARs, we proceeded to probe the inducer response dynamics of the best performing FFL (Lux). We specifically wanted to confirm the existence of the predicted time delay and we opted to initially do so using bulk plate reader measurements. Previous characterization of the natural Arabinose-cAMP C1-FFL demonstrated the existence of the time delay using a similar bulk measurement approach [8]. For this experiment, the appropriate control was necessary to confirm the existence of a time delay. This was the 'open loop' configuration, where the STAR is constitutively expressed. This configuration should only express delays arising from the direct regulation arm, unlike the FFL where the signal must propagate through both arms via Lux induction.

In our experimental setup, both strains were grown to late-exponential phase, diluted to an OD700 of 0.3, and simultaneously exposed to a lux concentration of 0.1 uM (Figure 4.15) and 1 uM (Figure 4.16).

Under both induction concentrations both the open loop and C1-FFL seem to activate at approximately the same timescale — around 75/80 min post-induction (Figure 4.15 and Figure 4.16). Surprisingly, when considering the full plate reader traces, it seems as if the C1-FFL possesses some form of response **acceleration** property, with the FFL reaching its max expression level faster than the open loop control. This is seen in the right panel of Figure 4.15 and is particularly clear in the right panel of Figure 4.16.

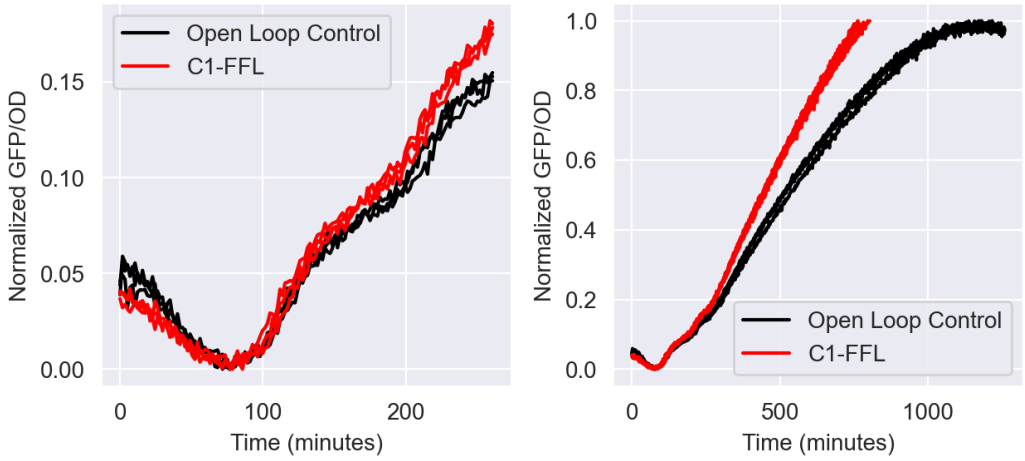

Figure 4.15: 0.1 μM lux induction pulse response traces. Both the open loop and C1-FFL were simultaneously induced 3 minutes prior to t=0 in these plots. The left panel is a zoomed-in version of the right panel. These experiments were performed with three replicates for each circuit.

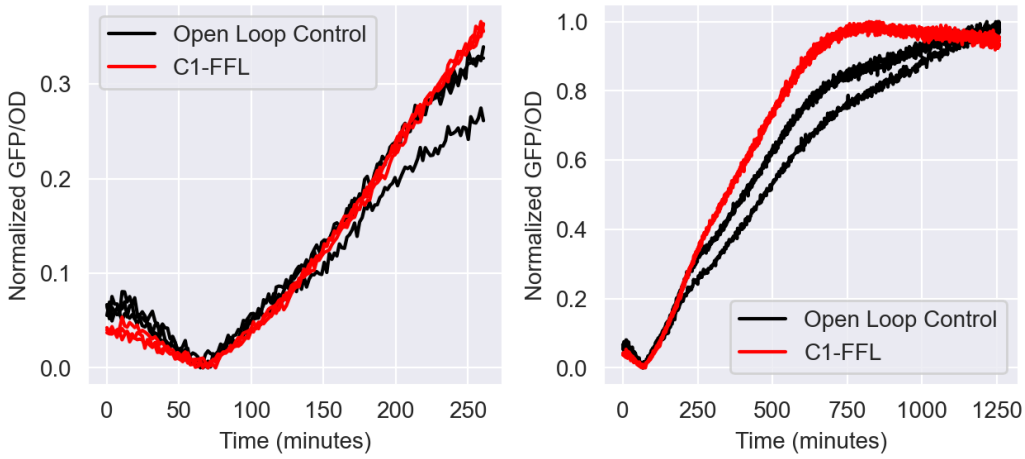

Figure 4.16: 1 μM lux induction pulse response traces. Both the open loop and C1-FFL were simultaneously induced 3 minutes prior to t=0 in these plots. The left panel is a zoomed-in version of the right panel. These experiments were performed with three replicates for each circuit.

Truncation titration

With STARs, we expected that via progressive truncation of either stem loop or binding region, we would be able to modulate affinity (and thus filtering properties) of a given STAR. To this end, we generated progressive truncation of the 4971 STAR in both regions. We titrated these variants from a pTet promoter (aTc-responsive) on a ColE1H backbone and examined their capacity to activate expression from

J23102-target promoter on a p15a backbone (Figure 4.17).

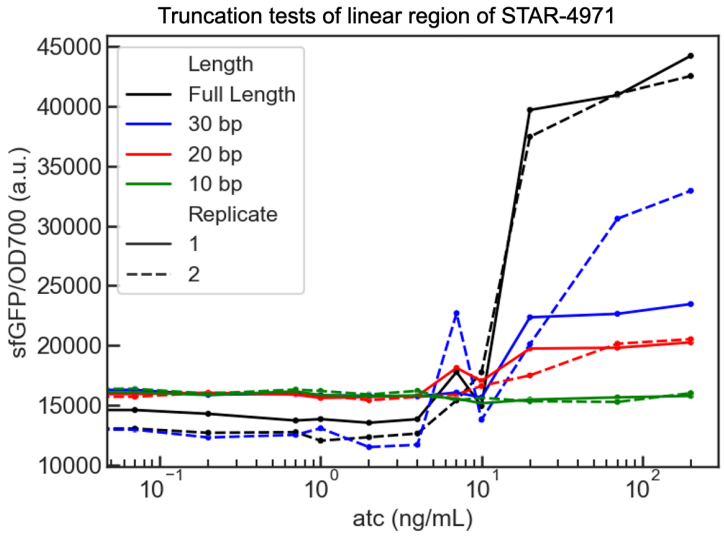

Figure 4.17: aTc dose response for stem-loop truncation. The endpoint GFP/OD is displayed. Different colors correspond to differing truncation lengths and solid and dotted lines are different replicates.

When considering the dose response curve, a progressive truncation of the stem-loop region does not produce a shift in STAR affinity (Figure 4.17). Instead, the truncation only modulates the maximal activation produced by STAR expression. It is interesting that the larger 13 bp truncation retains most of the maximal activation whereas the shorter 7 bp truncation loses a much greater extent of fold-change activation.

When considering a similar experiment looking at progressive truncation of the linear region, we see a similar effect (Figure 4.18). Specifically, progressive truncation of the linear region does not modulate STAR affinity but modulates the maximal activation. Unlike the stem-loop truncation, increasing the length of truncation leads to a progressive, linear decrease in the maximal activation. Overall, truncations of either the stem-loop or linear region do not yield the desired affinity shift.

4.4 Discussion

Summary of findings

In this chapter we attempted to implement and measure the properties of a STAR-based C1-FFL. We initially demonstrated that STAR-based activation from constitutive promoters can be replicated (albeit with lower performance) and was sensitive to copy number ratio between the STAR and the target. Subsequently, we demon-

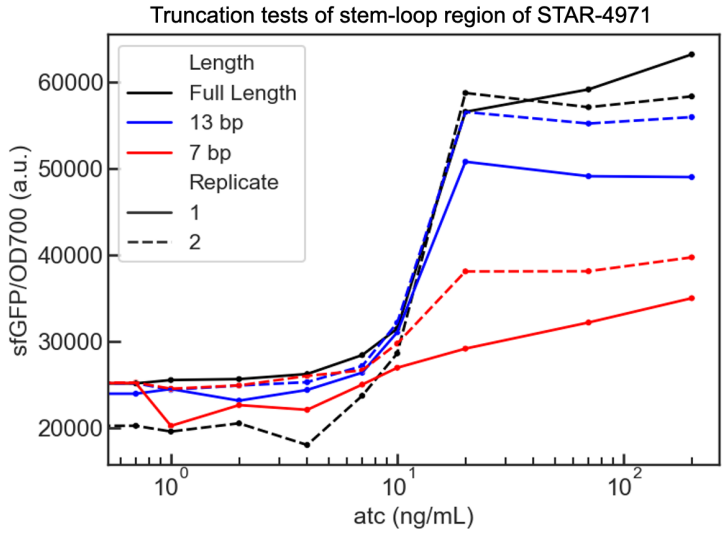

Figure 4.18: aTc dose response for linear region truncation. The endpoint GFP/OD is displayed. Different colors correspond to differing truncation lengths and solid and dotted lines are different replicates.

strated that STARs can create functional AND gates when combined with a variety of inducible promoter. However, this AND gate function is not guaranteed: one STAR pair (8/9) and inducible promoter (pCin) could not create AND gate activity.

Having demonstrated that AND gates can be constructed, we then created C1-FFLs using the functional AND gates. In all cases, the C1-FFLs activated, although certain FFLs produced either weak activation or overwhelming growth burden. Of these FFLs, we moved forward with the Lux FFL that displayed minimal growth defect and good activation upon induction. When compared to a simple induction circuit, FFLs are expected to display a delayed activation upon exposure to an inducing signal. We attempted to demonstrate this property in a bulk plate reader setting, but the experiment showed no detectable delay. Paradoxically, the Lux-FFL seemed to display a response acceleration property, a behavior consistent with an I1-FFL or some form of negative autoregulation [7]. In tandem we investigated the feasibility of tuning STAR affinity via progressive truncation of the linear and stem loop region. In both cases, progressive truncations simply modulated the fold-change activation of the STAR, with no impact on STAR affinity.

Overall, this initial exploration heavily implies that STARs are unsuitable for implementing a useful C1-FFL architecture. It possible that our implementation indeed has a delay but that it is so small that it gets lost in the context of cell and batch variability. Indeed, the delay reported by Mangan et al. [8] for the arabinose operon

FFL was only 20 minutes. It is feasible that the RNA-only layer of our FFL provides no meaningful delay when compared to a layer with both transcription and translation.

A T7 Polymerase alternative implementation

As previously stated, STARs seemed ideal to implement the C1-FFL — they enable a compact implementation and it seemed feasible to tune STAR affinity and thus filtering properties. However, this work has demonstrated some of the difficulties when using STARs, and when considering previous results from Mangan et al. [8], it seems that STARs do not provide a usable delay.

As such, it would be useful to consider other tools that could be implement the C1-FFL. Given our concern with excessively small delays arising from the RNA-only nature of STARs, alternative implementations should use components requiring full transcription and translation layers. A transcription regulator that matches this criteria is T7 polymerase, which also has the added benefit of being host orthogonal and thus feasibly portable to non-model organisms.

T7 polymerase could be used to compose AND gates via two approaches:

- Split-T7: Shis et al. [11] split T7 polymerase by nicking the sequence at amino acids 179-180, creating a N-terminal ($T7_A$) and C-terminal fragment ($T7_B$). Both fragments are separately transcribed and translated but remain inactive until they come together to form catalytically active T7 RNAp.
- Amber-T7: Anderson et al. [12] integrated two internal amber stop codons into T7 RNAp, blocking translation of T7 unless the amber suppressor tRNA, supD is expressed. When both the T7 RNAp transcript and supD are present, the T7 RNAp is successfully translated, enabling activating of any downstream T7 promoter.

These two approaches could be used to implement C1-FFLs when combined with a secondary transcription factor like T5 RNAp (Figure 4.19). Both implementations have an extra layer of regulation compared to the previous STAR design. This would result in substantially larger genetic constructs and increased delays relative to the STAR design. However, the key filtering properties of C1-FFLs should remain as this arises from having two regulation arms of differing lengths/directness to the final output (Z) [7].

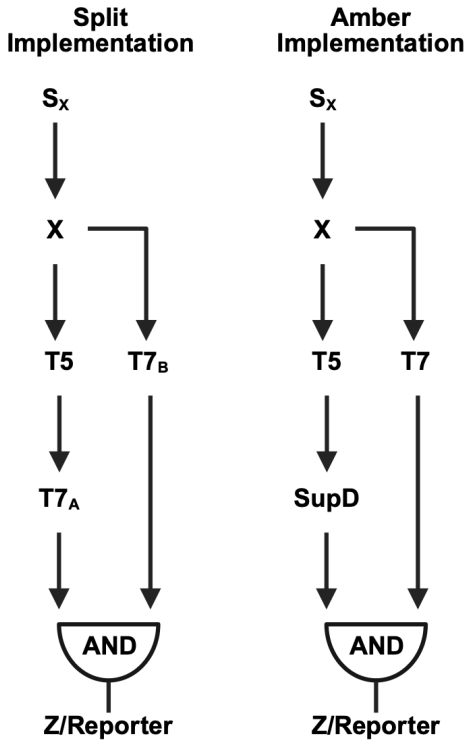

Figure 4.19: T7 polymerase C1-FFL implementations. The Split implementation uses artificially split T7 polymerase to create the AND gate logic. The Amber implementation uses amber codon mediated translation termination rescued by the SupD tRNA to create the AND gate logic.

With both approaches, it is feasible to tune the time delay and filtering properties of the circuit. For the split-T7 implementation, one may engineer split-variants with differing affinities for the assembly reaction. This could be achieved through rational engineering of hydrophobic interface residues or through more complex, computational approaches. For the Amber implementation, this tuning could be achieved through modulating the amber codon frequency in the T7 RNAp transcript. The more amber codons there are, the more SupD will be necessary to achieve successful translation of the T7 RNAp.

4.5 Materials and Methods

Cell strains and cloning

The MG1655 Marionette *E. coli* strain was used as the base strain for all strains generated in this work [13]. All new plasmids in the work were generated using 3G assembly[14], employing genetic parts from Murray Biocircuits Part Library. Several parts not found in this library were used, notably the STARs and target

sequences which were adapted from [9] and subsequently synthesized as linear fragments. Annotated nucleotide sequences can be found in the appendix section of this chapter. The exact copy numbers of plasmids vary from experiment to experiment and are detailed in the relevant sections and experimental protocols.

Cell culturing and plate reader experiments

All cultures were grown at 37 °C in M9CA 1% glucose (Teknova). Chloramphenicol (25 μg/ml) and carbenicillin (50 μg/ml chloramphenicol) antibiotics were used according to the plasmids used in each experiment. Prior to all experiments, cells were grown overnight and diluted 1:100 into 200 μl of media and grown in a 96-well plate in a Biotek H1M plate reader, with OD700 and GFP reads being performed every 5 minutes.

For experiments verifying initial STAR, AND gate and FFL function, inducer was immediately added to the relevant well. Sal, IPTG, Cin and Lux concentrations were maxed out according to the dose response data collected in the original Marionette paper. The concentrations were as follows, Sal = 100 °C , IPTG = 1000 μM, Cin = 1 μM, and Lux = 0.1 μM.

Time delay plate reader experiment

Leading up to the plate reader experiment, a similar approach described was employed. Both the open loop and FFL strains were grown for 6 hours in the plate reader. Subsequently, these cultures were diluted to and OD700 of 0.3 (200 μl media total). After dilution, 0.1 μM and 1 μM Lux was added to both sets of ODs and strains. Immediately after addition of inducer, the cultures were placed in the plate reader and grown for an additional 16 hours. During these experiments, reads were performed at the minimum possible interval (105 seconds) to maximize the possibility of detecting the expected time delay.

Truncation titration experiment

Two sets of STAR constructs were made containing three truncation variants in either the stem-loop or target region. The three variants were no truncation, 7 bp truncation and 13 bp truncation. These were only generated for the 4970/4971 STAR pair and J23102-target sequence remained unmodified from previous experiments. All these variants were placed under the control of the pTet promoter on a ColE1H backbone, with the J23102-target on a p15a backbone. Overnight cultures grown

in M9CA at 30 °C and diluted 1:100 into 200 μl cultures with atc concentration starting at 0 and then ranging from 0.7 to 200 ng/mL. The endpoint GFP over OD700 was then plotted against the relevant atc concentrations to generate a dose response curve for the 4971 STAR variants.

BIBLIOGRAPHY

1. Moraskie, M., Roshid, H., O'Connor, G., Dikici, E., Zingg, J.-M., Deo, S. & Daunert, S. Microbial Whole-Cell Biosensors: Current Applications, Challenges, and Future Perspectives. *Biosensors & bioelectronics* **191,** 113359. ISSN: 0956-5663. https://www.ncbi.nlm.nih.gov/pmc/articles/PMC8376793/ (2025) (Nov. 2021).

2. Chen, S., Chen, X., Su, H., Guo, M. & Liu, H. Advances in Synthetic-Biology-Based Whole-Cell Biosensors: Principles, Genetic Modules, and Applications in Food Safety. *International Journal of Molecular Sciences* **24,** 7989. ISSN: 1422-0067. https://www.ncbi.nlm.nih.gov/pmc/articles/PMC10178329/ (2025) (Apr. 2023).

3. Sterner, R. C. & Sterner, R. M. CAR-T cell therapy: current limitations and potential strategies. en. *Blood Cancer Journal* **11.** Publisher: Nature Publishing Group, 1–11. ISSN: 2044-5385. https://www.nature.com/articles/s41408-021-00459-7 (2025) (Apr. 2021).

4. Larsson, E. M., Murray, R. M. & Newman, D. K. Engineering the Soil Bacterium Pseudomonas synxantha 2–79 into a Ratiometric Bioreporter for Phosphorus Limitation. *ACS Synthetic Biology* **13.** Publisher: American Chemical Society, 384–393. https://doi.org/10.1021/acssynbio.3c00642 (2025) (Jan. 2024).

5. Woo, S.-G., Moon, S.-J., Kim, S. K., Kim, T. H., Lim, H. S., Yeon, G.-H., Sung, B. H., Lee, C.-H., Lee, S.-G., Hwang, J. H. & Lee, D.-H. A designed whole-cell biosensor for live diagnosis of gut inflammation through nitrate sensing. eng. *Biosensors & Bioelectronics* **168,** 112523. ISSN: 1873-4235 (Nov. 2020).

6. Mangan, S. & Alon, U. Structure and function of the feed-forward loop network motif. EN. *Proceedings of the National Academy of Sciences* **100.** Company: National Academy of Sciences Distributor: National Academy of Sciences Institution: National Academy of Sciences Label: National Academy of Sciences Publisher: Proceedings of the National Academy of Sciences, 11980–11985. https://www.pnas.org/doi/abs/10.1073/pnas.2133841100 (2025) (Oct. 2003).

7. *Bd.-Zählung der Serie aus der CIP*Alon, U. *An introduction to systems biology: design principles of biological circuits* eng. *Chapman & Hall/CRC mathematical and computational biology series* **10.** ISBN: 978-1-58488-642-6 (Chapman & Hall/CRC, Boca Raton, Fla, 2007).

8. Mangan, S., Zaslaver, A. & Alon, U. The Coherent Feedforward Loop Serves as a Sign-sensitive Delay Element in Transcription Networks. en. *Journal of*

Molecular Biology **334,** 197–204. ISSN: 00222836. https://linkinghub.elsevier.com/retrieve/pii/S0022283603012038 (2025) (Nov. 2003).

9. Chappell, J., Westbrook, A., Verosloff, M. & Lucks, J. B. Computational design of small transcription activating RNAs for versatile and dynamic gene regulation. en. *Nature Communications* **8.** Publisher: Nature Publishing Group, 1051. ISSN: 2041-1723. https://www.nature.com/articles/s41467-017-01082-6 (2025) (Oct. 2017).

10. Segall-Shapiro, T. H., Meyer, A. J., Ellington, A. D., Sontag, E. D. & Voigt, C. A. A 'resource allocator' for transcription based on a highly fragmented T7 RNA polymerase. *Molecular Systems Biology* **10.** Publisher: John Wiley & Sons, Ltd, 742. ISSN: 1744-4292. https://www.embopress.org/doi/full/10.15252/msb.20145299 (2025) (July 2014).

11. Shis, D. L. & Bennett, M. R. Library of synthetic transcriptional AND gates built with split T7 RNA polymerase mutants. *Proceedings of the National Academy of Sciences* **110.** Publisher: Proceedings of the National Academy of Sciences, 5028–5033. https://www.pnas.org/doi/10.1073/pnas.1220157110 (2025) (Mar. 2013).

12. Anderson, J. C., Voigt, C. A. & Arkin, A. P. Environmental signal integration by a modular AND gate. *Molecular Systems Biology* **3.** Publisher: John Wiley & Sons, Ltd, 133. ISSN: 1744-4292. https://www.embopress.org/doi/full/10.1038/msb4100173 (2025) (Jan. 2007).

13. Meyer, A. J., Segall-Shapiro, T. H., Glassey, E., Zhang, J. & Voigt, C. A. Escherichia coli "Marionette" strains with 12 highly optimized small-molecule sensors. en. *Nature Chemical Biology* **15.** Publisher: Nature Publishing Group, 196–204. ISSN: 1552-4469. https://www.nature.com/articles/s41589-018-0168-3 (2025) (Feb. 2019).

14. Halleran, A. D., Swaminathan, A. & Murray, R. M. Single Day Construction of Multigene Circuits with 3G Assembly. *ACS Synthetic Biology* **7.** Publisher: American Chemical Society, 1477–1480. https://doi.org/10.1021/acssynbio.8b00060 (2022) (May 2018).

Chapter 5

CONCLUDING REMARKS AND LESSONS LEARNED

Having presented these two projects, we may now examine them in the context of the introduction and themes outlined in our first chapter. With these projects, we have demonstrated that nature continues to be a source of inspiration for interesting and useful circuit behaviors and architectures. This is perhaps unsurprising — behavior that is useful for living organisms in their native environments can be useful in the context of biotechnological applications e.g. division of labor. Although we initially separated design methodologies into naturally-inspired, computationally-driven, and engineering-inspired, there is an undeniable synergy between these approaches. For instance, computational-driven approaches can help understand why specific naturally occurring architectures are prevalent. Previously cited work from Bhamidipati et al. [1] used their reinforcement learning approach to explain how the commonly-found motif of interleaved oscillatory feedback loops enables robustness to oscillator component deletions. One would expect that future approaches to circuit design will use a mix of these approaches to help build and understand circuit function and guide implementation.

Our synthetic phase variation project managed to recapitulate the intended natural behavior but the STAR project fell short. When trying to emulate natural behaviors, more often than not, our implementation will use completely different molecular machinery. This is further complicated by the plethora of synthetic biology tools that can perform a specific function e.g. repression, but differ in their exact mechanism. For instance, some tools may operate at faster timescales than others or only function in narrow parameter regimes due to the molecular details of their function. It becomes the circuit designer's job to choose the right molecular tool, balancing simplicity, flexibility and performance to achieve a given behavior.

The initial inspiration for the phase variation project came from Jin et al. [2], where stochastic switching in *B. subtilis* is generated via sigma factor competition for a limited core RNAp moiety. In theory, this implementation would scale better than our recombinase approach as each additional state requires a single, much less burdensome, sigma factor instead of a large serine recombinase. However, this system consisted of interlocking local positive and global negative feedback loops and

relied on unique and sensitive parameter symmetry. This configuration is perhaps more efficient but due to its complexity, it would have limited composition control (especially *in situ*) and it would be difficult to reproduce with current synthetic biology tools. Instead we opted to use serine recombinases to abstract this switching behavior, trading circuit scalability for implementation simplicity. In addition to improving practicality and control, the recombinase architecture has the distinct advantage of being more easily transferable to other hosts — the sigma factor implementation would certainly be species-specific. This implementation decision was critical in the successful recreation of phase variation dynamics.

However, our second project attempting to implement a C1-FFL using STARs was not successful. Our design priority was to create a system where the biosensor/promoter could be easily swapped while still retaining a small footprint with tunable affinity. STARs fit these criteria well but posed several challenges as we developed the circuit. Initially, we had great difficult simply having the STARs function—insulating ribozymes and perfect DNA context preservation from previous STAR studies was necessary and even then, performance was poor and substantial burden was observed. Critically, we failed to account for how the rapid dynamics of STAR expression (transcription only, no translation) may influence circuit dynamics. Indeed, the natural instances of C1-FFLs use protein regulators [3] and only display small delays of ~20 minutes. Although we have not confirmed this, we believe that it is likely that the C1-FFL AND topology is indeed functional but the burden and fast dynamics of its regulation compromise its ability to generate a detectable delay.

These two projects show just how carefully one must select their molecular tools. Initially, a tool may seem suitable but the fine details of its mechanism can have real and substantial impacts on circuit behaviors. These fine details are critical but often get lost when drawing circuits as simple activation and inhibition arrows. Excessive abstraction in the design process can lead us to forget the important underlying biology in these systems we are seeking to engineer.

BIBLIOGRAPHY

1. Bhamidipati, P. S. & Thomson, M. *Designing biochemical circuits with tree search* en. Pages: 2025.01.27.635147 Section: New Results. Jan. 2025. https://www.biorxiv.org/content/10.1101/2025.01.27.635147v1 (2025).

2. Park, J., Dies, M., Lin, Y., Hormoz, S., Smith-Unna, S. E., Quinodoz, S., Hernández-Jiménez, M. J., Garcia-Ojalvo, J., Locke, J. C. W. & Elowitz, M. B. Molecular Time Sharing through Dynamic Pulsing in Single Cells. eng. *Cell Systems* **6,** 216–229.e15. ISSN: 2405-4712 (Feb. 2018).

3. Mangan, S., Zaslaver, A. & Alon, U. The Coherent Feedforward Loop Serves as a Sign-sensitive Delay Element in Transcription Networks. en. *Journal of Molecular Biology* **334,** 197–204. ISSN: 00222836. https://linkinghub.elsevier.com/retrieve/pii/S0022283603012038 (2025) (Nov. 2003).